Nanoplasmonic Imaging for Real-time Protein Detection and Cell Secretion Mapping

By

Wen Yang

A dissertation submitted to the Graduate Faculty of

Auburn University

in partial fulfillment of the

requirements for the Degree of Doctor of Philosophy

Auburn, Alabama

August 2022

Keywords: LSPR, Biosensor, Cytokine, Nanoplasmonic, Single-cell imaging

Approved by

Dr. Pengyu Chen, Associate Professor of Material Engineering

Dr. Dong-Joo Kim, Professor of Material Engineering

Dr. Siyuan Dai, Assistant Professor of Material Engineering

Dr. Yi Wang, Associate Professor of Biosystems Engineering

Dr. Kyle Schulze, Assistant Professor of Mechanical Engineering

Abstract

The immune system is composed of a complex network of immune cells, proteins and, chemicals as the first line of defense to protect the human body against pathogens. Monitoring the immune status through disease progression provides extensive correlative analysis for a better understanding of the complex and highly dynamic immune system in modern patient care. Cytokines, cell-signaling proteins produced by a wide variety of immune cells, play pivotal roles in cell proliferation, differentiation, apoptosis, cytotoxicity activation, and cytokine-mediated intercellular communication. Rapid and accurate identification of cytokine-based immune fingerprints for immune monitoring provides valuable clinic information in treating infectious diseases, cancer, autoimmune diseases, etc. Various techniques have been developed for cytokine detection, such as enzyme-linked immunospot (ELASA/ELISpot), intracellular cytokine staining (ICCS), and flow cytometry. These methods provide multiparametric, static information for the traits of immune cells through either average measurement of a group of cells or repeated measurement of individual cells. However, the laborious reagent processing procedures, including multiple-step staining, washing, and blocking, greatly hinder the application of these methods to capture the subtle changes in the immune system for continuous and timely immune analysis of patients. Furthermore, direct visualization of cytokine production, diffusion, and transportation to reveal the fate of the signal mediators among immune cell populations at the single-cell level can provide mechanistic insights into intercellular communication. The aforementioned

techniques can only provide quantitative cytokine analysis, while a method for accurate quantification and mapping of the cytokine to provide spatiotemporal information of cytokine secretion in the immune network is surprisingly missing.

In this dissertation, we developed integrated optofluidic nanoplasmonic biosensing platforms for rapid, high throughput, sensitive, and multiplex cytokine detection and single-cell secretion imaging. Specifically, three projects were developed and presented as follows: 1) Label-free, ultra-sensitive, high throughput nanoplasmonic biosensor for real-time cytokine detection in amylin aggregation-induced immune responses; 2) Nanoplasmon ruler for direct visualization of single-cell cytokine secretion and cell-cell communication in CAR T-Cell cancer therapy; 3) Nanoplasmon ruler imaging for rapid SARS-CoV-2 RBD protein detection. These platforms for real-time cytokine detection and mapping show great potency in practical applications in immune monitoring, which could ultimately benefit the researchers, clinicians, and patients with better and more effective diagnosis and treatment for immune-related diseases.

Acknowledgments

I would like firstly to express my sincere gratitude to my supervisor Dr. Pengyu Chen for his continuous guidance, support, and encouragement during the past six years. without his help, this work cannot be completed. He has a strict working attitude and professional knowledges in multiple areas. I really appreciate his patience to provide all the help during my PhD career.

I would also like to thank the other members of my dissertation committee. Their insight, feedback, and advice were essential throughout my lab work and dissertation writing process.

I want to give many thanks to all the collaborators: They gave me the kindest supports and made the possibility to complete the whole projects.

I am indebted to my many of my friends and colleagues who brought me a flood of wonderful memories of the life in Auburn.

I also owe a great debt of gratitude to Dr. Guohua Chen who put me on the path to become a researcher and Dr. Shuifen Xie who showed me the wonderland of nanomaterials.

Finally, I would like to show my sincerest gratitude to my parents and sister. Their unconditional love and support give me courage and strength to overcome every difficulty. They raise me up to more than I can be.

Table of Contents

List of Figures

List of Abbreviations

AD	Alzheimer's Disease
Ag	Silver
APP	Amyloid Precursor Protein
APTES	(3-Aminopropyl)Triethoxysilane
Au	Gold
AzBTS	2,2'-Azino-Bis(3-Ethylbenzothiazoline-6-Sulfonic Acid)
Aβ	Beta Amyloid
B-ALL	B-Cell Precursor Acute Lymphocytic Leukemia
BSA	Bovine Serum Albumin
CAR	Chimeric Antigen Receptor
CE	Chemical Enhancement
CNTS	Carbon Nanotubes
CR1	Complement Receptor 1
CRS	Cytokine Release Syndrome
CSF	Cerebrospinal Fluid
CVD	Cardiovascular Disease
DMD	Discrete Molecular Dynamics
EBV	Epstein–Barr Virus
EDC	1-Ethyl-3-(3-Dimethylaminopropyl)Carbodiimide
ELISA	Enzyme-Linked Immunosorbent Assay

ELISpot	Enzyme Linked Immune Absorbent Spot
EM	Electromagnetic
FACSNP	Fe_3O_4/Au Core–Shell Nanoparticle
FBS	Fetal Bovine Serum
FRET	Fluorescence Resonance Energy Transfer
HFIP	Hexafluoro-2-Propanol
HIV	Human Immunodeficiency Virus
HSA	Human Serum Albumin
IFN-γ	Interferons-Gamma
Ig	Immunoglobulin
IL-1	Interleukin 1
IL-10	Interleukin 10
IL-2	Interleukin 2
IL-6	Interleukin 6
LED	Light-Emitting Diodes
LOD	Limited Of Detection
LPS	Lipopolysaccharide
LSPR	Localized Surface Plasmon Resonance
MCH	6-Mercapto -1-Hexanol
MES	2-(N-Morpholino) Ethanesulfonic Acid
MWs	Molecular Weights

NHS	N-Hydroxysuccinimide
NP	Nanoparticle
OD	Optical Density
OPD	O-Phenylenediamine
OTA	Ochratoxin A
PBMCs	Human Peripheral Blood Mononuclear Cells
PBS	Phosphate-Buffered Saline
PCR	Polymerase Chain Reaction
Pd	Rhodium
PDMS	Polydimethylsiloxane
PGMs	Platinum-Group Metals
PLL	Poly-L-Lysine
PMA	Phorbol 12-Myristate 13-Acetate
PNP	Plasmonic Nanoparticle
Pt	Palladium
QDs	Quantum Dots
RBD	Receptor-Binding Domain
RI	Refractive Index
RT-PCR	Reverse Transcription-Polymerase Chain Reaction
Ru	Ruthenium
SA	Streptavidin

SELEX	Systemic Evolution Of Ligands By Exponential Enrichment
SEM	Scanning Electron Microscopy
SERS	Surface Enhanced Raman Scattering
Si3N4	Silicon Nitride
SPR	Surface Plasmon Resonance Biosensor
SPRi	Surface Plasmon Resonance Imaging
SWCNTs	Single-Walled Carbon Nanotubes
SWNTs	Single-Walled Carbon Nanotubes
T2D	Type 2 Diabetes
TEM	Transmission Electron Microscopy
ThT	Thioflavin T
TiO2	Titanium Dioxide
TIRFM	Total Internal Reflection Fluorescence Microscopy
TMB	3,3',5,5'-Tetramethylbenzidine
TNF	Tumor Necrosis Factor
TPO	Thrombopoietin
VTM	Viral Transport Medium

Chapter 1

Introduction and Literature Review

1.1 Background

The rise of emerging infectious diseases as well as the increased spread of existing infections, such as human immunodeficiency virus (HIV), lyme disease, *Escherichia coli*, severe acute respiratory syndrome coronavirus (SARS-CoV), influenza, and Ebola virus[1,2], are threatening global economies and human health[3]. Since the end of 2019, COVID-19, an emerging coronavirus from SARS-CoV-2, has caused 518 million infections and 6.25 million deaths, which is a significant burden for the public health system. Before the development of the specific drugs and vaccines, early diagnosis and management usually play a crucial role in controlling the pandemic outbreak[4]. In addition to infectious diseases, some chronic diseases, such as cardiovascular disease (CVD), type 2 diabetes (T2D), and Alzheimer's disease (AD), are also the leading cause of death worldwide[5]; these diseases share risk factors linked to unhealthy modern lifestyles, like insufficient physical activity, unhealthy diets, alcoholic abuse, tobacco use, and exceptional pressure[6–8]. According to the WHO, heart disease has been the leading cause of death worldwide for the past 20 year, representing 33% of all deaths worldwide and 17.9 million people each year. Deaths from diabetes has increased by 70% since 2000 and has become the top 10 causes of death in 2020. At the same time, more than 6 million Americans aged 65 and older live with Alzheimer's disease and other forms of dementia in 2021. By 2050, that number is expected to increase

dramatically to nearly 13 million. As one of the costliest medical conditions to the society, $ 239 billion was paid by the nation for Medicare and Medicaid payment in 2021. About $1.1 trillion cost is projected in 2050. Those cost do not include the uncompensated care coming from the family members and friends of patients, which covers about 70% of the total Medicare cost for a dementia patient[9].

To mitigate the spread of disease and improve patient management, development of highly efficient, mass-produced, and highly sensitive diagnostic methods is essential[10]. Early diagnosis and daily health monitoring could also help patients with chronic diseases to properly manage or treat their illness, and to keep them from turning into full-blown disorders, thereby reducing physical harm and financial cost[11].

In addition to clinical diagnosis, cytological research, especially single-cell analysis is also important for the diseases study and drug development. Unravelling the underlying mechanism of how cells communicate upon external stimulation offers critical knowledge in a wide range of fields, such as fundamental biology, drug discovery, disease diagnosis, and cancer/stem cell research, to name a few[12–14]. Conventional cell-based assays mainly analyze the average response from a cell population and ignore the heterogeneity of individual cell[15]. It is reported that even the same cell line can differ in size, protein levels, genomes, transcriptomes, epigenomes, etc[16]. These cell-to-cell variations have great influence on the entire population function and bring biological noise in clinic therapy. However, the extremely complex intercellular communication networks in multicellular systems pose significant technical challenges to exploit the

single-cell signaling pathways. As a results, there is an emerging need for the development of novel technology that permits accurate monitoring of single-cell activities and further revels the complex cellular communication mechanisms in immune systems.

To fulfill growing demand of modern society, biosensor technologies have experienced explosive development. By combining interdisciplinary approaches, a variety of rapid, reliable, accurate, and cost-efficient diagnostics and analysis system have been developed.

1.2 Optical biosensors

Since their first application in the early 1950's, biosensors have been rapidly developed and widely used in the field of clinical diagnosis, drug discovery, biomedicine, food safety, agriculture, environment monitoring, and pollution control[17]. As disease is the leading factor that threaten human health and lives, biomedical diagnoses and biosensors have played important roles in our daily life and have a profound effect on our healthcare system.

A biosensor is an integrated analytical device that usually integrates analyte samples, recognition molecules (i.e., antibodies, enzymes, nucleic acid, aptamer) which allow the sensitive and selective detection, a transducer that can convert the biorecognition event into a measurable signal, and a display system[18]. The detection process can be roughly divided into two modes: label-based and label-free detection. Briefly, label-based mode relies on a signal probe (i.e., enzymes, radionuclides, nanoparticles, and

fluorescent or electrochemiluminescent probes) to generate the final detection signal[19,20]. Enzyme linked immunosorbent assay (ELISA) is a typical label-based method for protein detection and quantification. In this method, the target molecule was immobilized on a microplate surface and binds to specific antibody which was linked to the reporter enzyme ((i.e., horseradish peroxidase (HRP) and alkaline phosphatase (AP)). The incubation of reporter enzyme with appropriate substrate can generate a measurable signal to help quantify the amount of the target molecule. There are several formats for ELISAs including direct, indirect, sandwich, and competitive methods (**Figure 1.1**). The high-affinity antibodies pairs make ELISA a powerful tool for analyte detection with great sensitivity and selectivity. However, stepwise staining, washing, and manipulation before analysis lead to higher operational costs and longer assay times. The target biomarkers can only be measured under "static" state. In contrast, label-free test mode is performed without any signal probe. All the detection signals are generated directly by the interaction between the target biomarkers and transducer surface. The molecular presence can be real-time monitored via some biophysical properties such as molecular weight, refractive index, and molecular charge[20]. Label-free biosensing assays have made great improvement during the past few decades due to their ability for rapid and real-time detection[21,22].

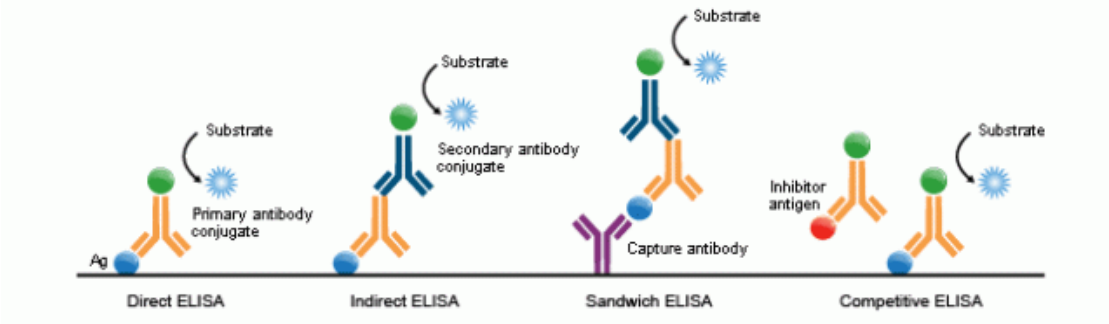

Figure 1.1 Different types of ELISA.

According to different types of transducers, biosensors can be classified into several categories, such as electrochemical biosensors, optical biosensors, electronic biosensors, thermal biosensors, gravimetric biosensors. acoustic biosensors, etc. Among them, optical biosensors have attracted plenty of attention due to the great potentials for direct, highly sensitive, real-time, and label-free detection of many biological and chemical substances[21–30]. Optical biosensors detect the biological interaction between a biorecognition element and a target molecule by measuring changes of the optical properties of the propagated light (i.e., refractive index, absorption, intensity, or wavelength). The commonly used optical biosensor usually involve fluorescence, plasmonic, Raman scattering, and optical fiber-based detection.

1.2.1 Biorecognition elements

Biorecognition element is used to capture or bind the target analyte in a biosensor device. A good biosensor requires a strong binding affinity and selectivity between the biorecognition element and analyte of interest. The most used biorecognition elements include antibody, enzymes, nucleic acid, and aptamer.

Antibody

Antibody is a large (~150 kDa) protein produced by the immune system and circulate in the blood to recognize and neutralize a specific foreign substance, called an antigen. Antibody has a Y-shaped structure containing two identical heavy chains and two identical light chains[31]. Human antibodies can be classified into five isotypes (immunoglobulin (Ig) A, IgD, IgE, IgG and IgM) based on their heavy chain constant regions, in which IgG is the most abundant antibody in the blood and serves as the main antibody in the biosensing platforms[18]. While various antigen-binding regions at both tips of the antibodies enable antibodies to recognize millions of different antigens. Due to its high affinity to the target molecule, antibodies have been widely used in different types of biosensors. However, Antibody production usually involves animals or cell cultures, leading to a costly and laborious process.

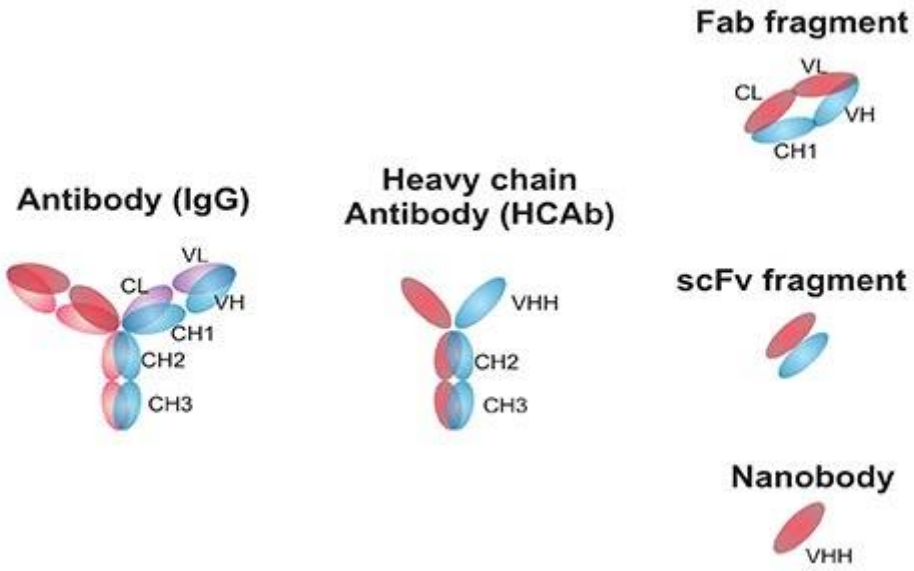

Figure 1.2 Schematics of antibody and nanobody. (https://www.cusabio.com/c-20987.html)

Recently, research on nanobody has gained a great deal of attention. Nanobody is a single domain antibody which deletes the light chain and only contains one variable domain located on a heavy chain[32](**Figure 1.2**). Compared to traditional antibodies, these much smaller (12-15kDa) antibodies have improved the stability while maintaining the original degree of recognition[33]. Besides, nanobodies are easier to produce in a large scale and their monomeric structures can be genetic encoded[34], making them good candidates in advanced therapeutics and biosensing filed[35,36].

Enzymes

Enzymes usually bind target analytes though non-covalent interactions (i.e., hydrogen-bonding, electrostatics). The binding signals are produced in biocatalytic process. Enzymes capture and catalyze target analytes, covering binding events into measurable signals (electrical, optical, or thermal signals). The signal can be further amplified for improved sensitivity[32,37].

Nucleic Acid

Nucleic acid probes may be either DNA or RNA molecules with different of lengths (100-10000 bases), ranging from short oligonucleotides to multigenic chromosomal segments. They are used to detect the presence of unique nucleotide substances within microorganisms. The binding specificity is provided from complementary binding motifs of DNA or RNA[18,32].

Aptamer

Aptamers are small single strands of DNA or RNA molecules which selectively bind to target analytes including proteins, peptides, carbohydrates, or live cells. The unique three-dimensional (3D) folded structures formed after binding usually determines the specificity and binding capabilities of aptamers[38]. Aptamers are synthesized through an in vitro selection process called Systemic Evolution of Ligands by Exponential Enrichment (SELEX) (**Figure 1.3**). SELEX is a combinatorial chemistry technique to isolate single-stranded oligonucleotides with high binding affinity to target analytes. It starts with incubation of the target analyte in a pool of random oligonucleotide sequences. After repeated rounds of purification and amplification, only high-affinity aptamer will be left and mass synthesized[39]. Since its discovery, Aptamers have received intense attention and interest in diagnostic and therapeutic fields due to their great advantages in high stability, low immunogenicity, easy for chemical modifications and mass production[40–48].

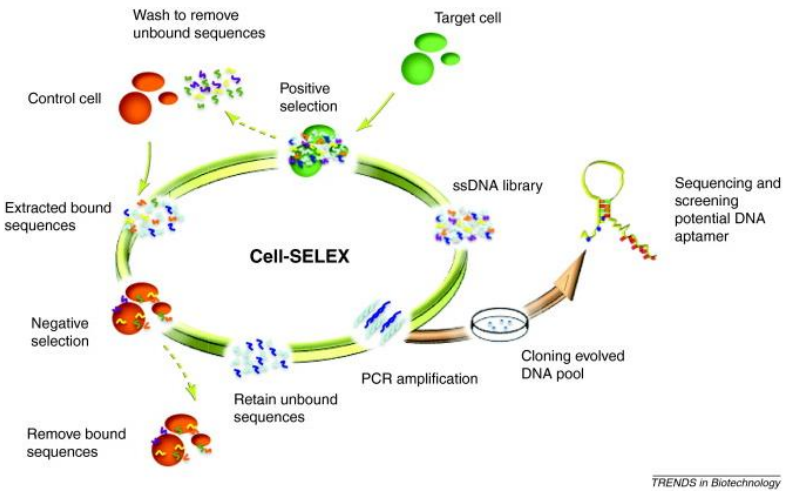

Figure 1.3 Schematic of DNA aptamer selection using cell-SELEX.

1.2.2 Nanomaterials and nanostructures in optical biosensors

The rise and maturation of nanotechnology have given us a better understanding of nanomaterials. Compared to bulk materials, nanomaterials usually show unique optical, magnetic, and electronic properties when the size of at least one dimension is less than 100 nm. Positive progress has been made in the application of nanomaterials in a wide range of filed, such as photothermal therapy, bioimaging, catalysis, spectral enhancement, and sensing, etc[49–53]. Among them, nanomaterial-based biosensors have attracted tremendous attentions due to the urgent need in the development of the personalized health care diagnostics and advanced therapeutics. The unique properties of nanoparticles such as large surface areas, biocompatibility, and catalytic activity have been discovered and exploited in different types of biosensors to improve the detection and analytical performance[54].

The physical and chemical properties of nanomaterials largely depend on their size, morphology, composition, and surface structure, etc. People can control these factors through the controlled synthesis of nanomaterials to optimize their properties, and then meet the needs of various applications.

Typical nanomaterials in biosensors

Noble metallic nanomaterials. Noble metals are metallic elements including ruthenium (Ru), rhodium (Rh), palladium (Pd), platinum (Pt), gold (Au), and silver (Ag). Nobel metal nanomaterials have been widely used in the field of biosensor due to their excellent optical and catalytical properties.

The optical properties of noble metal nanomaterials are mainly due to their local surface plasmon resonance (LSPR) effect. LSPR is a physical optical phenomenon caused by the interaction between incident light (electromagnetic field) and free electrons on the surface of metal nanoparticles. When the incident light acts on the interface between metal and medium, the free electrons on the surface of metallic nanoparticle are excited and collectively oscillate around the nanoparticle. If the oscillation frequency of such electrons is the same as that of the incident light, the resonance will occur, leading to a strong absorbance at a specific wavelength. This optical phenomenon is called LSPR[55,56]. In a typical LSPR biosensor, antibodies are functioned on the surface of gold nanostructures. Targeting antigens binding on the nanostructured surface change the refractive index of microenvironment, leading to a redshift and scattering intensity change of LSPR spectrum. Then, the presence and concentration of the analyte can be determined by monitoring the LSPR peak shift and intensity (**Figure 1.4**).

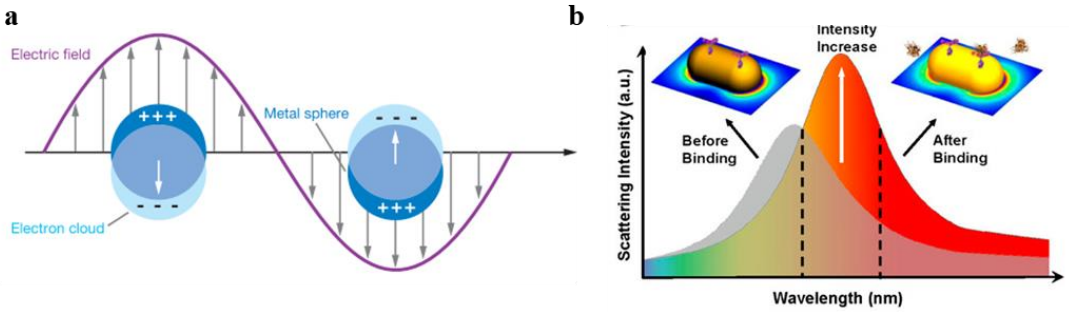

Figure 1.4 (a) Schematic diagram of LSPR. (b) A typical Au nanoparticle LSPR biosensor.[55,57]

The LSPR sensing works based on the resonance spectrum change induced by the refractive index of the surrounding medium. To improve the detection sensitivity of

LSPR biosensor, the noble metal nanoparticles that exhibit high refractive index sensitivity are highly required[58,59]. The refractive index sensitivity is defined by the ratio of the resonance wavelength shift to the change of refractive index of surrounding medium. Among all metallic nanoparticles (NPs), AuNPs have attracted enormous interest in nanoplasmonic-based biosensor owing to their excellent chemically stability, biocompatibility, and high refractive index (RI) sensitivity[60,61]. Biorecognition elements such as antibody and aptamer can be easily functioned on the gold surface through a covalent Au-S bond with a thiol group[62]. AuNPs of different shapes and sizes, such as nanospheres, nanocubes, nanobranches, nanorodes, and nanobipyramids, have been widely used in LSPR biosensor platforms. It is reported that the index sensitivities of Au nanospheres (e.g., sensitivity= 44 nm/RIU) and nanocubes are much smaller than those of nanorods, nanobipyramids, and nanobranches (e.g., sensitivity= 703 nm/RIU). In addition, for elongated nanoparticles such as Au nanorods and nanobipyramids, the index sensitivities increase with increasing aspect ratio. For example, the index sensitivity nanorods with aspect ratio of 2.4 (sensitivity=195 nm/RIU) is smaller than that of nanorods with 4.6 aspect ratio (sensitivity=288 nm/RIU)[58]. Overall, the refractive index sensitivities of AuNPs increase as the apexes of AuNPs get sharper, providing a general idea for material selection and design in nanoplasmonic sensing(**Figure 1.5**). AuNPs also exhibit strong and tunable plasmon absorption in the visible (VIS ≈ 400–750 nm) and near-infrared (NIR ≈750-2500 nm) ranges, allowing for colorimetric detection of target analytes[63,64]. Although Ag nanoparticles are less

stable than AuNPs, they offer a better sensitivity due to the higher molar extinction coefficient[65].

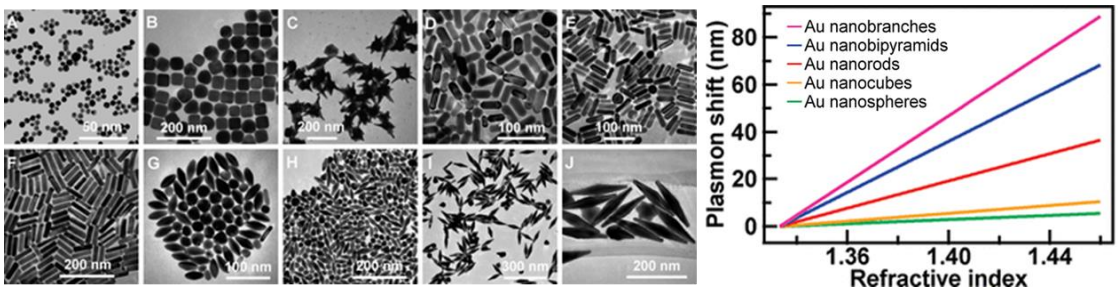

Figure 1.5 The refractive index sensitivities of Au nanoparticles with different shapes and sizes.[58]

Compared to Au and Ag NPs, Pd and Pt NPs have been seldom explored in nanoplasmonic biosensor due to their low scattering efficiency in the visible-NIR region[61,66]. However, platinum-group metals (PGMs) (Pt, Pd, Ru, Rh, and Ir) nanomaterials, are known for their excellent catalytic activity. Noble metal nanomaterials have the advantage of large specific surface area. The highly coordination unsaturated atoms on the surface can easily participate in some chemical reactions[67]. Furthermore, the d electron orbitals of the surface atoms of noble metal nanomaterials are not filled, which leads to the easy adsorption of reactants on surface. The adsorption strength is moderate, thus facilitating the formation of intermediate active compounds and promoting the catalytic reaction. Noble metal nanomaterials have been reported to catalyze the oxidation of some colorless organic chromogenic agents such as 3,3',5,5'-tetramethylbenzidine (TMB)[68,69], o-phenylenediamine (OPD)[70,71], and 2,2'-azino-bis(3-ethylbenzothiazoline-6-sulfonic acid) (AzBTS)[72] in

the presence of H_2O_2 to produce colored products, showing promising application prospects in colorimetric analysis as a peroxidase-like nanozyme[73,74].

Carbon nanotubes. Carbon nanotubes (CNTS) are hollow cylindrical tubule structures consisting of single-layer rolled-up graphene sheet. Common structures of CNTS include single-walled carbon nanotubes (SWCNTs) with a diameter of less than 1 nanometer (nm) and multi-walled carbon nanotubes (MWCNTs) consisting of several concentrically interlinked nanotubes with diameters ranging from several nanometers to hundreds of nanometers[75,76]. CNTs, especially SWCNTs, have attracted significant interest in biosensor research due to their unique physical, chemical, and optoelectronic properties for the transduction of signals associated with analyte recognitions. .

In recent year, SWCNTs have been widely used in the field of bioimaging[77,78]. Wavelengths used for excitation and emission in traditional fluorescence imaging are mainly in the visible light range (400-650nm). In this range, significant absorption and scattering induced by biological tissues and spontaneous fluorescence interference results in extremely low tissue penetration and large background noise, leading to loss of physiological and pathological information. Compared to organic molecules, SWNTs have a broad absorption spectrum and bright fluorescence emission in the near-infrared (NIR) range (900-1600nm)[79], offering an ultralow background and high penetration depth to biological tissues[80]. In addition, the absorption spectra of typical single-walled carbon nanotubes can overlap with the photoluminescence spectra of various fluorophore groups, which allows the resonance energy transfer to occur[77,81].

SWCNTs also have excellent photostability without photobleaching or blink as quantum dots are, enabling the long-term optical monitoring of biomolecules[82]. Besides, CNTs have large Raman scattering cross-sections and resonance enhancement at NIR region, making them excellent labels for Raman spectroscopy and surface enhanced Raman spectroscopy (SERS)[75,83,84]. One the other side, CNTs are high-aspect-ratio materials with extremely high surface areas which can be functionalized with biomolecules or other functional groups[85].

Quantum dots. Quantum dots (QDs) are known as zero-dimensional luminescent semiconducting nanomaterials with a few nanometers in size (2-10 nm). These materials consisting of elements from periodic groups of II–VI, III–V, or IV–VI and can emit fluorescence light which is tunable from the ultraviolet to the visible and NIR wavelengths[86,87]. Unique quantum confinement effect caused by the small size leads to an increased band-gap energy and further increases the excitation energy[88]. Compared to the traditional fluorescence dyes, QDs have higher photostability with extended fluorescence lifetime, superior signal brightness, larger Stokes shifts (difference between excitation and emission wavelength), and capability for multi-color emission, attracting tremendous attention in bioimaging and biosensor[89]. However, they also suffer from some disadvantages such as blinking, nanocolloid behavior, and biotoxicity.

Magnetic nanoparticle. Nanosized magnetic nanoparticles have superparamagnetic behaviors as the number of magnetic domains reduces. That means the magnetization only happens in the presence of external magnetic field and demagnetization will occur

immediately when external magnetic field was removed[90]. The unique magnetic properties enable magnetic nanoparticles to help to concentrate the analyte in a detection event[91]. Cai et.al exploited the unique superparamagnetic and plasmonic properties of the core–shell nanomaterials and developed a magnet patterned Fe_3O_4/Au core–shell nanoparticle (FACSNP) sensing array to achieve a label-free, high throughput cytokine detection (**Figure 1.6**). The sensor pattern quality of sensor array on the glass substrate was greatly improved with the assistance of the external magnetic field which significantly concentrated the local concentration of Fe_3O_4 nanocore[92].

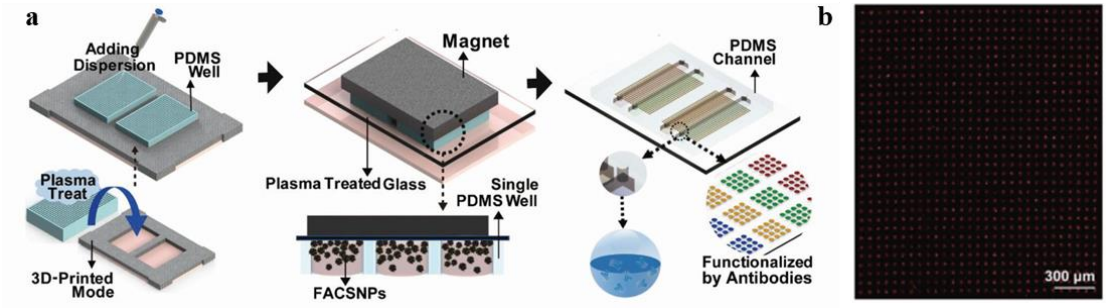

Figure 1.6 Schematics of the FACSNP microarray fabrication and dark-field microscopy images of the FACSNP microarray.[92].

Synthesis of nanomaterials

In the past few decades, the controlled synthesis of nanostructured materials has made great progress. A variety of physical and chemical methods have been developed for the synthesis of nanomaterials[93–95]. Physical synthesis methods include mechanical comminution, ultrasonic comminution, molecular beam epitaxy and evaporative condensation. Chemical synthesis methods include one pot direct synthesis, electrochemical synthesis, seed growth method and template method. Through these

synthesis methods, various nanomaterials with single morphology, uniform size and well-defined composition have been successfully synthesized, providing a strong foundation for the application in biosensors.

Biofunctionalization of nanomaterials

Efficient biofunctionalization of nanomaterials can endow them with better biocompatibility and improve the signal amplification. The functionalization can be performed in a direct or indirect way. In a direct functionalization process, interactions[91,96] between the nanomaterials and biomolecules can be achieved either through a non-covalent approach (e.g., electrostatic interaction, π–π stacking, or van der Waals forces) or a covalent approach through classic amide coupling reactions, cross-linking, amidation, or thiolation etc. Compared to non-covalent bonds, covalent bonds provide more stability and low unspecific binding. However, uncontrolled anchoring may change the surface properties and influence the analyte binding. In indirection approaches, a biomolecule can be immobilized on the nanomaterial via coordinative interactions. For example, biotinylated biomolecules can be linked to a streptavidin/avidin functioned nanoparticle[97,98].

1.2.3 Classification of optical biosensors

Fluorescence-based biosensors

Fluorescence is a phenomenon in which a molecule is excited by ultraviolet or visible light photons and emits the light with a longer wavelength. A fluorescence biosensor

usually includes an excitation light source (light-emitting diodes (LED)s or lasers), fluorophores that are used to label the target analyte, wavelength filters to isolate excitation and emission light with specific wavelength range, and a detector to record the fluorescence signals[24]. Numerous parameters have been explored in fluorescence biosensor such as fluorescence wavelength, fluorescence intensity, quenching efficiency, fluorescence anisotropy, and Förster or fluorescence resonance energy transfer (FRET). FRET is a nonradiative energy transfer form one donor fluorophore to an acceptor fluorophore involving in a dipole-dipole coupling process between two fluorophores in closer proximity (~1-10nm)[26,99]. The coupling results in a different fluorescence wavelength and intensity. The effect provides an effective way to investigate the protein-protein interaction. Recent development of FRET research and improvement of biosensor device has established many effective methods for biological imaging and single-molecule detection.

Surface plasmon resonance (SPR)-based biosensors

The surface plasmon resonance biosensor is a well-developed powerful optical detection technique for label-free biomolecular detection in real-time. SPR biosensor usually uses an Au nanolayer as a transducer[100]. SPR occurs when the electrons at the metal surface are excited by an incident light with a certain incident angle, resulting in resonant oscillations propagating along the metal-dielectric interface within the 100-300nm of the field. The resonating electrons are also known as surface plasmons which are highly sensitive to the refractive index (RI) of surrounding medium. Binding of the

target on to the transducer surface will induce changes of light properties (RI, intensity, incident angle) which are proportional to the concentration of analyte. SPR biosensors can help to investigate the time-dependent interaction process between analytes and bioreceptors through real-time monitoring of the SPR response, which enables the analysis of the binding kinetics of analyte molecules (association constant Ka, dissociation constant Kd, and equilibrium constant KD)[101].

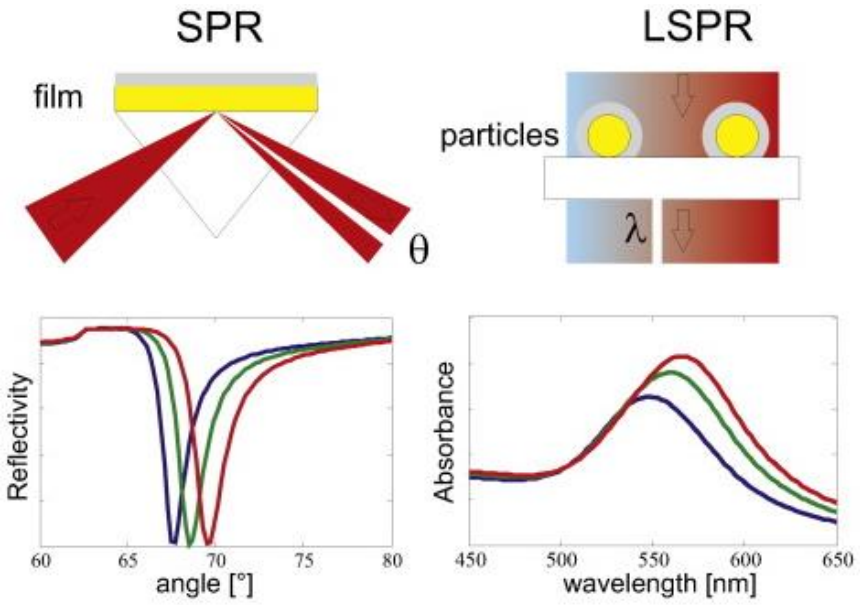

Figure 1.7 Compare the sensing principle of SPR (left) and LSPR (right). [102]

Localized surface plasmon resonance (LSPR)-based biosensorsLSPR biosensor has been regarded as a new generation of label-free detection method. It generally employs metallic nanostructures, such as nanospheres, nanorods, nanoshells, nanowires, and nanoprisms, as transducers. Instead of propagating on the large interface, the evanescent field of LSPR is confined around the plasmonic nanostructures with penetration depths around 10-30 nm[103]. Since electric fields are only enhanced near a small range of particle surface, the bulk effect and false positive

signal are greatly reduced. Binding of the analytes to the surface of plasmonic nanostructures results in the local RI change, which can be sensitively monitored by the detector[55]. The development of nano-photolithography techniques has enabled the fabrication of highly controlled nanostructures on the sensor substrate. The use of LSPR has several attractive unique optical properties. First, the scattering from a plasmonic NP is bright enough that single NPs can be identified using optical microscopes and dark-field illumination[104]. Coupled with high refractive index sensitivity, the sensor sensitivity can be greatly enhanced[105]. Another advantage of NP is that their optical properties are stable over time even with prolonged excitation, unlike fluorophores that are susceptible to photobleaching. Thus, long-time monitoring is available[61]. Also, scattering from NPs can be seen by the naked eye, promoting their use in colorimetric biosensing (such as pregnancy test). In addition, LSPR signals are completely tunable by adjust the size, shape, and composition of the NPs[1]. Compared to SPR biosensor, LSPR biosensor is theoretically more sensitive and more suitable for small molecular detection (**Figure 1.7**).

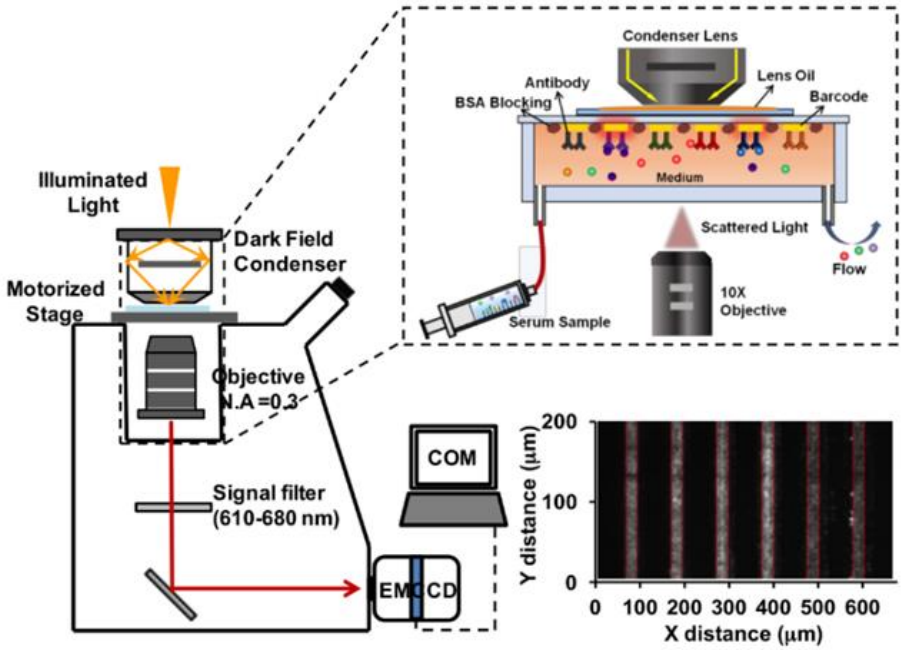

Figure 1.8 Optical setup of dark-field microscope for LSPR microarray immunoassay.[55]

To observe the plasmonic materials, dark-field microscope has been developed to serve as a biosensing technique for monitoring of biological events. In a typical optical setup of a dark-field microscope, an opaque disc placed between the light source and the condenser lens blocks most of the light from the illuminator and only permit light with high angular transmit. Thus, only light refracted, reflected, or scattered by the sample reach the low numerical aperture (**NA**) objective lens for visualization, leading to a bright image on a dark background[106]. A charge-coupled device (CCD) camera is used to take the pictures of the image being observed (**Figure 1.8**). Many modifications, such as different light sources and various CCDs, have been integrated into the dark-field illumination system to improve the signal-to-noise ratio and time resolution for LSPR biosensing.

Surface enhanced Raman scattering (SERS)-based detection

Raman scattering is an inelastic scattering process where the frequency of an incident photon is increased (Stokes Raman scattering) or decreased (anti-Stokes Raman scattering) after interacting with a vibrational molecule. The spectrum of the Raman scattering can help us identify the single molecule based on their vibrational fingerprint including energy and frequencies, which is a very useful technique for biosensing. However, the Raman scattering efficiency of most materials is usually insufficient because only a small fraction of incident light (~1 in 10 million photons) is Raman scattered, contributing to a low scattering intensity and weak biosensing signal[25]. SERS effect was discovered in the 1970s[107,108]. It has been showed that the Raman scattering efficiency can be enhanced by a factor of 10^6 to 10^{11} when the sample is immobilized or near the nanostructured metallic surface (common metals used are gold and silver nanoparticles). Electromagnetic (EM) enhancement is believed to be the main contribution of SERS effect. The interaction between the light and metallic nanostructure can generate a strong LSPR effect which will lead to the resonant absorption or scattering and result in a magnitude enhancement in the local electromagnetic field intensity. While chemical enhancement (CE) involves the charge-transfer process between the metallic nanostructure and analyte molecule[109].

Optical fiber-based biosensors

Fibre-optic biosensor (optrodes) has been developed with biorecognition molecules fixed on a silica optical fibre or a plastic optical fibre where light can transmit along the

fibre to analyte sites. This type of sensor has several advantages in long-distance transmission, sample optical design, low cost, compact construction and so on[110]. The signals can be measured in different optical parameters such as absorbance, reflectance, fluorescence, chemiluminescence, and bioluminescence. Recent research has integrated fibre-optic biosensor with different types of sensing technologies such as SPR, LSPR, or fluorescence to further improve their sensing performance.

1.3 Optical biosensors for single-cell protein secretion analysis and imaging

Unravelling the underlying mechanism by which cells communicate in response to external stimuli will greatly benefit therapeutics and clinic diagnosis[12,111–113]. However, the extremely complex intercellular communication networks in multicellular systems pose great technical challenges to exploit cellular functions and cellular activities. According to the current research, homogeneous cell population shows regular and programmatic response to external stimulation, while individual cells may exhibit enormous differences and heterogeneity[114–116]. That means the heterogeneous cellular behaviors (i.e., protein secretion, cell proliferation, and differentiation) exist not only between different cell population, but also among cells with the same phenotype. The highly dynamic intercellular communication process is usually mediated by the secretion and expression of signaling proteins (i.e., hormones, growth factors, chemokines, cytokines, and neurotransmitters) which identity the specific biological functions and behaviors of cells[117,118]. In clinical, protein secretion level is an important parameter in diseases diagnosis. Traditional techniques such as enzyme-linked

immunosorbent assay (ELISA) measure the overall response from the entire stimulated immune population and indiscriminate the cellular heterogeneity of individual cells as well as their interactions with other cell types, making it difficult to precisely identity their corresponding functions in an immune response[119,120]. The ability to accurately profile temporal and spatial regulation of protein secretion at the single-cell level will provide crucial information about heterogenous functions of cells in the immune system and help to identify intercellular communication mechanisms.

The development of microfluid devices and advances in technology provides many strategies for single-cell isolation and imaging[121,122]. A high spatial resolution is required to distinguish individual cells from each other and to visualize the spatial distribution of protein secretion from multiple individual cells. Besides, a high temporal resolution is also required to identify the secretion dynamics. According to the way that final signal is presented, the single-cell secretion imaging methods can be divided into two formats: homogeneous detection and heterogeneous detection. Heterogeneous assays require one or multiple physical separation steps to remove the unbounded components. This makes a time-consuming and laborious detection process but provides good sensitivity and selectivity. Homogeneous assays can distinguish antigen-biorecognition element complex from unbound fractions without a separation step, providing a quick, straightforward platform for biomolecule detections[123,124].

1.3.1 Heterogeneous techniques

ELISpot/ FluoroSpot assay

After its first introduction in 1983[125], Enzyme linked immune absorbent spot (ELISpot) has been widely used for quantitative cell-secretion analysis. It is a highly sensitive immunoassay that uses the immunosandwich-based method to capture the presence of a specific protein of interest directly secreted from an individual living cell. Stimulated cells are loaded into the plate and attached to the surface coated with primary antibody. Secreted analyte is captured immediately and detected by a secondary enzyme-coupled antibodies. The resulting signal can be detected through enzymatic action to produce a colorimetric substrate[126]. The assay has been used routinely for monitoring of cell-mediated immune response in the development of vaccines. Commonly used IFN-γ ELISPOT assay provide valuable information of individual T-cell responses after stimulation with a specific antigen or peptide. However, traditional ELISPOT assay is limited to one-analyte detection and unable to do the polyfunctional analysis. A dual color enzymatic ELISpot was developed to detect IFN-γ and IL-2 at the same time by introducing two antibody pairs with two different combinations of enzymes and substrates[127]. IL-2 secreting cells show in blue, IFN-γ secreting cells show in red and dual cytokine secreting cells show in purple spots. This method enables a more comprehensive analysis, but color bias caused by overlaps of different colors may lead to an incorrect calculation of dual color spots. FluoroSpot assays have been introduced to improve the multiple-analyte immunoassay. A fluorophore is used to replace the

enzyme in ELISpot. Final colorimetric signal, especially two-color signal, can be distinguished by a fluorescence imaging system, making a more accurate evaluation[128]. In FluoroSpot assays, spot sizes and fluorescence intensity can be quantified by the analysis software to help researcher identify and compare the degree of single-cell immune response. In order to get the best result, spot-based assays usually require optimal cell number (around 2-4 x 10^5 per well) depending on the cell types and estimated frequency of secreting cell . Too many cells will lead to spots overlapping while insufficient spot numbers cannot be used for statistical analyses[129]. Besides, the cells must be incubated in a vibration-free environment to avoid multiple secretion spots from one individual cell.

Micro-/nanowell microfluidics

The development of microfluidic systems including micro-/nanowells and droplet microfluidics have provided numerous advantages in cell isolation and cellular sorting. The miniaturized platform reduces the required analyte volume and offers precise spatial control of individual cells[130]. The detection platforms are limited to a few nano- or picoliters with 1000-10000 arrays of microwells, allowing for isolation of single cell and high throughput analysis. The average number of cells per well can be controlled by adjusting the well size and depth. The device usually integrates a microfluidic chip commonly made of polydimethylsiloxane (PDMS) molded with a large array of microwells and a glass substrate coated with capture antibodies. The assay placed in contact with glass slide defines numbers of subnanoliter culture environments.

Individual cells are confined in each well and secreted protein can be captured by the antibodies coated on the glass slide. After an incubation period, the PDMS layer needs to be peeled off and the glass slide is further processed with fluorescently labeled antibody. Micro- or nanowell assay has been widely applied to screen the secretion profiles of cytokines[131], to select antigen-specific antibodies[132], and to identify cells with interesting phenotype. Especially in vaccine research, profiling the relationship between primary-antibody-producing cells and their secreted antibody can facilitate the vaccine evaluation. Zhu et al. selected individual CD4 T cells from purified blood using anti-CD4 antibodies and isolated them within PEG-coated microwells to profile the IFN-γ secretion. Story et al. performed a corresponding screen to the antibody profiles produced by individual primary B cells from mice after immunization to estimate the specificity, isotype, and apparent affinity[133]. The heterogeneity of antigen-specific antibody-secreting cells has been evaluated to enhance the assessment of B cell immunity in humoral responses. Ogunniyi et al. used microwells to select cell lines which can secretion antibodies of interest. The antibodies produced by mouse hybridomas were captured and generated a protein microarray on the surface of the glass. Fluorescent-labeled antigens were used to revel the target antibodies and corresponding cells can further be retrieved from individual wells[132]. Bradshaw et al. simultaneously detected two kinds of cytokines (IFN-γ and IL-6) and two kinds of antibodies (IgG and IgM) produced from individual human peripheral blood mononuclear cells (PBMCs) by sealed PDMS microwells cultured with human PBMCs on an anti-cytokine coated glass slide and an anti-IgG/IgM coated glass slide in

sequence[134](**Figure 1.9 a**). Due to the possible spectral overlap, the number of analytes in the FluoroSpot-based assays are usually limited within four. The multiplexing capacities can be further improved by combining the immunofluorescence with barcodes strategies[135]. Lu et al. integrated a PDMS microchamber with an antibody barcode slide coated with 42 capture antibodies in 15 serpentine lines to achieve codetection of 42 immune effector proteins from single lipopolysaccharide (LPS)-stimulated macrophage. The combination of spectral (three-color immune sandwich assay) and spatial (barcodes and spots) multiplexing significantly improves the detection ability, allowing for more comprehensive monitoring of functional heterogeneity and cellular immunity[136](**Figure 1.9 b**)

In addition to capture secreted proteins on a glass slide in closed arrays, there is also an open-well format in which the capture antibodies are directly modified on the wells. The in-well protein capture method simplifies the operation process and more binding sides provided by side wells lead to well-defined spatial patterns and concentrated signals. However, the maximum signal in open-well assay is highly dependent on the secretion rate due to diffusion in bulk media, making quantitative analysis impossible[137].

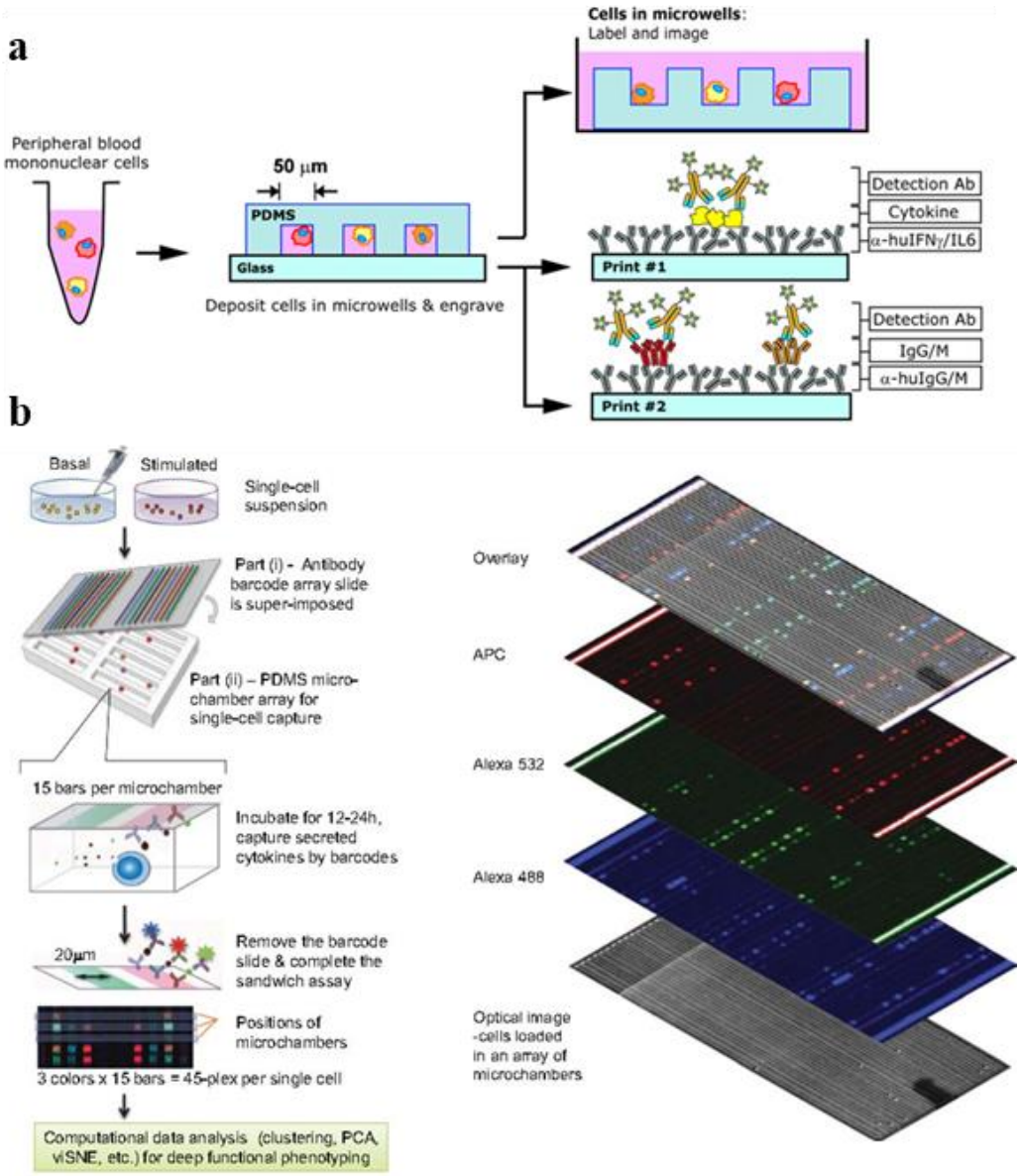

Figure 1.9 Micro-/nanowell microfluidics- based single cell analysis methods.(a). Schematic illustration of the microengraving method for concurrent detection of cytokines/antibodies from human PBMCs[134]. (b) Schematics of high-throughput profiling of single cells in basal and stimulated conditions for 42 secreted effector proteins[136].

Droplet-based microfluidics

In addition to nano-/microarrays, droplet-based microfluidics has also proven to be a promising technique to help isolated individual cells and perform single-cell analysis[138–140]. A droplet microfluidic system uses oil with a surfactant as the continuous phage and water-based solution as dispersed phase, generating water-in-oil microscale droplets in a high-throughput manner[139]. The droplets with volumes ranging from a few femtoliters (fL) to nanoliters (nL) can serve as individual reaction vessels to encapsulate single cells and confine the cell-secreted molecules. By integrating the microspheres or microbeads, the screen of single cell secretion can be performed within the droplet. Konry et.al co-encapsulates cells with microspheres which were conjugated with capture antibodies and detection fluorescence-label antibodies in nano-liter reaction droplets to analyze IL-10 secretion from single T cells[141]. Chokkalingam et.al encapsulated Jurkat T cells in monodisperse agarose droplets together with functionalized cytokine-capture beads. Jurkat T cells were stimulated by PMA and ionomycin overnight in droplets. The secretion of IL-2, TNF-α, and IFN-γ was measured by flow cytometry[116]. Droplet-based microfluidics have shown to dramatically improve the analysis throughput via generating of thousands of droplets per second, allowing more accurate description of the heterogeneity of cell populations[121]. However, uniformly, or predominantly single cell- occupied droplets are hard to generated because cells encapsulated by droplets follow Poisson distribution.

Label-free techniques

Immunosandwich-based assay offers a combination of simplicity, repeatability, and sensitivity for single-cell analysis. However, end-point measurement and laborious labeling process make dynamic screen of cell activities impossible. Besides, long incubation time may cause cell culture adaptation. Label-free techniques are thus developed to monitor real-time cell secretion process. Milgram et al. monitored the secretion of HEL-specific IgG from B-cells hybridoma via SPR imaging. B cell hybridomas were cultured on a gold chip functioned with HEL-antigen. The binding between antigen and analyte will induce changes of refractive index and SPR intensity change which can be monitored in real-time[142]. Stojanović et al. developed the surface plasmon resonance imaging (SPRi) to quantify the VU1D9 antibody production from individual EpCAM hybridoma cells. 53 single EpCAM hybridoma cells were analyzed and showed an average production rate of 0.30 pg per cell per hour (SD 0.25)[143].

Due to the much shorter electromagnetic decay length and a smaller sensing volume, LSPR sensor shows higher sensitivity to molecular binding and less sensitive to bulk effects. Zhu et al. [144]integrated a microwell chip and a gold-capped nanopillar-structured cyclo-olefin-polymer film to detect Interleukin 6 (IL-6) secretion from single Jurkat cells. The IL-6 secretion from the trapped cell can be immediately captured by antibody on the surface of gold-nanostructured film, resulting in red shift of transmittance spectrum peak. The detection limit of IL-6 was proven to be 10 ng/mL(**Figure 1.10a**). Raphael et al. [118]used gold-nanostructured arrays to achieve

quantitative spatiotemporal mapping of secreted proteins from single hybridoma cells. Analyte binding on the surface of gold nanostructures exhibits both a redshift of scattering spectrum peak and an increase in scattering intensity. Gold-nanostructured arrays offered spatial resolution to observe the protein secretion and time resolution is typically 250-400ms. The spatial and temporal information of secreted antibodies enabled estimation of diffusion constant in the range of 0.3 $x10^{-7}$ cm^2/s to 0.5 $x10^{-7}$ cm^2/s. The platform also incorporates transmitted light and fluorescence microscopy to simultaneously monitor cellular morphological changes and fluorescent labelled cell plasma membrane dynamics (**Figure 1.10b**).

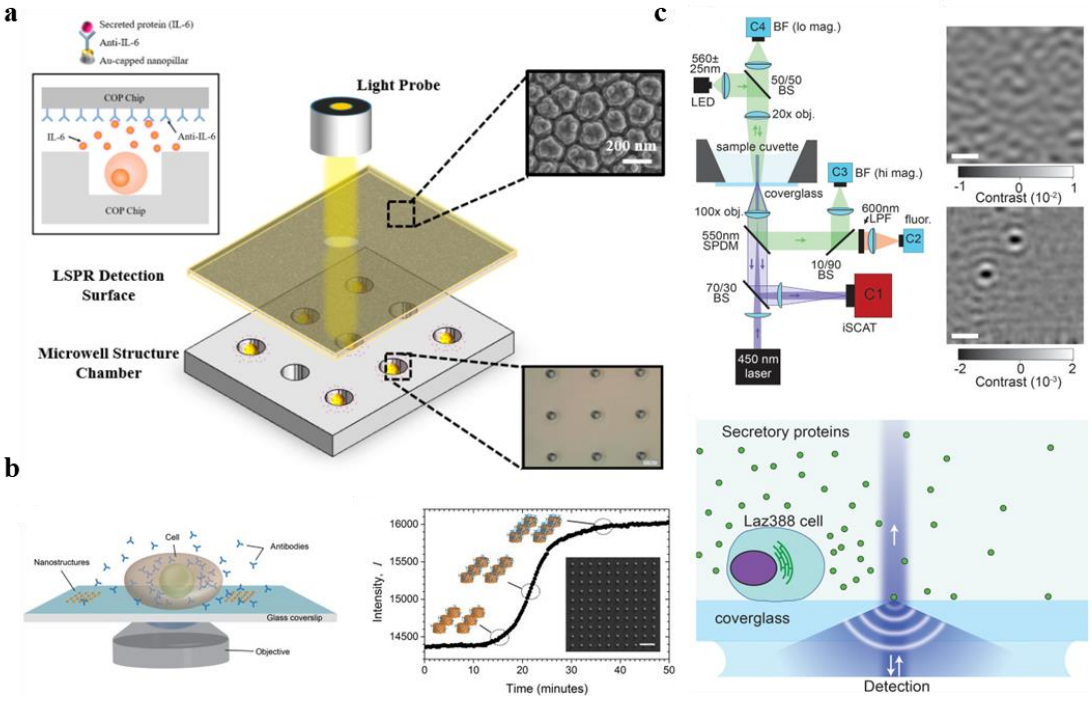

Figure 1.10 Label-free single cell analysis methods. (a) Schematic of the integrated localized surface plasmon resonance (LSPR) cytokine detection platform device[144]. (b) Gold-nanostructured arrays to achieve quantitative spatiotemporal mapping of secreted proteins from single[118]. (c) iSCAT microscopy of an individual cell's secretome[145].

McDonald et al.[145] presented an interferometric detection of scattered light (iSCAT)-based assay to directly visualize IgG antibody release from single Epstein–Barr virus (EBV)-transformed B cells in real time. The signals come from the interference between the scattering proteins and reference beams, generating a diffraction-limited shadows that indicates an individual protein. The molecular weights (MWs) of detected proteins were shown to be in the range of 100−1100 kDa according to an empirical calibration of iSCAT contrast versus molecular weight but proteins within this range are hard to differentiate. The anti-human IgG on the glass could improve the selectivity for IgG detection. In all, the biological specificity of iSCAT is insufficient due to the ubiquitous scattered light from all molecules (**Figure 1.10c**).

1.3.2 Homogeneous techniques

Photonic crystal resonator

A photonic crystal resonator surface composes of silicon nitride (Si_3N_4) or titanium dioxide (TiO_2) with periodically varied regions of high- and low-dielectric constants (photonic band gaps), which allows light in certain wavelength to propagate inside the material. The caused spatially confined resonant wave can interfere the incoming light beam, generating a stationary interference pattern with a localized and amplified optical field. The confined evanescent field is highly sensitive to refractive intensity change caused by the binding events on the sensor surface. Photonic crystal resonator has been demonstrated to be an effective method for real-time cellular imaging with subcellular spatial resolution (2-6um)[146].

Juan-Colás et al. mapped the thrombopoietin (TPO) secretion from individual human HepG2 cells using PCR combining with resonant hyperspectral imaging (**Figure 1.11**). A 150-nm-thick Si_3N_4 film with a grating in a 555nm period was microfabricated on photonic crystal resonator surface by electron beam lithography. To improve the sensitivity, the antibodies were functionalized in a 3D network instead of a single plane on sensor surface using branch glucan dextran, which significantly increase the antibody density. Purified casein serves as a surface block to avoid unspecific binding. The resonance wavelength of every pixel (0.925 μm) can be determined by analyzing the intensity in hyperspectral imaging. The mapping area was 500 x500 um, allowing to image 30 cells simultaneously without compromission of spatial resolution. By tracking the secretion area change, the single-cell secretion rate was calculated to be 22 μm^2/h under a Langmuir adsorption distribution model[147].

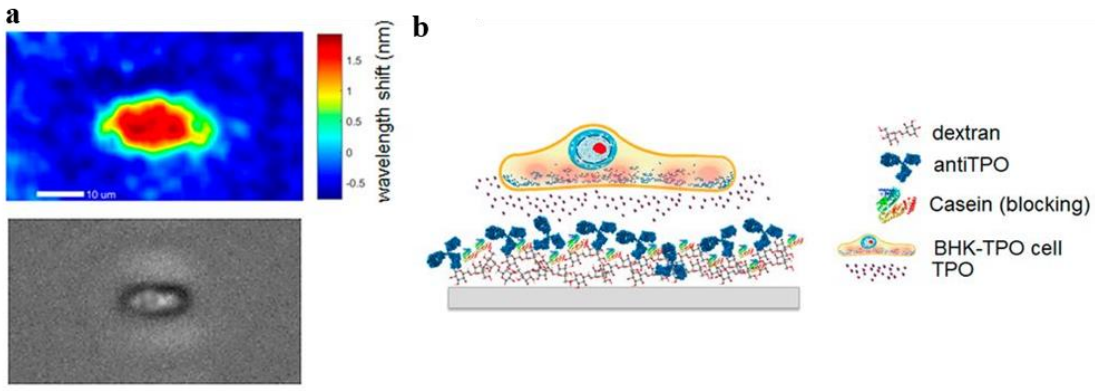

Figure 1.11 Schematic of photonic crystal resonant imaging for monitoring TPO secretion from a single BHK-TPO cell.[147]

Total internal reflection fluorescence microscopy (TIRFM)

Shiraskaki et al. took advantages of near-field excitation in TIRFM and combined it with mocroengraving method to monitor IL-1β secretion process from monocytes after external stimulation[148]. The proteins were captured via fluorescence sandwich immunoassay. However, instead of adding labelled detection antibody after several intensive wash steps, the fluorescent detection antibody in which the fluorophore was excited by the TIRFM is directly added to the cell culture solution (**Figure 1.12**). Target analytes secreted from a single cell are captured by the antibodies immobilized on the microwell bottom and immediately incorporates with fluorescent detection antibody. The immunocomplex formed on the bottom surface is excited by evanescent field of light and generates a strong fluorescent signal. The free fluorescent detection antibody without excitation cannot emit fluorescence. In this way, the immunocomplex can be selectively detected without further wash steps. However, forming an immunocomplex is the rate-limiting step, which compresses the temporal resolution to some degree[122].

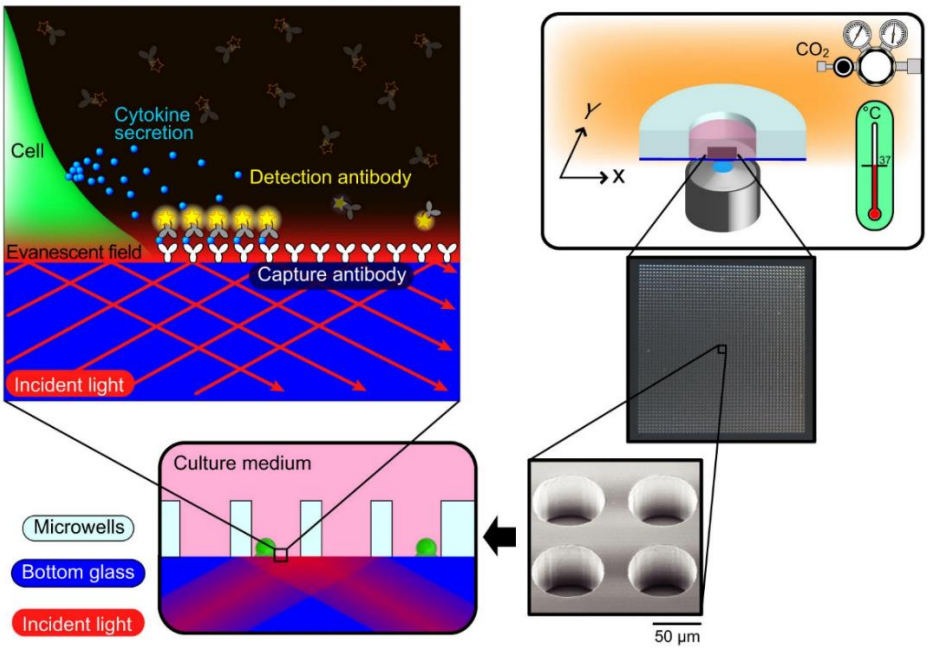

Figure 1.12 Schematics of total internal reflection fluorescence microscopy for the real-time single cell secretion.[148]

Aptamer conformational change

The aptamers have attracted tremendous attentions in the field of biosensor research due to their synthetic and chemical simplicity. Besides, the rapid and reversible conformational change of aptamers can be exploited to achieve real-time sensing with good sensitivity and selectivity[43,44].

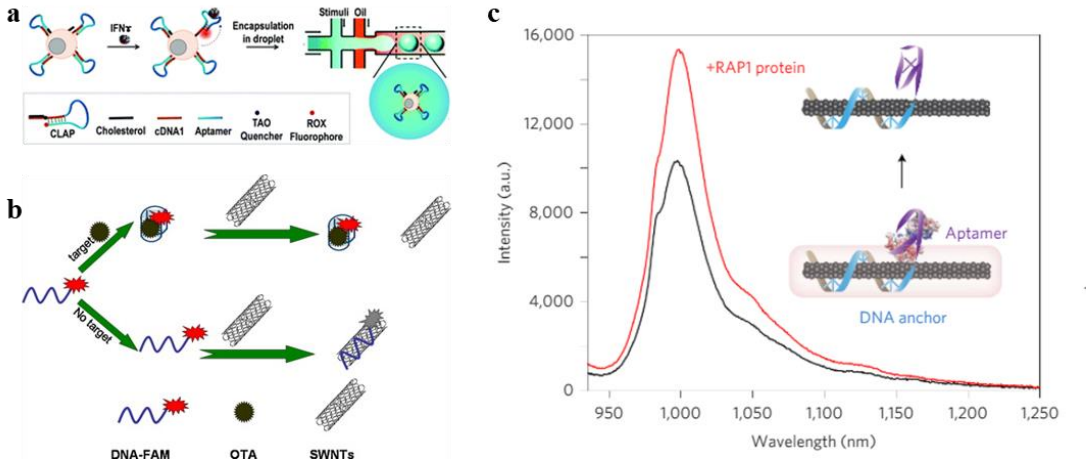

Figure 1.13 Aptamer-based biosensor. (a) Schematic illustration of a T cell-surface aptamer sensor for measuring cytokine secretion at the single-cell level. Binding of the target cytokine will turn on the fluorescence[149]. (b). Schematic illustration of SWNTs based sensing platform for detection of OTA[150]. (c). Schematic representation of aptamer–SWNT construct binding[82].

Qiu et al. developed a cell membrane-anchored fluorescent aptamer sensor combining with a droplet microfluidic platform (**Figure 1.13a**). A ROX fluorophore and a TAO quencher were separately modified on two ends of IFN-γ aptamer. ROX and TAO were self-hybridized into a hairpin structure, resulting in fluorescence quenching. After binding with IFN-γ, the aptamer will suffer from a conformational change, separating two fluorophores and restoring the fluorescence signal. This method has proven to monitor the cytokine secretion at a single-cell level[149]. Guo et al. used single-walled carbon nanotubes (SWNTs) to quench the fluorescence signal from carboxy fluorescein (FAM)-labeled aptamers which can specifically bind to ochratoxin A (OTA) (**Figure 1.13b**). The presence of OTA can separate the SWNTs and the aptamer, leading to the release of fluorescence signal. The detection limit of OTA on this platform was 24.1

nM[150]. Landry et.al also designed a SWNTs-aptamer biosensor to perform the single-molecule detection (**Figure 1.13c**). Compared to quantum dots, SWNTs are the only fluorophores with infinite lifetime and less susceptible to blink on and off, enabling long-term optical monitoring. The aptamer consists of an 'anchor' domain which can adsorb strongly to the SWNT surface, as well as a 'capture' domain which enables to recognize target protein. Protein binding on the SWNT surface can generate a near-infrared (nIR) optical signal with increased SWNT fluorescence intensity, showing a promising method for real-time and single-cell optical detection[82].

1.4 Objectives of research

The dramatically increased demand of medical diagnostics has promoted the repaid development of biosensor technologies. Human immune system is undergoing complex and dynamic change. Biomarkers for disease estimation are required to be analysis in time with high precision and sensitivity. However, traditional sandwich immunoassay cannot serve as a point-of-care immunomonitoring method due to the time-consuming labeling and washing processes.

On the other hand, cellular analysis with accurate, in-depth information of cell characteristics, behaviors, and functions is an emerging need as it offers critical knowledge to modern biology and clinical sciences[12,139,151]. Among the spurring opportunities in cellular analysis, unraveling cell-to-cell communication has emerged as a crucial step to reveal the underlying mechanisms in regulation of cell proliferation, transcription, migration, differentiation, and apoptosis. Intercellular communication is

achieved mainly through cell secreted signaling molecules including proteins, small peptides, amino acids, nucleotides, steroids, retinoids, fatty acid derivatives, and even dissolved gases such as nitric oxide and carbon monoxide. Among them, cytokines, a broad category of small proteins produced by many of cell populations, has been widely investigated as they are critical for the regulation of immune response and intercellular communication[152,153]. These molecules travel in the extracellular space, bind to target sites, and then elicit corresponding responses via different signaling pathways. Impaired transportation of signaling molecules leading to malfunction of intercellular communication has been evidenced to present in varied diseases such as cancer, autoimmune disorders, diabetes and more[154–156]. Thus, to decipher the message carried during intercellular communication and probe how cells "talk", it is essential to track and understand the spatial/temporal distribution and the fate of secreted biomolecules in response to external stimulation, which has enormous implications for cell biology, stem cell regenerative medicine, cancer therapy and immune disease diagnosis. Thus, there is an urgent need for the development of novel technology that permits accurate quantification and mapping of the secretion patterns from target individual immune cells in a dynamic manner.

Over the last two decades, plasmonic biosensors have been extensively studied owing to their proven advantages in real-time monitoring with minimal interference and high signal stability[1,63,157–159]. Comparing to the conventional SPR sensor limited by the bulky system and low spectral resolution, metal nanoparticle based localized surface

plasmon resonance LSPR biosensors have been perceived as emerging label-free techniques enabled by recent advances in nanotechnology[55,144,160]. The main purpose of the whole project is to advance our understanding of intercellular communication in the immune system by pushing the frontiers in the cutting-edge disciplines of biomaterials and bionanotechnology. We aim to develop a robust LSPR-based biosensor platform which permits accurate and real-time detect biomolecules, serving for disease diagnosis and medical research such as immune response monitoring. Furthermore, a novel synthetic hybrid nanomaterial – aptamer linked nanoplasmon ruler- was fabricated to achieve direct imaging of cytokine secretion profile from a single immune cell upon external stimulation in a high spatiotemporal resolution. Finally, the developed hybrid nanomaterial will be employed to monitor the cytokines produced from the activated commanding cells and to track their diffusion and interaction with the target immune cell in a cocultured cellular environment. We believe the knowledge obtained from this study will facilitate a more comprehensive understanding of the immune intercellular network, unlocking the potential to transform the experimental studies into an information-rich science not only in immunology but beyond. To achieve the goal, this research is focused mainly on the five aspects:

1. **Surface function of nanoparticle structures.**

   We synthesized different shapes and sized of Au nanostructures (nanorod, nanosphere, and nanobipyramid) and constructed COMSOL finite element

analysis to predict the plasmonic responses and scattering behaviors of functionalized nanostructures in an electrochemical field.

2. **Self-assembled plasmonic gold nanorod microarray for rapid, multiplex cytokine detection.**

   We employed a simple microfluidic assisted patterning technique for gold nanorods (AuNRs) that can form self-assembled AuNR barcode structures on a cover glass substrate. By integrating an emerging dark-field LSPR imaging technique, we can map the target cytokine binding by selectively collect the increased scattering light from the LSPR AuNR barcode arrays using specific band-pass filter. This nanoplasmonic biosensing approach allowed quantitative multiplexed measurement of target cytokines (IL-6, TNF-α, IFN-γ) with concentration ranging from 1~5000pg/mL within 30min.

3. **Design and synthesize the aptamer linked nanoplasmon ruler for real-time, multiplex cytokine detection with high sensitivity and selectivity.**

   We have developed a self-assembled 'nanoplasmon ruler' sensor with a dimmer of noble metal NPs conjugated by a designed aptamer (one strand DNA structure), which has shown great potential in detecting secreted biomolecules with superior sensitivity and specificity at real-time. We uniquely integrated optical simulations, advanced nanomaterial fabrication and state-of-art dark field imaging technique to design, synthesize, characterize and optimize the proposed nanoplasmon ruler structure. We fabricated the hybrid dimer structure using nanoscale AuNPs conjugated by aptamers with specific sequence and

length toward target cytokines. The formation of the architecture and the subsequent binding of cytokines onto the plasmon ruler have been examined and optimized to improve the detection efficiency. The parameter space to be mapped includes a) NP size, b) NP surface function, c) interparticle distance (aptamer length), and d) stoichiometric particle-aptamer ratio. Results from part will offer valuable information on the key parameters affecting the desired nanoplasmon ruler formation, facilitating the development of a real-time, multiplex cytokine mapping technique with high sensitivity and selectivity.

4. **Evaluate the nanoplasmon ruler for mapping single immune cell cytokine profiling.**

   we have examined the assembled nanoplasmon ruler for real-time monitoring the cytokine secretion patterns from activated individual immune cells. We constructed the plasmon ruler nanostructures serving as imaging elements in a micro-chamber and demonstrate in-situ multiplex single-cell function analysis by real-time mapping the cytokines secreted by individual immune cells. The parameter space to be mapped includes a) scattering intensity, b) limit of detection (LOD), c) multiplicity and specificity, d) stimulant concentration, e) time response, f) cytokine secretion rate, and g) diffusion pattern (diffusion anisotropy and diffusion coefficient). Results from this part will establish a new approach on understanding the secretion profile from a single immune cell and serve as a basis for elucidating the intercellular communication in the immune cell network.

5. Extrapolate the nanoplasmon ruler for intercellular communication

We further evaluated performances of nanoplasmon ruler for intercellular communication in the biological network. Especially, we mimicked a microenvironment for CAR-T cell therapy by coculturing CAR-T cell, B cell lymphomas, and macrophage in vitro and investigated CAR-T cell -induced cytokine release syndrome (CRS). Isolated paired immune cells as well as their secreted cytokines will be real-time monitored in a cocultured system. The cytokine secretion patterns were imaged and assessed in real-time as the major indicators of cell “vision” and “response” through intercellular communication. The parameter space to be mapped includes a) immune cell type, b) cocultured cellular environment, c) directional cytokine diffusion, d) target immune cell response, and e) cytokine secretion pattern. This part will demonstrate the first direct visualization of how cells “talk” in the intercellular network and thus provide comprehensive information on the cell-to-cell communication for a more advanced cell therapeutics.

Chapter 2

The Influence of Plasma Protein Corona on Immune Cell Association and Cytokine Secretion Induced by Oligomeric and Fibrillar Beta-Amyloid.

2.1 Introduction

Beta amyloid (Aβ) originates from amyloid precursor protein (APP), an integral membrane protein expressed in tissues and especially in the brain[161].The APP is cleaved off by β and γ secretases, yielding two major peptide products Aβ1–40 and Aβ1–42. Among the two peptides, Aβ1–42 is more hydrophobic due to the two additional amino acids of isoleucine and alanine at the C-terminus and is considerably more cytotoxic due to its higher tendency in aberrant aggregation. The extracellular amyloid deposits of Aβ and the intracellular tangles of tau are two histopathological hallmarks of Alzheimer's disease (AD), a primary form of neurological disorder in aging populations[162].

While Aβ plaques are often located in the brain tissues of AD patients post mortem, the peptide itself can also be traced in cerebrospinal fluid (CSF) and the circulation[163]. The relationship between the peptide levels in the brain, CSF and plasma in healthy and diseased individuals, however, remains unclear[164]. Compelling evidence has shown the transport of Aβ by serum albumin and apolipoproteins in the blood plasma[165,166], likely due to the poor solubility of the peptide as well as the chaperone-like capacity of serum albumin[167–169]gainst the conformational changes of Aβ. Furthermore, while specific

receptors on microglia and monocytes/macrophages in the brain may determine the clearance of extracellular Aβ peptides through non-inflammatory phagocytosis or pro-inflammatory cytokine secretion[170–174], adherence of complement C3b to complement receptor 1 (CR1) of erythrocytes is a mechanism hypothesized for the peripheral clearance of Aβ[175].

The literature has suggested the use of Aβ in the blood as an effective indicator for the early diagnosis of AD. The effect of human serum albumin (HSA) on the reduction of α-synuclein aggregation (associated with Parkinson's disease) has been reported recently[176]. However, the associations of plasma proteins and blood cells with Aβ in its major aggregation forms, namely, oligomers and amyloid fibrils (abbreviated as AβO and Aβf hereafter, to refer to the chiefly oligomeric and fibrillar forms of the peptide), remain unclear. Furthermore, the immune responses of blood cells to amyloidogenic peptides and their aggregates have not been systematically investigated.

Here, we performed a label-free microfluidic-based LSPR immunoassay that achieved real-time detection of cytokines, i.e., interleukin 6 (IL-6) and tumor necrosis factor alpha (TNF), by human monocytes and lymphocytes exposed to AβO and Aβf in the presence and absence of plasma proteins. The results implicated a significant role of plasma protein corona in shaping the cell binding affinity and toxicity of amyloid protein aggregates, and demonstrated a convoluted relationship between amyloidosis and inflammation in AD.

2.2 Experiments

Transmission electron microscopy (TEM). For TEM imaging, 5 μL of AβO and Aβf (each of 50 μM), plasma proteins, Aβo, and Aβf in interaction with plasma proteins were pipetted onto copper grids (400 mesh, glow-discharged for 15 s; Formvar film, ProSciTech) and let adsorb for 1 min. After removing unbound samples by filter paper the grids were rinsed with 10 μL of Milli-Q water. The grids were then negatively stained with 5 μL of 1% uranyl acetate (UA) for 30 s and blown dry. The samples were imaged by a transmission electron microscope (Tecnai G2 F20, FEI, Eindhoven, The Netherlands) under an electric potential of 200 kV. Images were acquired with a CCD camera (UltraScan 1000, Gatan).

Thioflavin T (ThT) kinetic assay. A kinetic assay on peptide fibrillization was conducted using 50 μM Aβ and 100 μM ThT dye pipetted into a 96-well plate (Costar). Changes in ThT fluorescence, indicating the β-sheet content in the sample, were recorded at 37 °C till the saturation phase after 60 h by a plate reader (PerkinElmer EnSight HH33400; Ex/Em: 440/485 nm). The assay was done with triplicate for each sample condition.

Cell culture and toxicity assay. SH-SY5Y neuroblastoma cells were cultured in Dulbecco's Modified Eagle Medium: Nutrient Mixture F-12 (DMED/F12, ATCC) with 10% fetal bovine serum (FBS). For the viability assay, a 96 well plate (Costar) was pretreated with poly-L-lysine (Sigma, 0.01%), incubated at 37 °C (5% CO2) for 30 min, and washed with phosphate buffered saline (PBS) thrice. Approximately 60,000 cells

were added to each well and incubated at 37 °C and 5% CO_2 to reach 80% confluency. 1 μM propidium iodide (PI) dye in fresh DMEM/F12 was added and incubated with the cells for 30 min. After optimization of concentrations, samples of 20 μM Aβ in the form of oligomers or fibrils were added to the wells. After 15 h of treatment, the cell viability was read by Operetta (PerkinElmer, 20× lens, numerical aperture: 0.7) at 37 °C with 5% CO_2. The PI-positive apoptotic cells were counted by the mapping function of the instrument. 9 reads per well for samples of triplicate were acquired. Untreated cells were imaged as the control.

Aβ preparation. Hexafluoro-2-propanol (HFIP)-treated human Aβ1–42 (AnaSpec, sequence, AIAEGDSHVLKEGAYMEIFDVQGHVFGGKIFRVVDLGSHNVA; purity, HPLC ≥ 95%; abbreviated as Aβ hereafter) was used in preparation of the two aggregating states of Aβ. Specifically, AβO was rendered by incubating the freshly dissolved Aβ in 0.003% NH_4OH buffer at room temperature for 30 h, while Aβf was obtained by incubating the peptide at 37 °C for more than 60 h.

Localized surface plasmon resonance (LSPR) immunoassay

Cells culture. Jurkat human T cells (ATCC®CRL-2901TM) were cultured in RPMI-1640 medium (ATCC® 30-2001™) with 200 mcg/mL G428 and 10% FBS (ATCC® 30-2020™). The cells were incubated at 37 °C with 5% CO2 in a Cell Culture Incubator (Thermo Scientific). Epstein-Barr virus (EBV) transformed human B lymphoblast (ATCC® CRL-5969™) were cultured in RPMI-1640 medium with 10% FBS. Human THP-1 cells (ATCC® TIB-202™) were cultured in RPMI-1640 medium with 0.05 mM

mercaptoethanol and 10% fetal bovine serum. The culture medium was renewed every 2 to 3 days to maintain the suitable concentration of 1×10^5 to 1×10^6 cells/mL. The cells were collected through centrifugation at 125 g for 5 min, and then resuspended in fresh culture medium

PDMS microfluidic-pattering layer preparation. The mold wafer for parallel microfluidic channels (200 μm (W) x 2.5 cm (L) x 50 μm) was fabricated on a silicon substrate by photolithography. Then, a liquid PDMS (Polydimethylsiloxane, Sylgard-184, Dow Corning) pre-polymer and cross linker were mixed (10:1) and degassed twice, and then poured onto the silicon mode wafer. The device was incubated in an over for 6h at 70°C. After that, the PDMS microfluidic-pattering layer can be peeled off from the mold wafer easily. Inlets and outlets of the follow channels were created by a hole puncher with 1mm diameter.

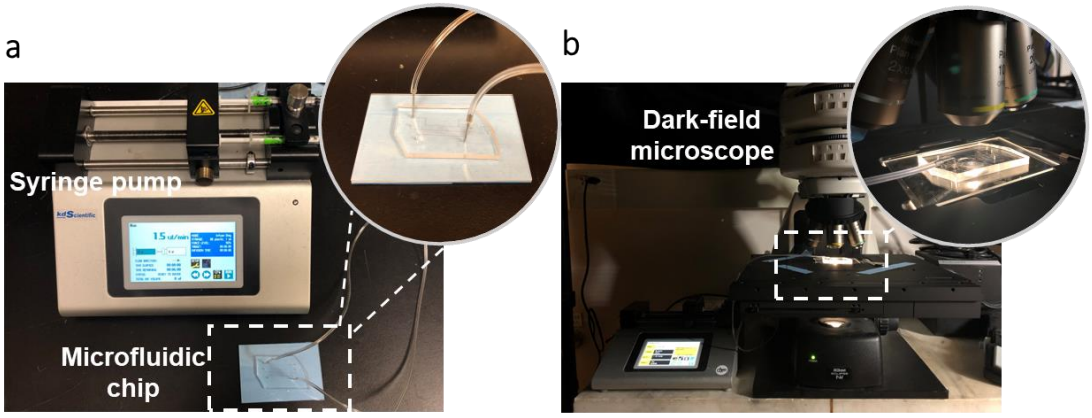

Figure 2.1 Experimental instruments for Au nanorod barcode patterning and real-time cytokine detection. (a). Au nanorod barcode patterning process. AuNRs and functional chemical solution were loaded into microfluidic chip using a syringe. The liquid speed was precisely controlled by a syringe pump. (b). LSPR immunoassay

process under a dark-field microscope. Prepared LSPR chip was mounted on the sample stage. Scattering light was collected by a 10x objective lens. Dark-field images were captured by a EMCCD camera and analysed by a customized MATLAB code.

Au nanorod barcode patterning. Glass slides were first washed by deionized (DI) water and immersed in Piranha solution (H_2SO_4:H_2O_2 = 3:1 v/v) for 10 min. The cleaned slides were rinsed with DI water and kept in an ultrasonic bath for 15 min, and then thoroughly wash with DI water. The prepared glass slides were fully dried at 80°C. To create negatively charged surface, oxygen plasma at 60W (PE-50, Plasma Etch Inc.) was applied onto glass substrate for 4 min. The PDMS microfluidic-pattering layer was quickly attached onto the surface of plasma-treated glass for Au nanorod (NR) barcode patterning. CTAB-coated AuNRs (Nanoseedz, NR-40-650-10) solution was loaded into the channels and incubated overnight. The Positively charged AuNRs were immobilized onto the glass surface through electrostatic interactions to form the barcode pattern on the glass substrate. Unbound AuNRs were washed away by DI water, The PDMS patterning layer was then carefully removed and a free PDMS flow channel layer (from the same mask) was attached perpendicularly to the AuNRs barcode patterns. 1 mM of 11-Mercaptoundecanoic acid (Sigma-Aldrich, USA) was loaded into channels to replace the CTAB layer on AuNRs surface and incubated overnight. 0.1 M NHS (N-hydroxysuccinimide, Thermo Scientific) and 0.4 M EDC (1-Ethyl-3-(3-dimethylaminopropyl)carbodiimide, Thermo Scientific) prepared in 0.1 M MES (2-(N-morpholino)ethanesulfonic acid, Thermo Scientific) were mixed in equal volume. The mixture solution was then loaded into microfluidics channels, and then incubated for

40 min. Probe antibody solutions (anti-human IL-6 or anti-human TNF-α, ebioscience, USA) in 50μg/mL were injected into the channels and incubated for 1 h. All the excessive chemicals and molecules in each step were washed away by 1x PBS at 1.5 μL/min for 6 minutes (**Figure 2.1a)**.

Real-time cytokine detection. Immune cells (T cells, B cells, or THP-1 cells) were resuspended in human plasma (Innovative Research) and RPMI-1640 at 1×106 cells/mL, respectively. The immune cells were incubated with Aβo and Aβf of 5 μM, 10 μM, and 15 μM final concentration for 2h at 4 °C and 37 °C. The immune responses of human THP-1 cells, human Jurkat T cells and human B cells were investigated after stimulations with Aβo and Aβf. After 2h of incubation, the culture medium was collected and loaded into the prepared LSPR immunoassay chip (fabrication and measurement details in supporting information) for the detection of secretory cytokines from the immune cells (**Figure 2.1b**).

2.3 Results and discussion

2.3.1 Interactions of Aβ aggregates with plasma proteins

Due to the kinetic nature of amyloidosis, which is a convolution of both primary and secondary nucleation followed by elongation and saturation, the AβO and Aβf samples were not pure oligomers or fibrils but were inclusive of a collection of minor heterogeneous aggregates. The interaction of Aβ with blood components is of intense interest as it offers a model to understand the immune response to amyloid proteins. Previously, Kuo et al. reported the interactions of fresh Aβ1-40 and Aβ1-42 with plasma

proteins[177]. Here our TEM imaging of plasma proteins Aβo and Aβf with and w/o plasma proteins confirmed the two aggregation states as globules and fibrils (**Figure 2.2a&b**), respectively. TEM imaging showed the morphologies of plasma proteins (**Figure 2.2c**) and their associations with the Aβ species (**Figure 2.2d&e**). Specifically, in the case of Aβf, a protein "corona" was rendered upon the peptide incubation with plasma proteins, mediated by H-bonding and electrostatic interactions between the Aβf surface moieties and the amphiphilic plasma proteins[178].

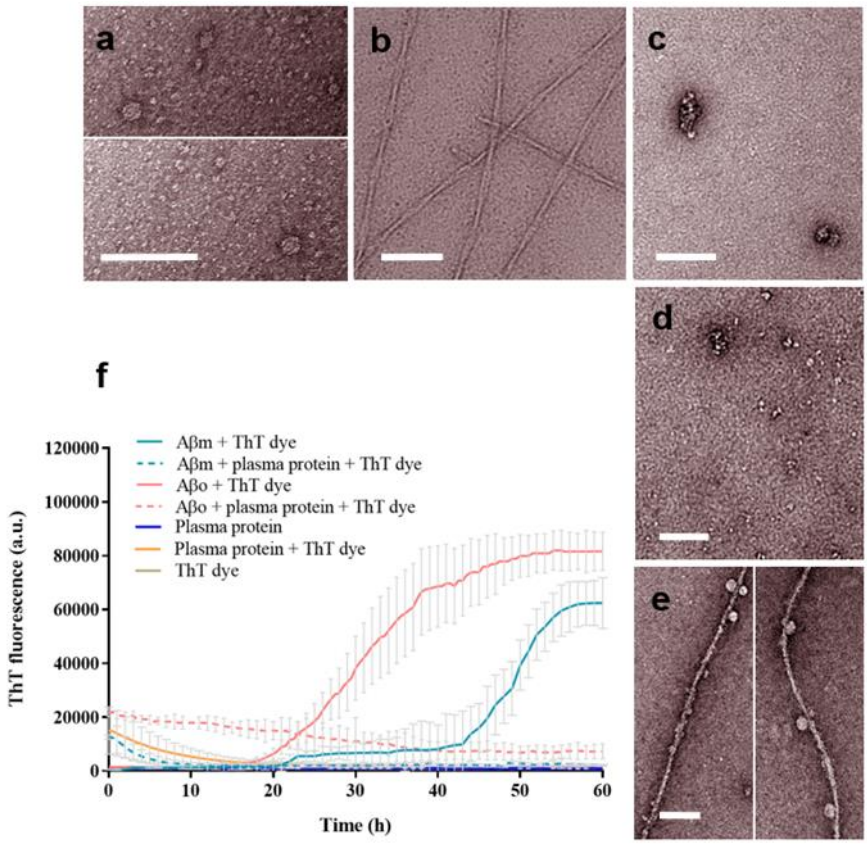

Figure 2.2 TEM imaging and ThT kinetic assay of Aβ fibrillization. TEM images show the following structures: (a) Aβo, (b) $A\beta_f$, (c) plasma proteins, (d) Aβo with plasma proteins and (e) $A\beta_f$ with plasma proteins. The experiments were performed in triplicate. The error bars indicate the standard deviations of averaged data sets. Aβ concentration: 50 μM (ThT assay, 37 °C) and 20 μM (TEM, at room temperature). Scale

bars: 100 nm. (f) ThT kinetic assay of Aβm and Aβo fibrillization with and without plasma proteins.

2.3.2 Aβ aggregation kinetics and cytotoxicity

The ThT kinetics of Aβm and AβO displayed a nucleation phase, followed by an elongation phase to a saturation phase of the peptide after ~60 h (**Figure 2.2f**). This result is consistent with the Aβ fibrillization in the literature[179–181]. In the presence of plasma proteins, interactions of both Aβm and AβO with the proteins blocked the addition of Aβ monomers to inhibit the further assembly of the oligomers into amyloid fibrils.

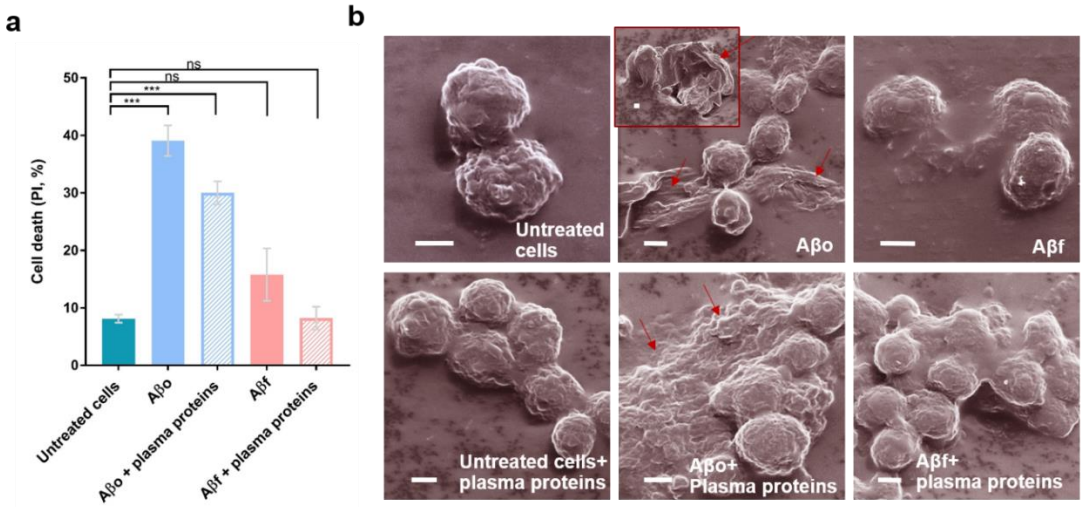

Figure 2.3 Viability and morphology of neuronal cells exposed to the Aβ species with or without plasma proteins. (a) SY5Y cell toxicities exposed to Aβo and $Aβ_f$. PI: propidium iodide. (b) Helium ion microscopy indicates the toxicity of Aβ species with and without plasma proteins. Arrows indicate the deformation of cell membranes induced by Aβo. Cells were treated with the Aβ species for 2 h, with or without plasma proteins. The experiment was performed in triplicate and error bars indicate standard deviations (ns: $P > 0.05$ and ***: $P \leq 0.001$). Aβ concentration: 20 μM. Scale bars: 2 μm.

Aggregation of amyloid proteins is a hallmark of neurodegenerative diseases and type 2 diabetes. Aβ aggregation is associated with neuronal cell degeneration[182–184] and the Aβ oligomers are considered to be the most toxic species[185]. The cytotoxicity of Aβ in this study was consistent with the literature and with the aggregation inhibition of Aβ in interaction with plasma proteins (**Figure 2.3a**), revealing suppressed toxicity of $A\beta_O$ with plasma proteins (39 ± 2.6% without plasma proteins and down to 30 ± 2% with plasma proteins). In comparison, Aβf induced a modest 13% cytotoxicity which was not affected by plasma proteins. The morphologies of SH-SY5Y neuronal cells exposed to the two Aβ aggregating species were examined with helium ion microscopy (HIM). HIM utilizes a helium ion source to excite a small sample volume with a large depth and is advantageous to conventional scanning electron microscopy in both resolution and image brightness. Consistent with the viability assay, significant damage including membrane deformation and blebbing of the SH-SY5Y cells were observed upon their exposure to AβO (**Figure 2.3b**), while such damage was reduced in the presence of Aβo incubated with plasma proteins. In comparison, no damage was evident when the cells were exposed to Aβf with or w/o plasma proteins.

2.3.3 Aβo- and Aβf-induced immune responses with and without plasma proteins

The deposition of Aβ peptide has been revealed to trigger a range of inflammation responses from immune cells to express cytokines and chemokines[186]. Laboratory and clinical investigations have shown evidence of increased release of proinflammatory cytokines such as TNF-α, IL-6, IFN-γ and IL-18 in both the brain and the plasma of AD

patients[186,187]. In addition, plasma proteins including human serum albumin (HSA) have been demonstrated to inhibit the aggregation of Aβ and participate in AD-related inflammatory responses in the brain endothelium. HSA binds 90% of plasma Aβ and could potentially affect their molecular distribution and pharmacokinetics[188]. Unveiling the influence of plasma proteins on Aβ peptide-induced immune response and understanding the pro-inflammatory cytokine release profiles upon stimulation may offer new insights into Aβ-induced cytotoxicity to facilitate the development of AD therapy. Conventional cytokine detection methods such as enzyme-linked immunosorbent assay (ELISA) usually require laborious regent processing procedures, including multiple steps of staining, washing, and blocking, and posing challenges in real-time analysis of dynamic molecular release processes[189]. In this study, we performed a label-free microfluidic-based LSPR immunoassay for real-time detection of multiple cytokines secreted by three types of immune cells, after co-culturing the cells with AβO or Aβf. The immune responses induced by AβO and Aβf with and without plasma proteins were assessed by the levels of cytokine secretion.

Immune cell lines (T cells, B cells, or monocytic cells) were incubated with the two types of Aβ aggregates in human plasma and RPMI medium at 4 and 37 °C, respectively. LSPR immunoassay chips consisting of antibody-functionalized gold nanorods (AuNRs) were used to detect TNF and IL-6 secreted by the immune cells (**Figure 2.4a**). Cytokine binding with AuNR–antibody conjugate altered the localized-refractive index and enlarged the scattering cross section of the nanostructure. The plasmon resonance

gave rise to a red shift in the scattering spectrum, coupled with an increased scattering intensity (**Figure 2.4b**). Images of the sensing spot arrays were acquired in real-time by an ultrasensitive electron multiplying CCD (EMCCD, Photometrics). The scattering intensities of the sensing spots were processed by MATLAB and converted to cytokine concentrations based on pre-established calibrations (**Figure 2.4c**).

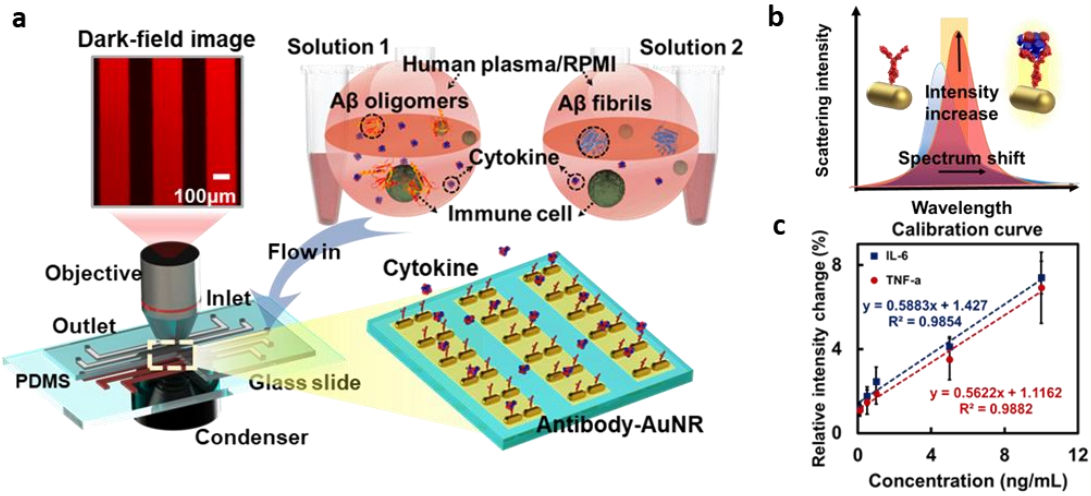

Figure 2.4 Schematics of the LSPR immunoassay. (a) LSPR immunoassay on Aβo- and Aβf-induced immune responses. Human immune cells (T cells, B cells, or THP-1 cells) were incubated with Aβo and Aβf in human plasma or RPIM medium, respectively. The cellular responses were compared by detecting secreted concentrations of TNF and IL-6 in the medium using LSPR microfluidic chips in dark field. (b) Cytokine binding with AuNR–antibody conjugates altered the local refractive index and scattering cross section of the nanostructure, giving rise to a red shift in the SRP peak coupled with an elevated scattering intensity. The cytokines secreted were determined by changes to the scattering light intensity using an EMCCD. (c) Calibrations of cytokines TNF and IL-6 showing the relative intensity changes of the LSPR barcode with varied cytokine concentrations. The trendline equations and R2 values are indicated. AuNR: gold nanorod.

More pronounced inflammatory responses were observed for immune cells exposed to the Aβ species at 37 °C than at 4 °C due to higher cell activity and metabolism ( ). Specifically, AβO induced overall heightened immune responses as compared to Aβf at 37 °C, suggesting stronger interaction and toxicity of the former with the immune cells. THP-1 cells (as a model system for monocytes), in particular, displayed a prominent pro-inflammatory cytokine secretion upon exposure to AβO, consistent with the observed monocyte association with the Aβ aggregate.

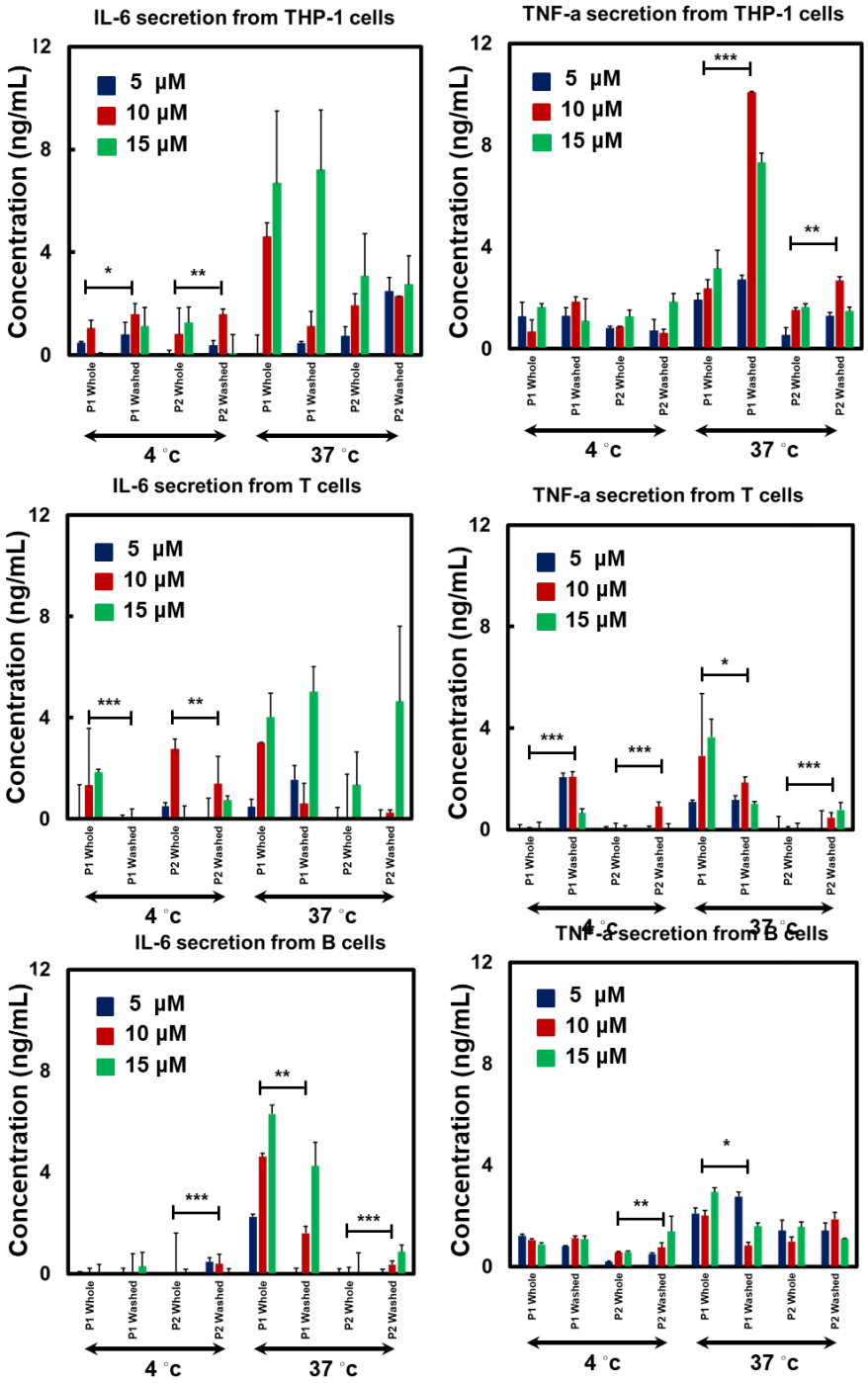

Figure 2.5 Aβ-induced immune responses of human immune cells Cytokine secretion profiles for THP-1 cells, T cells, and B cells incubated with Aβo and Aβf in human plasma or RPMI-1640 medium. The assay was performed in triplicate. The error bars indicate standard deviations (*, $P < 0.05$; **, $P < 0.01$; ***, $P < 0.001$; and ****, $P < 0.0001$).

Contrasting effects of plasma proteins on AβO- and Aβf-induced immune responses were observed at 37 °C. Whereas Aβf displayed overall suppressed immune responses after interacting with plasma proteins for all three types of immune cells, AβO-associated immune toxicity was mostly promoted in the presence of plasma proteins, except for TNF expression from the THP-1 cells. Such differential immune toxicity of Aβ depositions can be attributed to two main factors: size and hydrophobicity, correlating to the capacities of the Aβ species and their protein-coronae to bind and penetrate the immune cell membranes. It was reported that amylin oligomers of smaller size and higher hydrophobicity elicited a stronger immune response than their counterparts with similar size but less solvent-exposed hydrophobic residues[190,191]. As such, binding of AβO with serum albumin in plasma proteins inhibited the peptide aggregation to maintain their small size and surface hydrophobicity, facilitating immune cell interactions to elevate immune responses[192]. In contrast, Aβf with lower structural plasticity and less exposed hydrophobic residues tends to bind to plasma proteins via charged and polar groups, resulting in a larger colloidal-like amyloid-protein corona while displaying weaker toxicity. It should be noted that TNF expression from THP-1 cells could be promoted through receptor-specific signaling pathways such as the Mac-1 receptor[193]. Hence, the formation of an AβO-plasma protein corona could potentially shield the exposed AβO activation motifs and drastically prohibit TNF secretion. Such a phenomenon was not observed for Mac-1 receptor-negative T-cells and B-cells.

2.4 Conclusions

Amyloidosis has been extensively investigated for the past decades, driven by the urgent need to find a cure for amyloid diseases[161]. Much of this research emphasis has been centered on the amyloid hypothesis[194] and its pathological implications. The oligomers are widely viewed as the most toxic products of protein aggregation as established by extensive in vitro and in vivo data[195,196], while amyloid fibrils are generally considered as benign despite experimental discrepancies[197]. Here, we have revealed a convoluted relationship between the amyloidosis and immunogenicity of Aβ1–42, using a label-free microfluidic-based LSPR immunoassay. The LSPR immunoassay revealed elevated cytokine secretion of immune cells against both AβO and Aβf, especially more so for the oligomers. The Aβf-elicited immune response was screened by plasma proteins, via a protein corona mediated by nonspecific forces. The oligomers, on the other hand, maintained their capacity for immune cell association due to their small size and finite hydrophobicity. This study has implicated the intertwined relationship between the amyloidosis and immunogenicity of Aβ, two aspects underlining the pathological cascade and therapeutic solution of AD[198].

Chapter 3

Nanoplasmonic Mapping of Single-Cell Cytokine Secretomic Signatures in CAR T-Cell Cancer Therapy

3.1 Introduction

CAR-T cell immunotherapy is a novel treatment modality for cancer. It genetically modifies T cells to express CD 19-targeted chimeric antigen receptor (CAR) which is against a B-lineage antigen[199]. The adoptive T-cell transfer has shown a high rate of complete remission in clinical trials on patients with relapsed/refractory B-cell precursor acute lymphocytic leukemia (B-ALL)[200–202]. Variable responses have also been reported when treating other B-cell malignancies. However, the fundamental mechanistic that contributes to the variations remains unclear[203,204]. Moreover, the recognition of tumor antigen by CAR induces an elevated secretion of acute-phase proteins and stimulatory cytokines, known as cytokine release syndrome (CRS)[202]. Severe CRS, if left untreated, will lead to reduced efficacy of the treatment and life-threatening side effects due to over expression of immunosuppressive and pro-inflammatory cytokines[205]. Remarkably, the elicited cytokine profile under CRS varies among patients and even among individual cells, posing significant challenges to control, monitor and standardize the immunotherapy. These emerging clinical demands highlight the pressing need for high-resolution single-cell cytokine secretomic signatures for systematic evaluation of the immune cytokine network to provide new insights into the development of efficacious and safe CAR T-cell immunotherapy.

However, the CAR T-cells and other immune cells in the tumor microenvironment experience highly dynamic and transient alternations and show heterogeneity during the secretion of cytokines. Recent evidence further suggests that localization and segregation of cytokines are crucial to the successful initiation and propagation of immune cell communication and, just as importantly, to the termination of the associated responses in maintenance of immune tolerance during immunotherapy[206] Acquisition of appropriate functional outcomes from such complex intercellular networks requires accurate measurement of secretory cytokines at single-cell level with dynamic spatial and temporal information. Standard approaches, such as enzyme-linked immunospot (ELASA/ELLSpot)[207,208] polychromatic flow cytometry[209] or intracytoplasmic cytokine staining, rely predominantly on immunological analytical methods. These platforms can provide multiparametric, albeit static information of immune cells traits of interests, ranging from average measurements of a population to precise and repeated measurements at single-cell level. Nonetheless, the multi-step staining, washing and blocking processes have constrained those to be only able to resolve the variations of cytokine production at a time snapshot. Most importantly, no techniques, thus far, can probe the "footprint" of cytokine secretion from single immune cells by localizing individual cytokine binding events in real-time, which has become a major obstacle in characterizing protein secretomic signatures and investigating the interplay between these cells via cytokine signalling on tumour growth and progression[210–212]

Over the last two decades, plasmonic nanoparticle (PNP) biosensors have emerged as promising tools for label-free, real-time detections of biomolecules owing to their unique local environment dependent optical properties[213]. In particular, nanoplasmon ruler, self-assembled PNP dimmers conjugated by a biomolecule linker (typically DNA, RNA or peptide), has shown great potential in chemical and biological sensing with superior sensitivity and selectivity. Upon target analyte binding, the nanoparticle dimers are brought to closer proximity, resulting in larger scattering cross section that can be readily observed with dark-field microscopy. This allows detection and imaging of target analytes with much improved spatiotemporal resolution even for single molecule binding. Herein, we present an integrative approach using nanoplasmon ruler coupled with dark-field imaging for real-time mapping cytokine secretion profiles from a single immune cell. The nanoplasmon ruler probes leverage on target-specific conformation change of synthetic DNA aptamers guided by a biomimetic riboswitch design, which enables homogeneous detection of human Interleukin-6 (IL-6) and interferons-gamma (IFN-γ) with high sensitivity. Besides, intercellular communication processes in a tumour microenvironment model system with the presence of CAR-T cells, B-ALL cells, and macrophages were also observed and imaged under the nanoplasmon ruler platform.

3.2 Experiments

Characterization methods

Morphological studies on nanoplasmon ruler were performed using scanning electron

microscopy (SEM, Hitachi TM 3000). HR4000 High-resolution User-configured Spectrometer (Ocean Optics) was used to analyze the scattering spectrum of sensing spots on the chip. Particles size distribution and charge carrier were identified through Dynamic Light Scattering (DLS, Zetasizer Nano ZS90, Malvern).

Coarse-grained discrete molecular dynamics (DMD) simulations.

In DMD simulations, temperatures were in the reduced unit of kcal/(mol•k_B). We used eight replica simulations with following temperatures: 0.200, 0.225, 0.250, 0.270, 0.300, 0.333, 0.367, and 0.400. We employed the weighted histogram analysis method[214] to compute the distribution of end-to-end distances at T=0.300.

Electromagnetic-field simulation on AuNP dimer.

We predict the electric field distribution near the surface of AuNP dimer upon interaction with the external electric filed. The AuNP size is 30nm. We defined far-field domain surround the AuNP dimer with a radium of half the wavelength of incident light and a perfectly match layer of the same thickness, in which the scattering light decays exponentially. The incident light was set parallel to the dimer axis. The hot pot between the dimer gap showed the strong plasmon resonance. We also investigated the scattering intensity when incident light was perpendicular to the dimer axis, the weak electric filed distributed around the AuNP dimer proved the negligible contributions of the light to the scattering intensity change. The influence of gap distance on the scattering cross section change was also evaluated.

LSPR immunoassay

1) Characterization of gold nanoparticles

The gold nanoparticles (AuNPs) used in this study were purchased from nanoComposix in aqueous sodium citrate (2mM) buffer with an average diameter of 30 nm(0.05mg/mL). The Citrate coating on the AuNRs resulted in a negatively charged surface with a zeta potential of -48±0.5 mV (Zetasizer Nano ZS90, Malvern). The scattering spectrum of the AuNPs in solution was obtained using a spectrophotometer. The resonance peak wavelength of the AuNP lays around 520 nm (**Figure 3.1**).

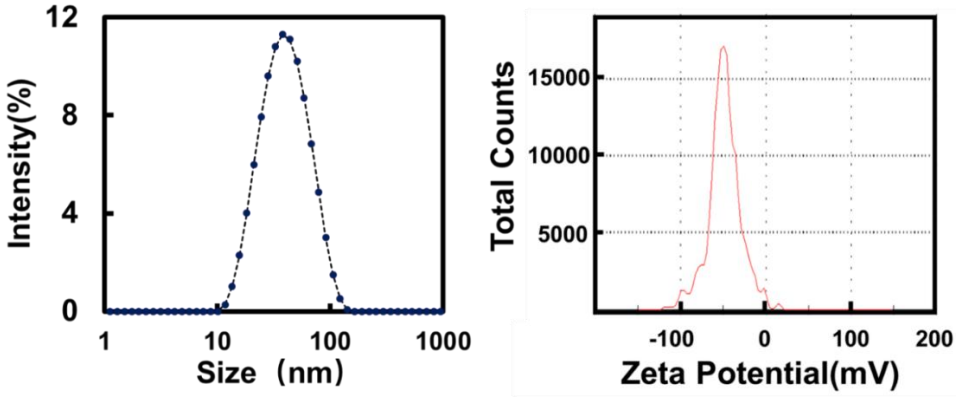

Figure 3.1 DLS analysis for gold nanoparticles. (a) Size distribution. (b) Zeta potential.

2) PDMS Microfluidic Channel fabrication

A microfluidic flow-patterning mask layer mold was fabricated on a silicon substrate by deep reactive-ion etching (DRIE). The mold contains five parallel microfluidic channels (400 μm (W) x 2.5 cm (L) x 50 μm) for the AuNPs patterning and function. To make the microfluidic mask layer, a liquid PDMS (Sylgard-184, Dow Corning) pre-polymer fully mixed with cross-linker at the weight ratio of 10:1was exposed to vacuum

to completely remove air bubbles. After degassing, the mixture was poured onto the silicon mask mold wafer and degassed using a vacuum pump, and then we placed the Petri dish containing the wafer in an over for 6h at 70°C. The cured PDMS mask layer can be easily peeled off from the mold wafer and cut into several pieces. Then, a hole puncher with 1mm diameter was used to create inlets and outlets of the channel.

3) Self-assembled Nanoplasmon ruler

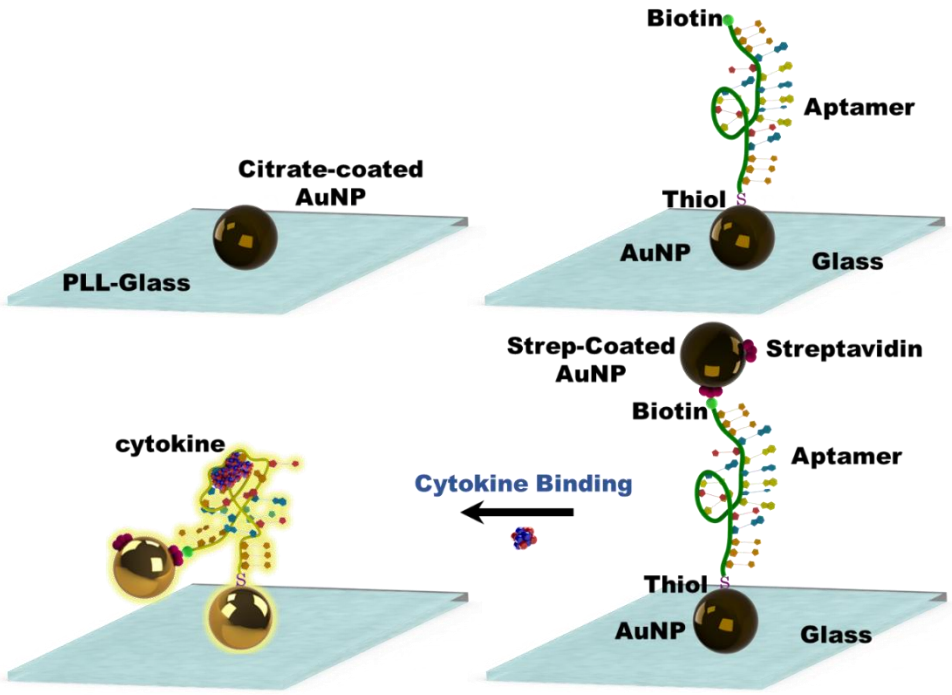

Figure 3.2 Schematics of nanoplasmon ruler assembling process.

Nanoplasmon ruler were self-assembled in the microfluidic device on a glass chip (**Figure 3.2**). A high-precision syringe pump (Masterflex, 100 to 240 VAC) was used to control the flow rate.

AuNPs Patterning. Glass slides were first washed using DI water and dried in the oven. They were put into the Piranha solution (H_2SO_4:H_2O_2 = 3:1 v/v) for 10 min, followed

by the complete wash by DI water. Finally, the glass was rinsed in DI water and kept in an ultrasonic bath for 15 min. To pattern the AuNPs, the prepared PDMS mask was bonded onto the glass substrate. Then we loaded poly-L-lysine hydrobromide solution (PLL, Sigma) (0.1mg/mL) into each channel at a flow rate of 1.5 μL/min for 6 min follow by 0.2 μL/min for 2 min. Then we sealed the inlets and outlets with a cover glass to prevent liquid evaporation from the channel and incubated the chip for at least 4hrs. After that, each channel was washed with DI water at a flow rate of 1.5 μL/min for 4 min, and then AuNPs stock solution (0.05mg/mL) was loaded into each channel at a flow rate of 1.5 μL/min for 6 min follow by 0.2 μL/min for 2 min. The chip was incubated overnight.

Aptamer Preparation. DNA aptamer targeting human IL-6 was conjugated with a biotin group on one end and a thiol group on the other end. To prepare the stock solution, the lyophilized aptamer was suspended in IDTE buffer at a stock concentration of 100 μM and stored at −20 °C. Prior to use, the aptamer should be reduced first because that thiol-modified oligos are in the oxidized form. 10uL of 10mM TCEP solution was added in aptamer stock solution with the same volume and let it incubate for a couple of hours at room temperature. Then folding buffer (30 mM HEPES, pH 7.5; 100 mM potassium acetate) was used to dilute the aptamer to 10-100x working concentration. To fold the aptamer, the solution was heated to 90-95 °C for 5 min and then cooled to room temperature (~15min). Then the folded aptamer was diluted to working concentration using working buffer (1mM $MgCl_2$ in TE buffer).

Monomeric Aptamer-Au Nanoparticle Preparation. After constructing the AuNP microarray patterns on the glass substrate, we functionalized them with the aptamer within the microfluidic flow-patterning channels constructed above. To remove the unbound AuNPs, 20μL of PBS was used to thoroughly wash the channel at 2 μL/min. Then, the reduced aptamer at working concentration (1nm) was loaded into each channel at a flow rate of 1.5 μL/min for 6min follow by 0.2 μL/min for 2 min and incubated overnight.

Streptavidin-functioned AuNPs Preparation. Adsorption of streptavidin (SA) on AuNPs was achieved by adding 100 μL of SA solution (100 nM in 1x PBS buffer) to 100 μL of AuNPs solutions (0.5 nM), and the mixture was kept on ice for 1 h. The solution was centrifuged for 5 min at 12,000 rpm. The unreacted excess of SA was removed by discarding the supernatants and redispersing the particle in 100 μL of DI water.

Preparation of nanoplasmon ruler. After washing the channel with 20 μL of DI water to remove the excess unbound aptamer at a flow rate of 2μL/min for 4 min, streptavidin functioned AuNPs solution was loaded into each channel at a flow rate of 1.5 μL/min for 6 min followed by 0.2 μL/min for 2 min to bind with aptamer functioned AuNPs to form the nanoplasmon rulers and incubated overnight.

Biosensor optimization. To optimize the sensor behavior, we demonstrated the correlation between the aptamer to AuNP ratio during the assembling process and the final nanoplasmon ruler density in the sensing area. Five different ratios between the

aptamer and AuNP (1:1, 2:1, 5:1, 10:1. 50:1) were evaluated and the nanoplasmon ruler densities were determined through SEM images.

4) Real-time dynamic cytokine binding curve

The dark-field microscope measurements were performed on a Nikon Eclipse Ni-U system. After the fabrication of nanoplasmon ruler, the prepared immunoassay chip was mounted the on a motorized X-Y stage (ProScanIII, Prior Scientific, Rockland, MA), which allowed automated image scanning. The back of the chip was attached with a dark-field condenser (NA=1.45, Nikon) via the lens oil. 10x objective lens (Nikon) was used in the system. Before doing the measurement, PDMS layer used for plasmon ruler function was removed immediately and replaced with another sample-loading PDMS microfluidic channels perpendicularly. Before doing them optical measurement, 30 μL of cell medium were loaded into the on-chip flow channel at the speed of 1.5 μL/min to stabilize the initial light intensity of sensing spots. After signal stabilization, cytokine sample was loaded into the channel using a syringe pump at 0.5 μL/min for 30 min. The automated imaging was performed by an ultrasensitive electron multiplying CCD (EMCCD, Photometrics) and recorded by NIS-Element BR analysis every 10s.

Real-time intensity change in the sensing area was obtained by MATLAB code which computed the intensity difference between the analysed image with the first image, and got the relative intensity change:

$$I_{x,y} = \frac{I_{i(x,y)} - \mathrm{I}_{1(x,y)}}{\mathrm{I}_{1(x,y)}}$$

Where I_1 means the average intensity in the analysed area for the first dark-field image.

In order to characterize the uncertainty and limit of detection of our LSPR microarray system, we performed a control experiment measuring the variance of the background signal with nanoplasmon ruler microarrays loaded with cell medium solution. The average system uncertainty determined by the minimum distinguishable signal equivalent to a confidence factor was set to be 3 times the standard deviation of the background noise (σ). The detection limits of the target cytokines were thus obtained from $3\sigma/k_{slope}$, where k_{slope} is the slope of calibration curves using linear fitting.

5) Single-cell cytokine mapping using nanoplasmon ruler.

Cell culture. Jurkat human T cells (CRL-2901TM, ATCC) were cultured in RPMI-1640 combining with 10% fetal bovine serum (ATCC® 30-2020™) and 200mcg/mL G428. Human B lymphoblast (ATCC® CRL-5969™)) were cultured in RPMI-1640 combining with 10% FBS. Cells were incubated at 37◦C with 5% CO_2 in a Cell Culture Incubator (Thermo Scientific). In order to maintain a suitable cell culture concentration which is between at 1 $x10^5$ to $1x10^6$ cells/mL, the culture medium was replaced two to three times per week. Cells with required concentration were collected through centrifugation at 125xg for 5 min with subsequent resuspension in the fresh culture medium.

Cell stimulation and single-cell secretion patterning image. 1 mL Jurkat T cell was suspended in the cell culture medium at the concentration of $1x10^6$ cells/mL. A mixture of PMA (100 ng/mL, Sigma – Aldrich) and Ionomycin (1,000 ng/mL, Sigma – Aldrich)

was added into the T cell solution to stimulate the cytokines secretion. The stimulated T cells were diluted into $1x10^5$ cells/mL and loaded into PDMS channels and randomly settled on the prepared nanoplasmon ruler surface. The dark-field images were captured with the exposure time of 10s for 30 mins.

6) Cytokine mapping in CAR-T cell therapy using nanoplasmon ruler.

Cell lines preparation. Human acute lymphoblastic leukemia cells (NALM-6, CRL-3273™) were cultured in RPMI-1640 medium (Invitrogen) supplemented with 10% FBS, 1% penicillin/streptomycin in a 37 °C with 5% CO_2 incubator. NALM-6 cells were collected at $1x10^5$ cells/ml and labeled by green fluorescent protein (GFP) for cell tracing.

Human THP-1 cells (TIB202™, ATCC) were grown in RPMI-1640 medium, supplemented with 10% FBS, and 1% penicillin/streptomycin in a 37 °C with 5% CO_2 incubator. Macrophages were fluorescently labeled with Hoechst solution (Thermo Scientific, 62249) following the manufacturer's instructions. Briefly, macrophages were incubated with serum-free RPMI-1640 containing 1u/mL of Hoechst solution for 25 min at 37 °C, followed by a rinse with RPMI-1640 medium three times. The labelled macrophages were then collected and resuspended at $1x10^5$ cells/ml for further use.

Human CD19 CAR T-cells (PM-CAR-1003-1M, ProMab) were expanded with 1 ml of T-cell media supplemented with 200U IL-2 and 25 ul Anti-CD3 and CD8 activator in ImmunoCult™-XF T Cell Expansion Medium (Stemcell Technologies, catalog # 10981), as well as red fluorescence protein (RFP) for fluorescent cell tracing. Following

expansion, CAR-T cells were then collected and resuspended at $1x10^5$ cells/ml for further use.

Anisotropic analysis for cytokine secretion

Isotropy reforms to uniformly cytokine secretion in all orientations of the cell, which means that the concentration distributions tend to be consistent all around the cell. Otherwise, anisotropy was presented when cytokine secretion is restricted to specific regions. The anisotropic property in different directions (every 30º) was determined by anisotropy ratio – the ratio of the standard derivation of cytokine concentration in different regions (every 30º) to the average cytokine concentration in whole analyzed area (120 um x120 um around the cell).

Mathematical model for diffusion coefficient analysis

To analyse the kinetic of cytokine secretion during the imaging process, a mathematic model was built based on a previously reported cyto/chemokine diffusion model in intercellular signalling process[215].

Single suspended solitary cells can be regarded as a spherical surface source for cytokine secretion. The time dependent mass transport from a single cell can be described by the equation:

$$\frac{\partial C}{\partial t} = D\frac{1}{r^2}\frac{\partial}{\partial r}[r^2\frac{\partial C}{\partial r}] \qquad \textbf{[1]}$$

where C is the cytokine concentration, r is the distance, and D is the diffusion coefficient. There were three boundary conditions: (1) Secretion rate (F_0) was constant

at the cell surface; (2) there are no cytokines far away from the cell; (3) the cytokine concentration was 0 surrounding the cell. The conditions can be stated as:

$$At\ r = \rho,\ \ F_0 = -D\frac{\partial C}{\partial r}$$

$$At\ r \to \infty, \qquad C \to 0$$

$$At\ t = 0, \qquad C = 0$$

where ρ was the cell radius. One thing to note that cell secretion could be asymmetric and shows "plumes" shape around the cell. Then the diffusion analysis was restricted in that specific direction using the same model. The final diffusion equation could be expressed as:

$$C(r,t)=\frac{F_0\rho}{2Dr}\sqrt{\frac{4Dt}{\pi}}\{e^{\frac{-(r-\rho)^2}{4Dt}} - e^{\frac{-(r+\rho)^2}{4Dt}} - \frac{|r-\rho|}{\sqrt{\frac{4Dt}{\pi}}} \times erfc\left(\frac{|r-\rho|}{\sqrt{4Dt}}\right) + \frac{|r+\rho|}{\sqrt{\frac{4Dt}{\pi}}} erfc\left(\frac{|r+\rho|}{\sqrt{4Dt}}\right)\} \quad \textbf{[2]}$$

The diffusion coefficient was obtained through a MATLAB program which was used to get the analytical solution by assigning the experiment values to the parameters (t,C, ρ,r,F_0).

3.3 Results and discussion

3.3.1 Experiment mechanisms and nanoplasmon ruler assembling

Plasmon coupling is a reaction that occurs when two or more plasmonic particles approach each other to a distance below approximately one diameter's length. Upon the occurrence of plasmon coupling, the resonance of individual particles starts to hybridize, and their resonance spectrum peak wavelength will either blueshift or redshift,

depending on how surface charge density distributes over coupled particles. At single particles' resonance wavelength, the surface charge densities of close particles can either be out of phase or in phase, which causes repulsion or attraction and in turn leads to increase (blueshift) or decrease (redshift) of hybridized mode energy. The magnitude of the shift, which can be the measurement of plasmon coupling, is dependent on the interparticle gap as well as particles geometry and plasmonic resonances supported by individual particles.

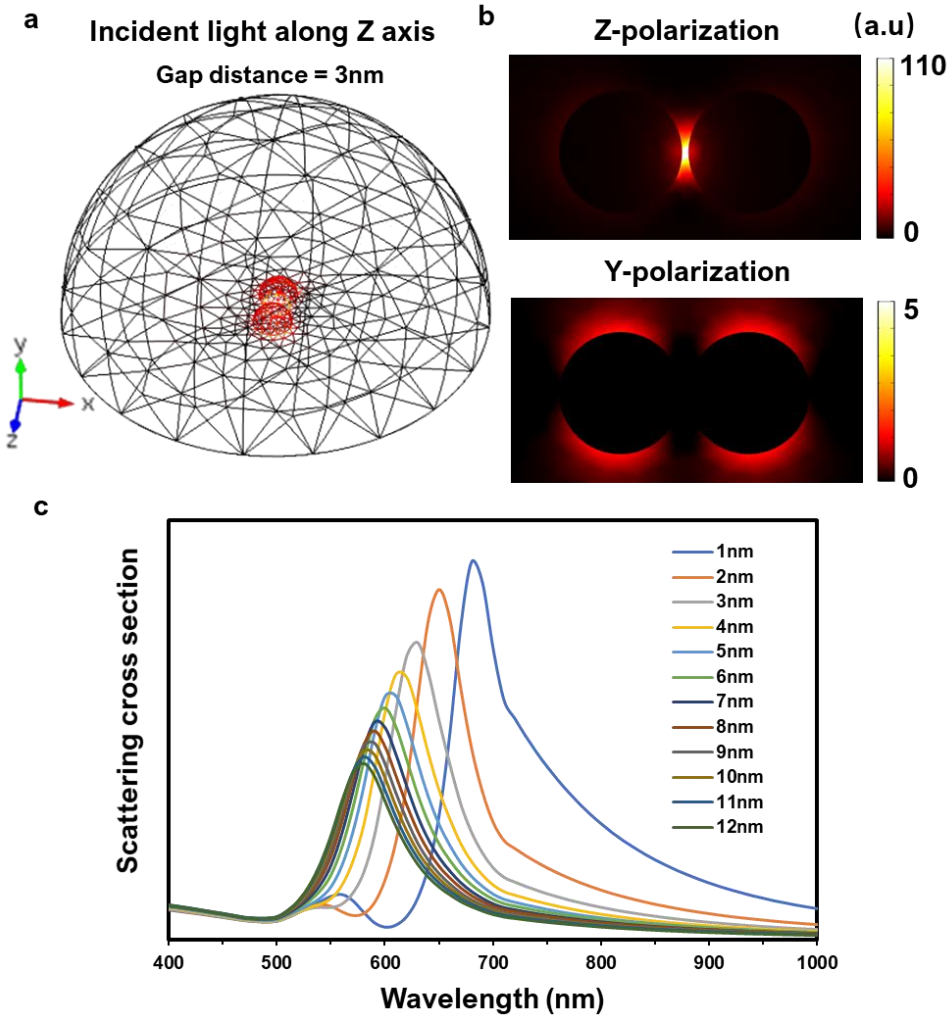

Figure 3.3 Electromagnetic-filed simulation results. (a). Electromagnetic-filed simulation on scattering response of AuNP dimer upon interaction with polarized

incident light which is parallel to the dimer axis. The red (black) color represents high (low) electric intensity. (b). Comparation the influence of incident light polarization on the scattering response of AuNP dimer. (c). Predicted scattering spectrum changes with the gap distance change.

To achieve optimal optical sensing performance, we used COMSOL to simulate the electric field distribution near the surface of AuNP dimer after interaction with the external electric filed. The incident light was set parallel to the dimer axis (**Figure 3.3a**). The area between the dimer gap showed the strong plasmon resonance. However, when incident light direction was perpendicular to the dimer axis, the weak electric filed distributed around the AuNP dimer demonstrated the negligible contributions to the scattering intensity change (**Figure 3.3b**). We also simulated the influence of gap distance on the scattering cross section change. A reduced interparticle separation resulted in a red shift of the resonance spectrum and electric field enhancement. This distance-dependent plasmon coupling was even more sensitive to small gap distance (<10nm) (**Figure 3.3c**). These results indicate that if the designed nanoplasmon ruler has a large gap distance change upon binding to the target antigen, the induced strong plasmon coupling and significant scattering spectrum change can lead to an ultrasensitive cytokine detection.

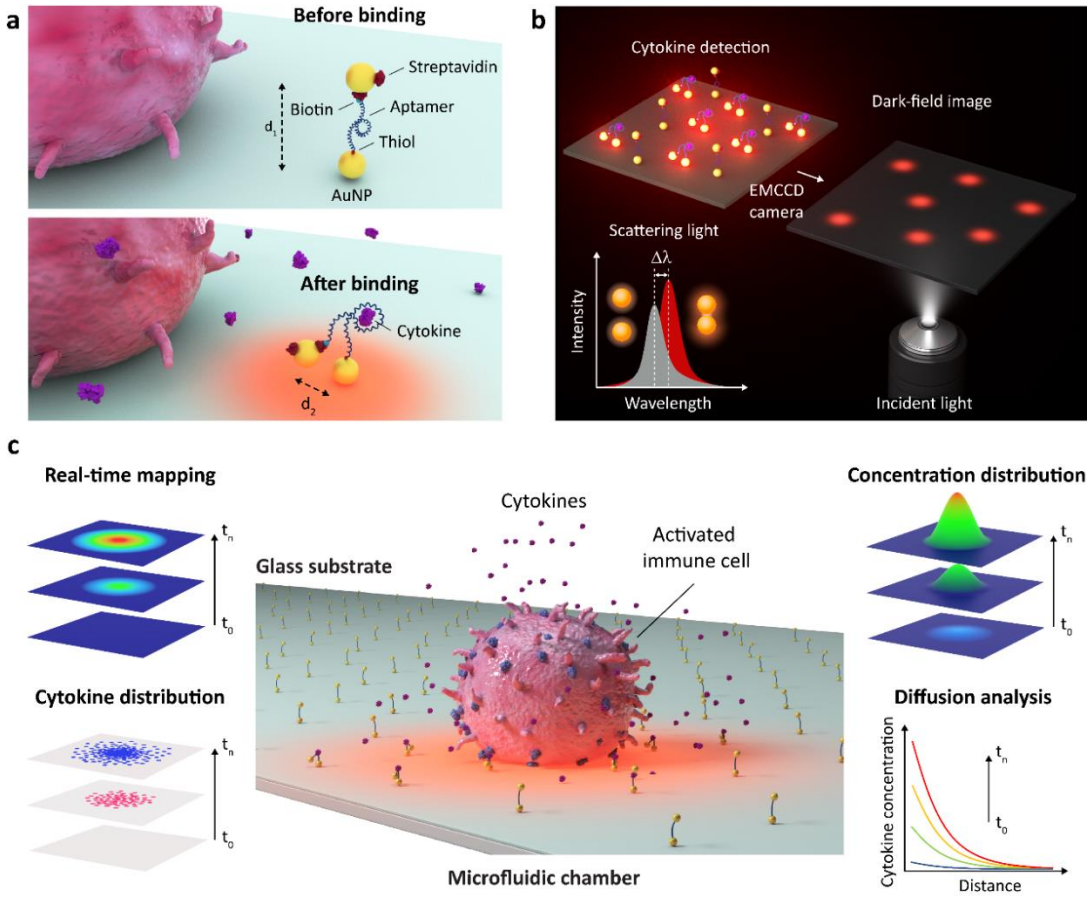

Figure 3.4 The principle of the nanoplasmon ruler method for single cell secretion mapping. (a)The nanoplasmon ruler was assembled on the glass side using a one-step microfluidic patterning technique. Upon cytokine binding, the NP dimers are brought to closer distance. (b) The strong plasmonic coupling leads to a redshift and scattering intensity change of the spectrum which can be detected by the optical spectrometer. Rea-time intensity change can be imaged via the EMCCD coupled dark-field microscopy. (c) Cytokine secretion from a single cell can detected in real-time and located though customized MATLAB code. The cytokine distribution, cytokine concentration distribution, and cytokine diffusion data can be further achieved though real-time imaging data analysis.

Biopolymers like DNA, RNA, and proteins usually undergo conformational changes in their folded form in response to the change of external factors such as temperature, pH, ionic strength, or ligand binding[216]. Hence, a conformational changeable single-strand

DNA combining with a dimer of metal nanoparticles can form a nanoplasmon ruler structure. Due to the interparticle distance- dependent property of plasmon resonance, real-time single-cell secretion imaging can be achieved by the nanoplasmon ruler biosensor. After stimulation, immune cells will secrete specific cytokines. The binding of target cytokines to the aptamer will change the distance between the paired AuNPs and results in a closer proximity, yielding a significantly enhanced plasmonic coupling and generating a red-shift light scattering spectrum dependent on the interparticle distance (**Figure 3.4a**). Local scattering intensity change due to the cytokine binding was captured by a EMCCD camera in real-time and analysed via a customised MATLAB code (**Figure 3.4b**). The cytokine concentration distribution around the cell can be directly determined from the local intensity change. Isotropy or anisotropy secretion behaviours of the cell can be determined though the secretion profiles. Besides, the diffusion coefficient can also be compared and analysed to further reveal the heterogeneity of the cells (**Figure 3.4c**). Since the plasmonic coupling induced by the aptamer-cytokine binding process is specific, unspecific binding of the cytokine on the glass substrate will not influence the light response, which guaranteed the detection sensitivity and selectivity.

3.3.2 Design an DNA aptamer with a robust conformational switch

The desired nanoplasmon ruler structure consists of three key components: A substrate citrate coated gold nanoparticle (AuNP, 30nm), a modified DNA aptamer targeting specific cytokine, and a coupling AuNP. In which, aptamer is the critical part that

directly determines the sensor performance. Effective target detection by the plasmon ruler requires a large end-to-end distance change of the aptamer upon target binding. Since a given DNA/RNA aptamer does not necessarily undergo conformational changes before and after target binding, we propose a sequence redesign approach to engineer robust conformational switching by mimicking riboswitches in gene regulation[217]. Specifically, a competing short sequence complementary to a part of the aptamer sequence with existing base-pairs is introduced to either the 5' or 3' regions, so that the formation of newly engineered base-pairs in an alternative conformational state ("off" state) disputes the original structure compatible for target binding ("on" state). If the stability of the redesigned alternative state (ΔGoff) is stronger than the stability of the "on" state of the aptamer alone (ΔGon) but weaker than that of the aptamer-target complex (ΔGon+ΔGbinding), the resigned aptamer adopts the "off" state in the absence of target but switches to the "on" state in the presence of target.

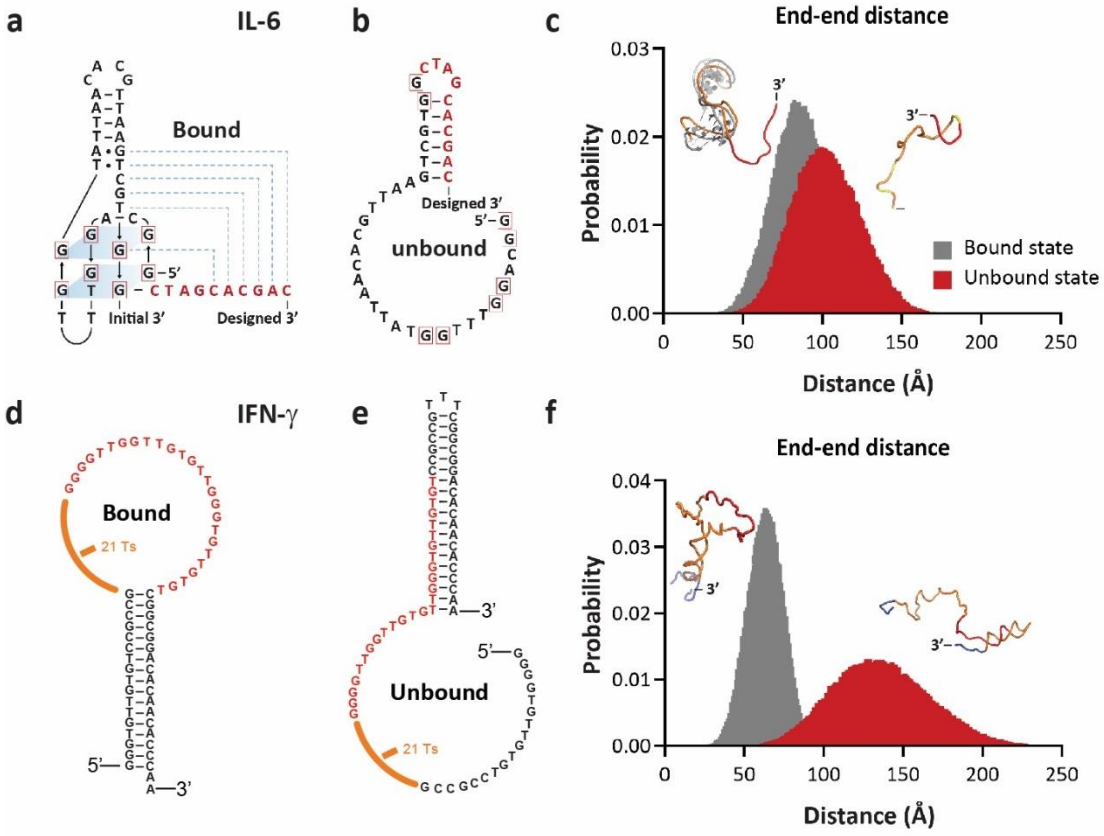

Figure 3.5 Switchable aptamer sequence design upon IL-6 and IFN-γ aptamer.

(a) Estimated structure of bound state of the redesign IL-6 aptamer sequence. Added nucleotides are marked in red. Possible secondary structures are marked in blue dotted lines. (b) Estimated secondary structure of unbound state of the redesign sequence. Added nucleotides are in red, and GQ required guanines are marked in red square box. (c)End-to-end distance probability distribution at simulation Temperature of 0.3. Superposition of DNA aptamer structure (All-Atom model in grey) against DMD prediction resulting from bound and unbound structure (ribbon backbone in orange) are shown near the distribution curves. Backbone of added nucleotides are marked in red. (d) Estimated structure of bound state and (e) unbound state of the redesign IFN-γ aptamer sequence. Binding sequences are shown in red, added nucleotides are marked in black, and 21 T bases are show in orange segment. (f) End-to-end distance probability distribution for IFN-γ aptamer at simulation Temperature of 0.3. Superposition of DNA aptamer structures are shown nearby the distribution curves.

Here, we based our design on a 32-nt DNA aptamer identified by SELEX to target IL-6 with a binding constant Kd ~ 0.16 nM (ΔGbinding ~ -12.4 kcal/mol)[218]. Crystallography study of the aptamer-IL6 complex showed that the aptamer in the bound formed a G-quartet between 5' and 3' and a short hairpin in the middle **(Figure 3.5a)**. Using Mfold[219] and the tabulated stabilities of G-quartets with different topologies[220], the stability of the "on" state alone ΔGon was estimated to be ~ -3.4 kcal/mol. We introduced a 10-nt sequence to the 3' end that competes with a guanine forming the G-quartet **(Figure 3.5b)**, and the Mfold server estimated a corresponding free energy of the "off" state of ~ -7.9 kcal/mol. We also performed coarse-grained discrete molecular dynamics (DMD) simulations to estimate the distributions of end-to-end distances for both "on" and "off" states. The "on" state with G-quartet had the average end-to-end distance of ~ 8.5 nm, while the "off" state forming the designed hairpin **(Figure 3.5c)** had the average end-to-end distance of ~10 nm. Hence, we predicted a distance change of ~ 1.5 nm upon IL-6 binding. We used the simplified three-bead nucleotide model in DMD simulations to study aptamer structures, where three beads corresponding to groups of phosphate, sugar and base were used to represent each nucleotide**(Figure 3.5c inner)**. Different from continuous potential functions utilized in conventional molecular dynamics (MD) simulations, DMD employs step-functions to model inter-atomic interaction potentials. Instead of solving Newton's equations in MD simulations, DMD solves the ballistic equations for atoms which participate in 'collisions' with inter-atomic distances at potential steps and thus change velocities under the restraints of conservation laws of energy, momentum and

angular momentum, leading to fewer calculations and access to longer time scales. To increase conformational sampling, replica exchange method was used to efficiently overcome energy barriers between conformational states[221]. In replica exchange method, several simulations are running in parallel under different temperatures, and temperatures periodic exchange between adjacently replicas according to the Metropolis criteria to ensure the sampling of a generalized canonical ensemble. IFN-aptamer was redesigned from a reported 26-nt sequence. We introduced a 38-nt sequence which involves in a 21-nt T spacer to the 5' end and 28-nt sequence to the 3' end (**Figure 3.5d,e**). The redesigned aptamer prefers the "off" state before binding but switches to the "on" state in the presence of the target molecule. The corresponding free energy changes from -25.48 kcal/mol to -34.56 kcal/mol after target binding. The end-end distance change was predicted to be ~6.4nm (from 12.3nm to 6.3nm) (**Figure 3.5f**).

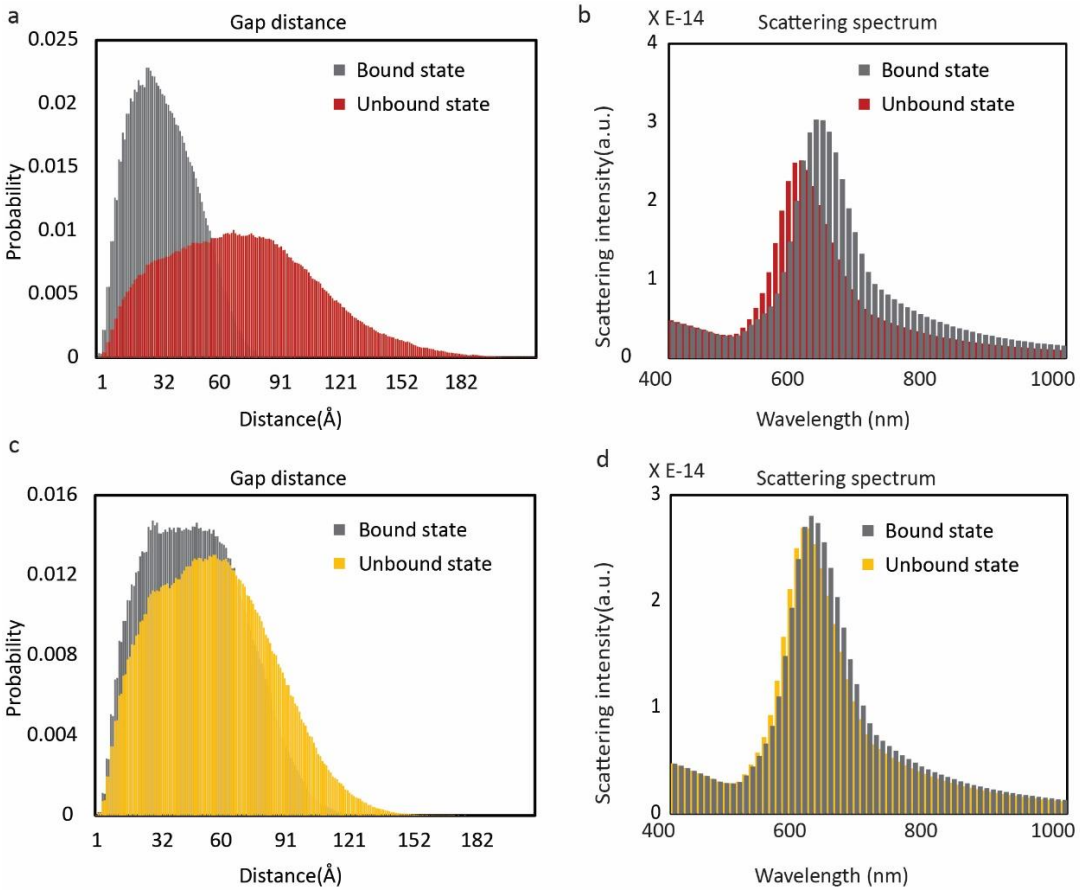

Figure 3.6 Gap distance distribution between AuNP dimer conjugated with IL-6. (a) and IFN-γ aptamer (**c**).COMSOL simulation of scattering spectrum of IL-6 (b) and IFN-γ nanoplasmon ruler (d) before and after binding of the target.

We also predicted the gap distance distribution between AuNP dimer conjugated with designed aptamer after considering the steric hindrance during the assembly process. The average gap distance changes upon IL-6 binding and IFN-γ binding are ~2nm and 4nm, respectively (**Figure 3.6a,c**). COMSOL simulation of the scattering spectra from nanoplasmon rulers before and after cytokine binding also showed a great change of intensity and peak location (**Figure 3.6b, 3d)**. The strong and uniform plasmon coupling signal gives rise to a homogeneous signal output and provides a wash-free condition in biomolecular detections.

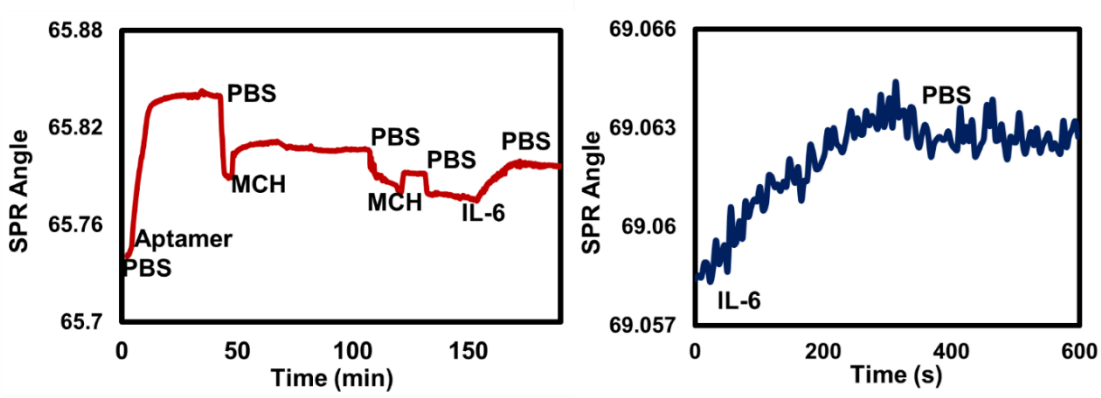

Figure 3.7 SPR validation for the IL-6 aptamer. MCH is 6-Mercapto-1-hexanol which was used to block the surface to avoid the unspecific binding. The aptamer concentration is 1 uM and Human IL-6 concentration is10 nM.

The cytokine capture performance of redesigned aptamers was first investigated by surface plasmon resonance (SPR) method. The IL-6 aptamer was immobilized the aptamer on an Au film chip with the surface bock of 6-Mercapto -1-hexanol (MCH). After stabilizing the baseline, 10nM human IL-6 was injected into the flow cell at a flow rate of 30 μL/min for 5min and then PBS buffer was injected to wash the unbound target molecules on the chip surface for 5min at the same rate (**Figure 3.7**). The good binding curve was showed as the IL-6 binding on the aptamer.

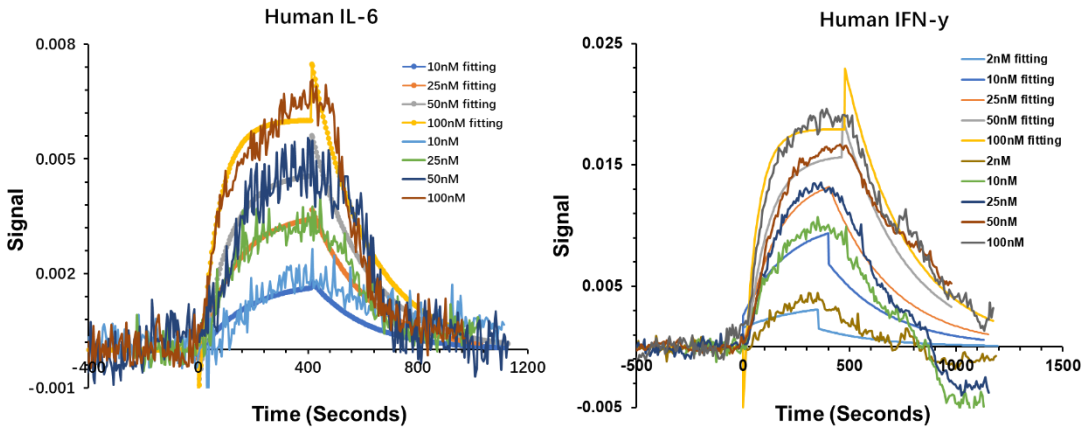

Figure 3.8 Kinetics of IL-6 and IFN-γ binding. Each of binding curve would be fitted into a related mathematic model to do the quantitative characterization.

We detected different concentrations of spiked IL-6 and IFN-γ solution in real-time using SPR to analyze the binding kinetics. Kinetic parameters were obtained by fitting the sensor grams with BIAEVAL 4 software. It was shown that the association rate constant (K_{on}) for IL-6 aptamer is $9.98x10^4$ $M^{-1}S^{-1}$ and for IFN- γ aptamer is $1.32 x10^5$ $M^{-1}S^{-1}$. The dissociation rate constant (K_{off}) for IL-6 aptamer is $4.91x10^{-3}$/s and for IFN-γ aptamer is $2.41x10^{-3}$/s. The overall equilibrium dissociation constant (K_D) for IL-6 aptamer and IFN- γ aptamer is 49.2 nM and 25.9 nM, respectively (**Figure 3.8**). The SPR results showed that the redesigned aptamers worked well in target detection.

Nanoplasmon ruler assembling and real-time cytokine detection. To assemble the nanoplasmon ruler, the aptamer was modified a thiol group on one end and a biotin group on the other end, so that one end can bind to one AuNP through Au-S group and another end can bind to a streptavidin functioned AuNP to for a nanodimer structure. Besides, a 10-T spacer was functioned on both ends to relieve steric hindrance effect. The desired structures were assembled layer by layer using PDMS microfluidic

channels. The key parameters governing the assembly process such as stoichiometric ratio of aptamer to AuNP. Incubation conditions were carefully examined to get the highest yield of plasmon ruler structure. The synthesized nanostructures on the glass were imaged under dark-field microscopy (Nikon, Eclipse Ni-U) and high-resolution scanning electron microscopy (SEM, Hitachi TM 3000) **(Figure 3.9)**.

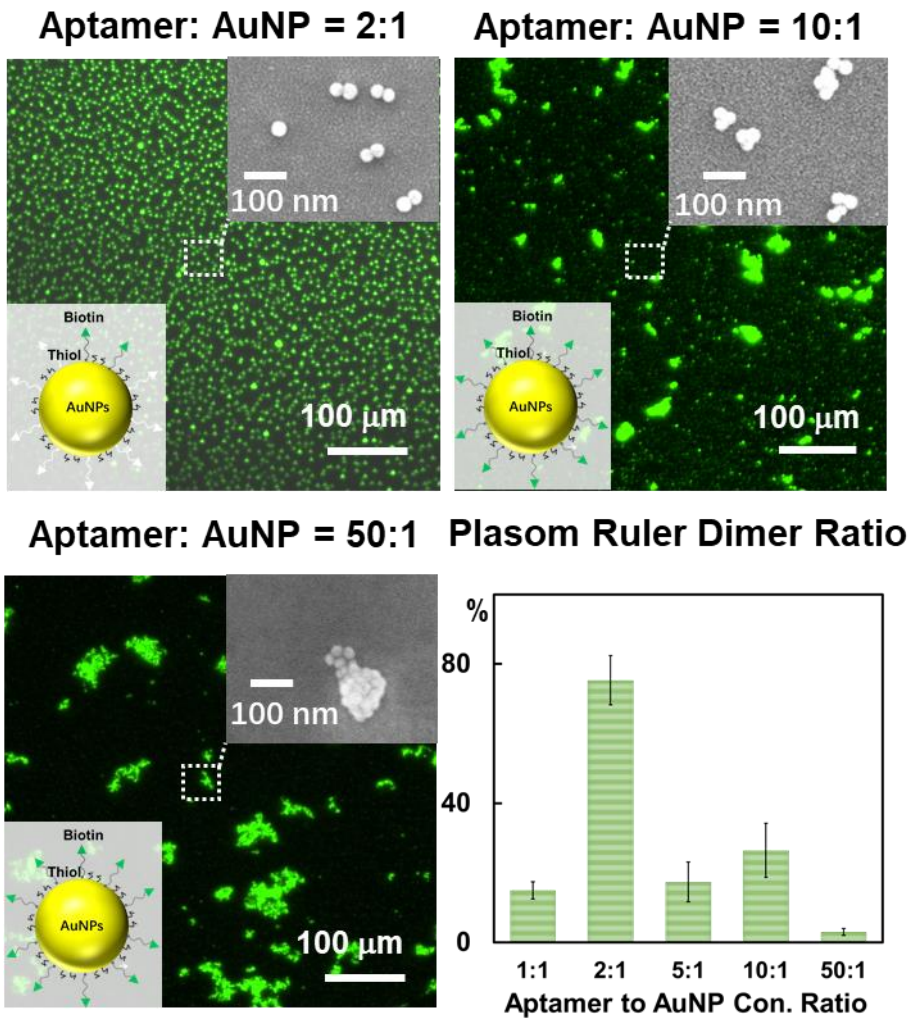

Figure 3.9 The effects of stoichiometric ratio of aptamer to AuNP on the formation of nanoplasmon ruler. The large panels show the synthesized nanostructures under dark-field and the inserted panels are zoomed-in images under SEM.

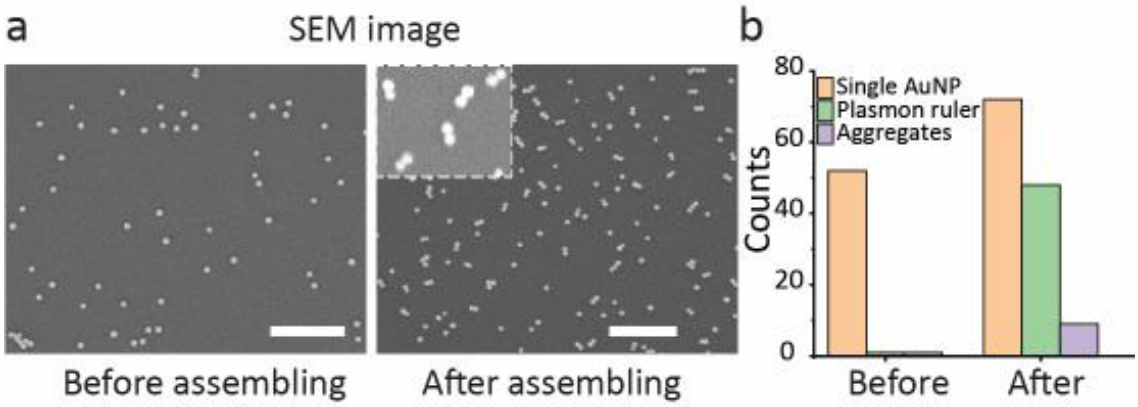

Figure 3.10 Nanoplasmon ruler sensor characterization. (a) SEM image of nanoplasmon ruler assembling process. Zoom in picture showed the plasmon ruler structure. The scale bar is in 1 μM size. (b) Comparison the distribution of the different structures on the sensor chip before and after assembling.

It showed that higher aptamer-AuNP ratio led to the formation of trimer, pentamer and even the aggregation of AuNPs due to the large number of biotin surface groups available for the binding of streptavidin-functioned AuNPs. These clusters or aggregation structures yielding a broad scattering spectrum would compromise the sensitivity for single-cell measurement. While aptamer-AuNPs ratio at around 2:1 yielded highest ratio (>70%) of well-dispersed nanoplasmon ruler structures **(Figure 3.10**Figure 3.10 Nanoplasmon ruler sensor characterization.**)**. Since the plasmonic coupling induced by the aptamer-cytokine binding process is specific, unspecific binding of the cytokine on the glass substrate will not influence the light response, which guaranteed the detection sensitivity and selectivity.

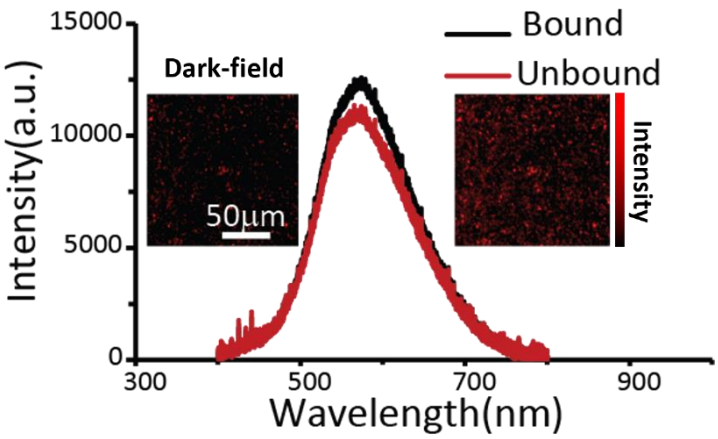

Figure 3.11 Scattering spectrums of sensor surfaces before and after analyte binding. Dark-field images of nanoplasmon ruler sensor chip before any after cytokine detection under the 10x objective lens are shown near each curve.

The scattering spectrum of the nanoplasmon ruler on the sensor chip was characterized via high-resolution optical spectrometer (Ocea optics, HR4000). Binding with the analyte led to the scattering intensity increase and the red shift of the scattering spectrum on the sensor surface, resulting in a brighter analysis area under a dark field image (**Figure 3.11**).

3.3.3 Real-time IL-6 and IFN-γ detection and mapping using nanoplasmon ruler

Proinflammatory cytokines such as IL-6 and IFN-γ as multifunctional factors have thought to mediate the intercellular communication in inflammatory and immune response processes[152]. An elevated IL-6 level has been widely found in many inflammatory-based or immune-mediated diseases such as multiple myeloma, Crohn's disease, rheumatoid arthritis, and chronic psoriasis[222]. Rapid and accurate detection of cytokines in clinical condition offers a great value in disease monitoring and diagnosis.

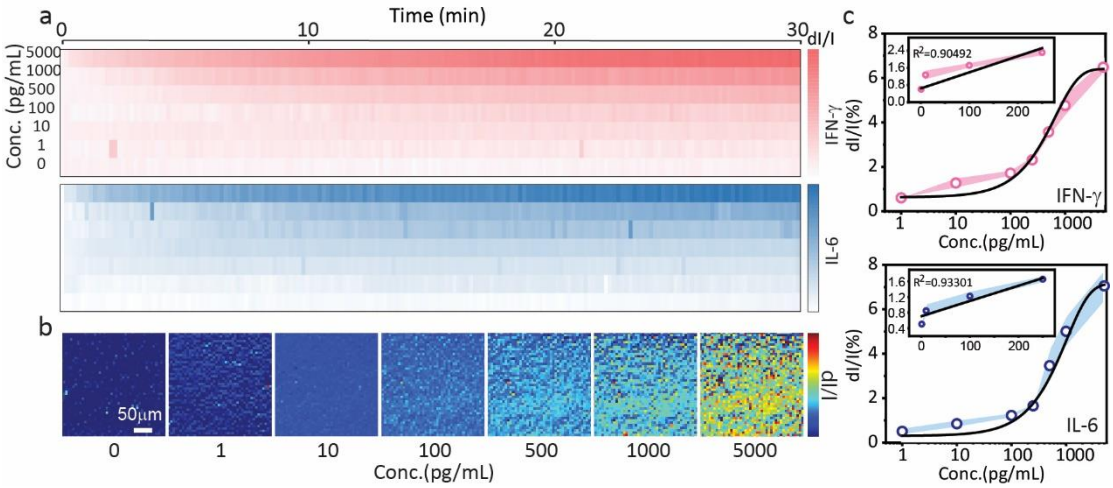

Figure 3.12 Real-time spiked cytokine solution mapping. (a) real-time intensity changes on the sensor surface for the IL-6/IFN-γ detection at different concentrations. (b) IL-6 detection mapping at different concentrations after 30 min detection. (c) Calibration curve IL-6 and IFN-γ detection.

The performance for nanoplasmon ruler biosensor was validated by measuring the limit of detection (LoD) at different analyte concentrations under the dark-field microscope. Different concretions (0, 1, 10, 100, 500, 1000, and 5000pg/mL) of human IL-6/IFN-γ solution dissolved in cell culture medium were loaded into the microfluidic channels of nanoplasmon ruler device. The time-course signal variation from the sensor spot with 250 x 250 pixels (400 x 400 μm^2) was observed under the dark-field microscope by an ultrasensitive electron multiplying CCD (EMCCD, Photometrics) with a frame acquisition rate at every 10s. To minimize system error, 5x5 pixels (8 x 8 μm^2) were set as a detection unit due to the tiny image vibration. The relative intensity changes ($(I-I_0)/I$) of every detection unit was analysed via a customized MATLAB code in real-time (**Figure 3.12a**). The signal platform showed that the analyte-binding event reached an equilibrium within 30min after introducing the cytokine into the sensor chip,

demonstrating a rapid binding kinetics and shorter incubation time as compared to traditional sandwich immunoassay. The intensity change mapping of sensor surface after measurement were shown in a form of heatmap (**Figure 3.12b**). **Figure 3.12c** showed the calibration curves of human IL-6 and IFN-γ detection. The LoD of human IL-6 in our system is 61 pg/mL, while the L0D of IFN-γ is 79 pg/mL. These detection limits were sufficient for the system to detect the IL-6 and IFN-γ secretion from a single cell[223].

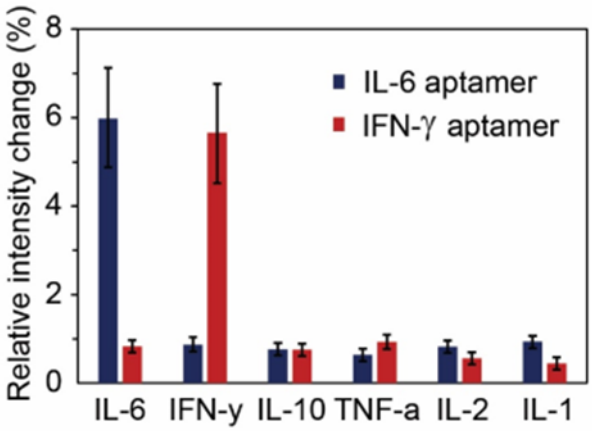

Figure 3.13 Sensor selectivity verification. Using nanoplasmon ruler assembled with human IL-6/ IFN-γ aptamer to detect human IL-6, IFN-γ, IL-10, TNF-α, IL-2, and IL-1 in 5 ng/mL.

In addition, the control groups with pure cell medium solution and nontargeted cytokines including human Tumor Necrosis Factor- Alpha (TNF-a), Interleukin 10 (IL-10), Interleukin 2 (IL-2), and Interleukin 1 (IL-1) showed negligible relative intensity change, proving the great selectivity of nanoplasmon ruler sensor to detect the specific cytokine (**Figure 3.13)**. The presented results show the great potential for application of our plasmon ruler in single-cell protein secretion detection and mapping.

3.3.4 Single-cell cytokine secretion mapping using nanoplasmon ruler

T cells play a key role in mediating adaptive immunity against multiple pathogens and tumors[224]. The release of multiple cytokines by T cells contribute to trigger the immune response and against infections[225]. In immunology, cytokines secreted by immune cells serve as the signaling molecules to adjust immune system and drive the proliferation, differentiation, and cytotoxicity activation of immune cells[153]. In clinical, cytokine secretion level is a signal reflecting the disease-specific immune response[226]. Technological advances have shown great efforts on the investigation of the relationship between cytokines and cells both in bulk and single-cell resolution. They provided valuable knowledges of the underlying mechanism for the intercellular communication and regulatory mechanism of immune system, leading to the more precise disease diagnosis and more effective clinic treatment. In addition, even though homogenous cell population shows regular and programmatic response, there are still a large degree of heterogeneity exists in single-cell level[227,228]. Due to the complexity of the intercellular communication and functional heterogeneity of individual immune cells, cytokine detection is necessary to be applied at the level of single-cell resolution.

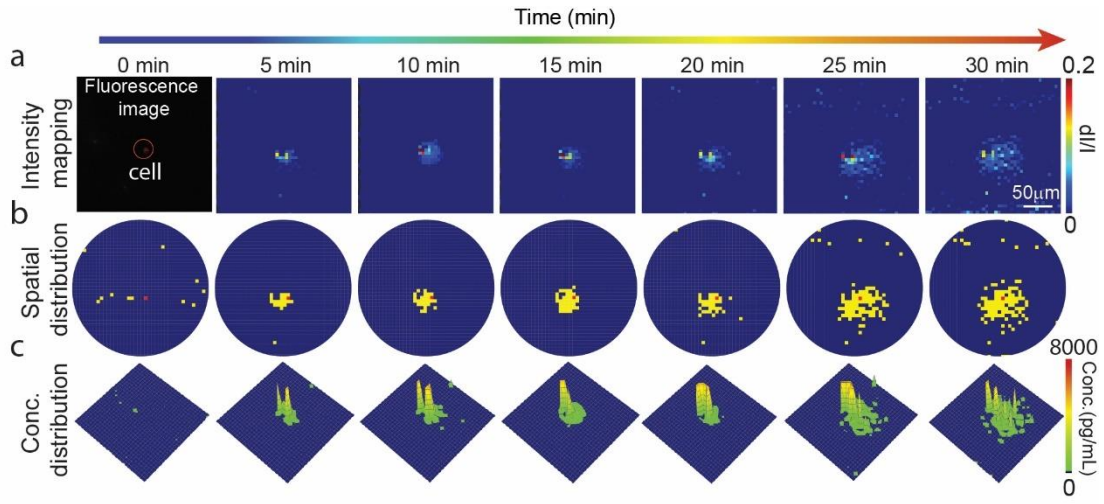

Figure 3.14 Single-cell secretion mapping. (a) Real-time imaging of the single-cell IL-6 secretion process in 30min was shown in the first row. Single T cells were random settled on the chip surface. The T cell location was determined by fluorescence image and labeled with a red circle. Secreted IL-6 will be captured by the nanoplasmon ruler on the substrate, leading to local intensity increase around the cell which can be real-time monitored by EMCCD camera. (b) By setting a threshold, the change of cytokine distribution with time was determined and shown in yellow dot. (c) Concentration distribution in the analyzed area was determine by transferring the relative intensity change to concentration vis calibration curve. The analyzed sensor area is 250μmx250 μm. Here, we employed the nanoplasmon ruler for direct visualization of the human IL-6 secretion profile from single immune T cells under external antigen stimulation to study the individual T cell behavior. We first stained purified human Jurkat T cells (CRL-2901TM, ATCC) with red CMTPX dye and stimulated them by phorbol 12-myristate 13-acetate (PMA) and ionomycin (see methods) to induce T cell receptor (TCR)-independent stimulation of immune response. PMA and ionomycin can induce elevated cytokine secretion of T cells due to the heightened AP-1 activity[229]. The activated T cells were loaded into the microchannels at a diluted population of 10^5

cells/mL and randomly settled on the prepared nanoplasmon ruler surface. The individually distributed immune cells can be located using a fluorescence microscope with the TRITC filter. The dark-field microscope with EMCCD camera was them performed to capture the dark-field images at the frame rate of every 10s for 30 mins. The binding of the target cytokines (IL-6/IFN-γ) secreted by the stimulated T cells on the nanoplasmon ruler induced a local intensity increase in the analysed region (250 μmx250 μm). The secretion process can be real-time imaged by the colormap with the fraction of relative intensity change of secretion unit (5 pixels x 5 pixels) (**Figure 3.14a**). A radiant IL-6 secretion pattern suggested a non-directional secretion mechanism form the T-cell when isolated. The cytokine binding locations were defined when the relative intensity changes of secretion units above the background noise (**Figure 3.14b**). The area concentration can be determined through the calibration curve (**Figure 3.14c)**. The time-depended secretion area change demonstrated the great spatiotemporal resolution of nanoplasmon ruler in single-cell secretion imaging.

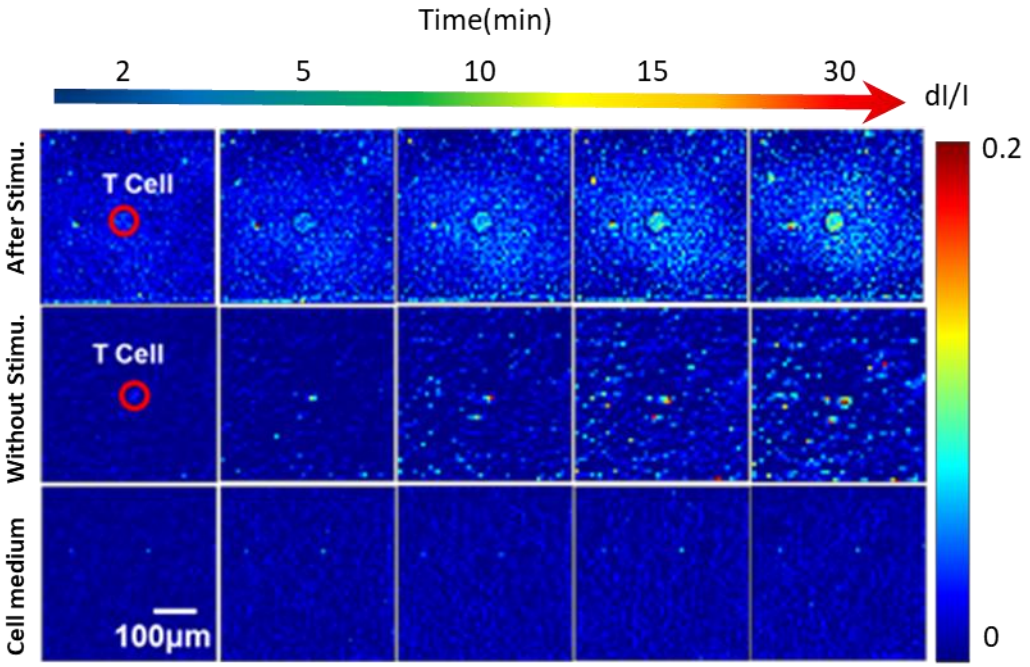

Figure 3.15 Single-cell secretion mapping under different stimulation conditions. T cell location was labelled with red circle.

Figure 3.15 shows secretion profiles of single T cells under different stimulation conditions over a region of interest at 2, 5, 10, 15, 30 min. The performance of T cells incubated with and without toxic agent was compared. After incubation with PMA and ionomycin, the image profiles showed fast local intensity change around the analytical cell. In contrast, without the stimulation of toxicant, T cell secretion was negligible. The relative intensity change around individual T cells was minimal and showed the poor secretion activity.

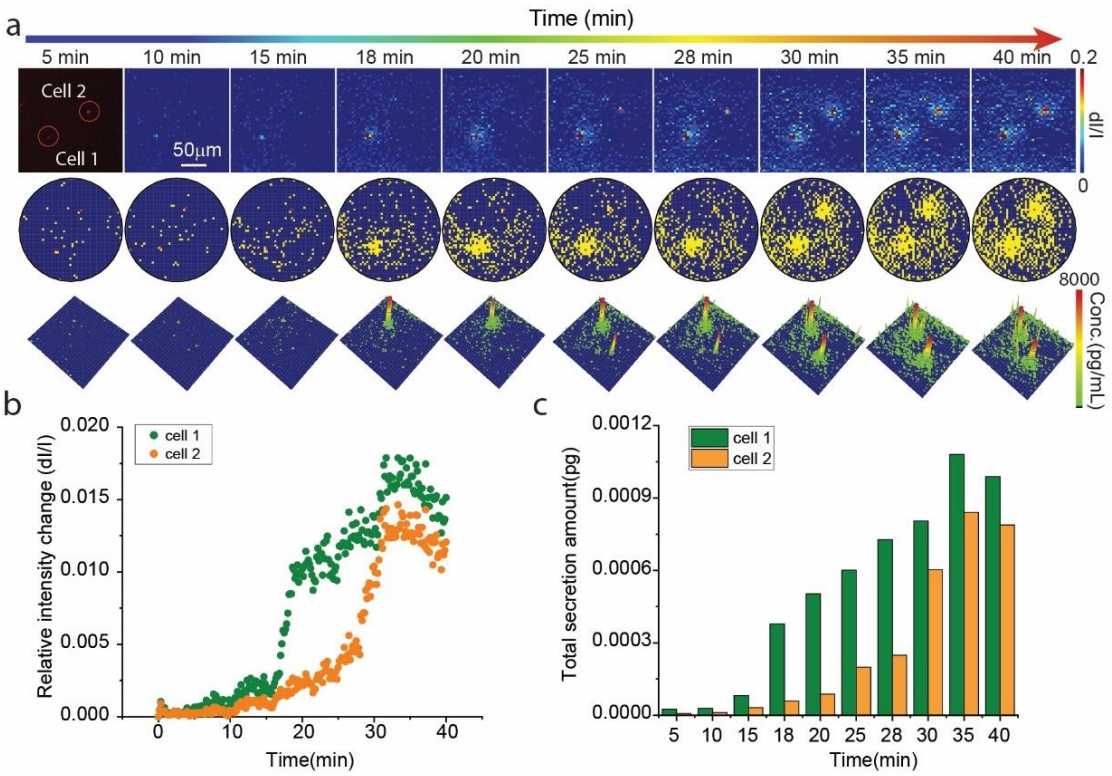

Figure 3.16 IL-6 secretion profiles from two adjacent cells. (a) Real-time image, cytokine distribution, and concentration distribution change in 40min. (b) Real-time curve for local intensity change around the cell. The dark-filed image was captured by EMCCD every 10s. (c) Change of secretion amount in 40min.

While even under the same stimulation condition, individual T cells would show different secretion patterns, indicating the heterogeneity of cytokine secretion dynamic, which has rarely been observed by previous studies. **Figure 3.16** showed IL-6 secretion profiles of two adjacent cells. One cell started to secret the IL-6 at 10min, while another one started to secret at around 18min (**Figure 3.16b**). We also calculated the change of secretion amounts in 40min, the IL-6 secretion in analysis area tended to be saturated after 30-min measurement (**Figure 3.16c**). The distinct secretion patterns and secretion amounts clearly indicate the functional heterogeneity of individual immune cells.

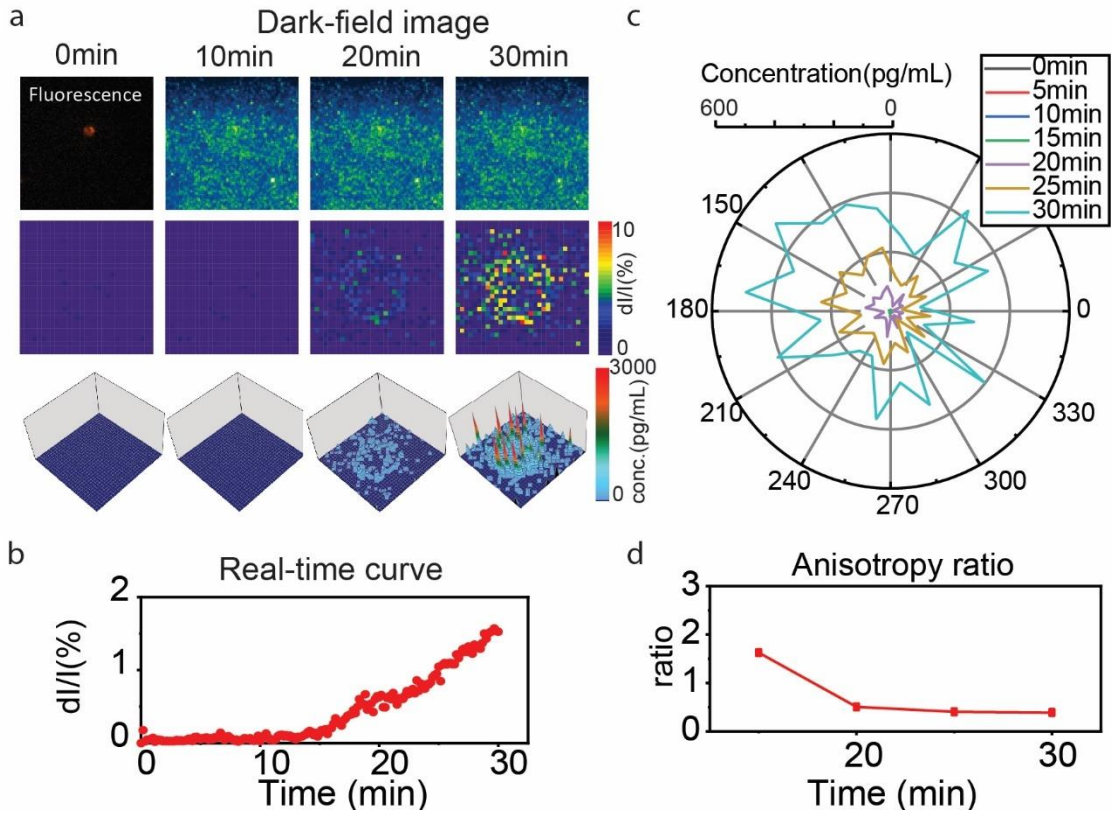

Figure 3.17 Isotropic IL-6 secretion process from single T cell. (a) Fluorescence image and dark-field images are shown in first line. The second line and third line show the secretion mapping and concentration profiles in 0 min, 10 min, 20 min, 30 min, respectively. (b) Real-time curve showing the relative intensity change around the single cell (250μmx250μm). (c) Rose diagram of concentration profiles with time in all directions for anisotropy analysis.(d) Change of anisotropy ratio with time.

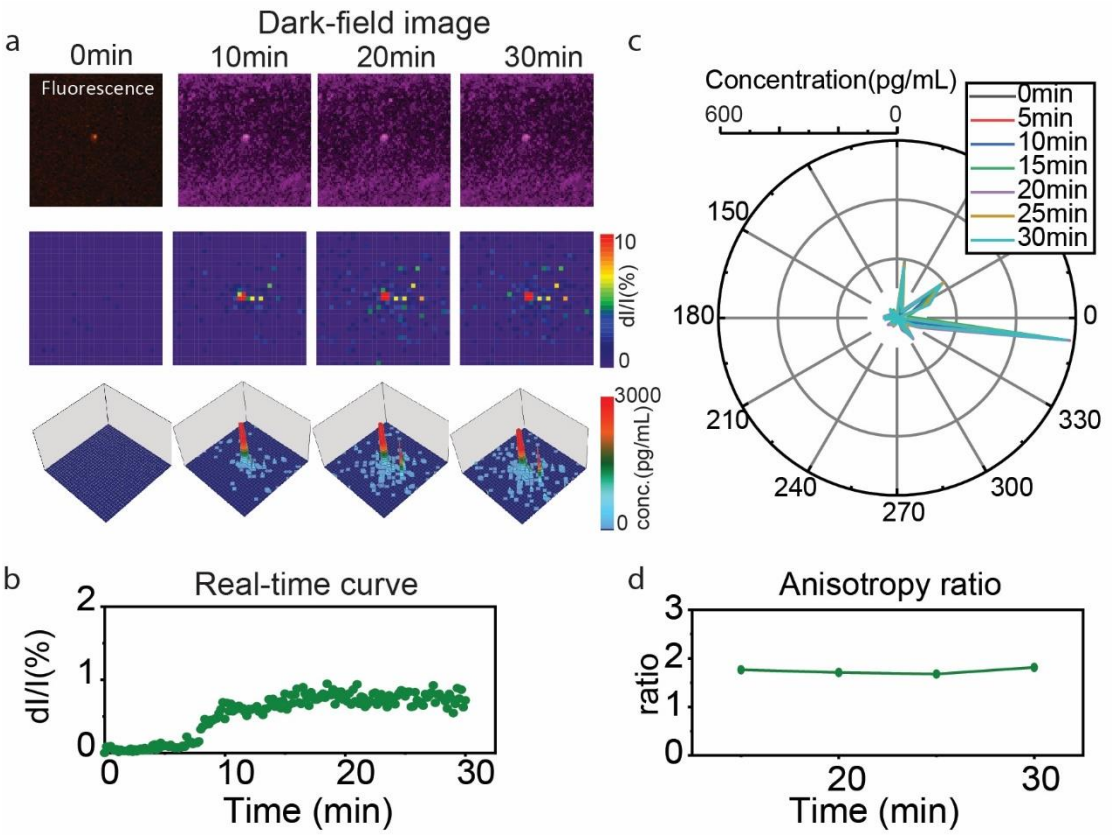

Figure 3.18 Anisotropic IL-6 secretion of single cell secretion. (a) Fluorescence image and dark-field images are shown in first line. The second line and third line show the secretion mapping and concentration profiles in 0 min, 10 min, 20 min, 30 min, respectively. (b) Real-time curve showing the relative intensity change around the single cell (250μmx250μm). (c) Rose diagram of concentration profiles with time in all directions for anisotropy analysis.(d) Change of anisotropy ratio with time.

In addition to the heterogenous amounts and rates of cytokine secretion, we observed that the heterogeneity in cytokine secretion direction. Isotropic secretion tends to be uniform in all directions, meaning that the average concentration does not vary in any direction. Whereas the secretion of cytokines is anisotropic when the mean concentration of cytokines is different in direction. In this study, whether the cell secretion is isotropic or anisotropic was determined by the anisotropy index – the ratio

of the standard derivation of concentration in different directions to the average concentration of the entire analyzed area. The anisotropy ratios were evaluated using MATLAB code. As shown in **Figure 3.17** and **Figure 3.18**, the single-cell secretion can be classified into two categories based on the anisotropy ratio of cytokine concentration distributions in different directions. Cell 1 tended to secrete homogenous with anisotropy ratio was lower that 0.5 after 30min. However, cell 2 showed an anisotropy secretion behavior and only secreted IL-6 in specific directions. The anisotropy ratio was stable during the 30 min and all above 0.5. This anisotropy property may be correlated with the anisotropic presentation of ligands on cell surfaces[230].

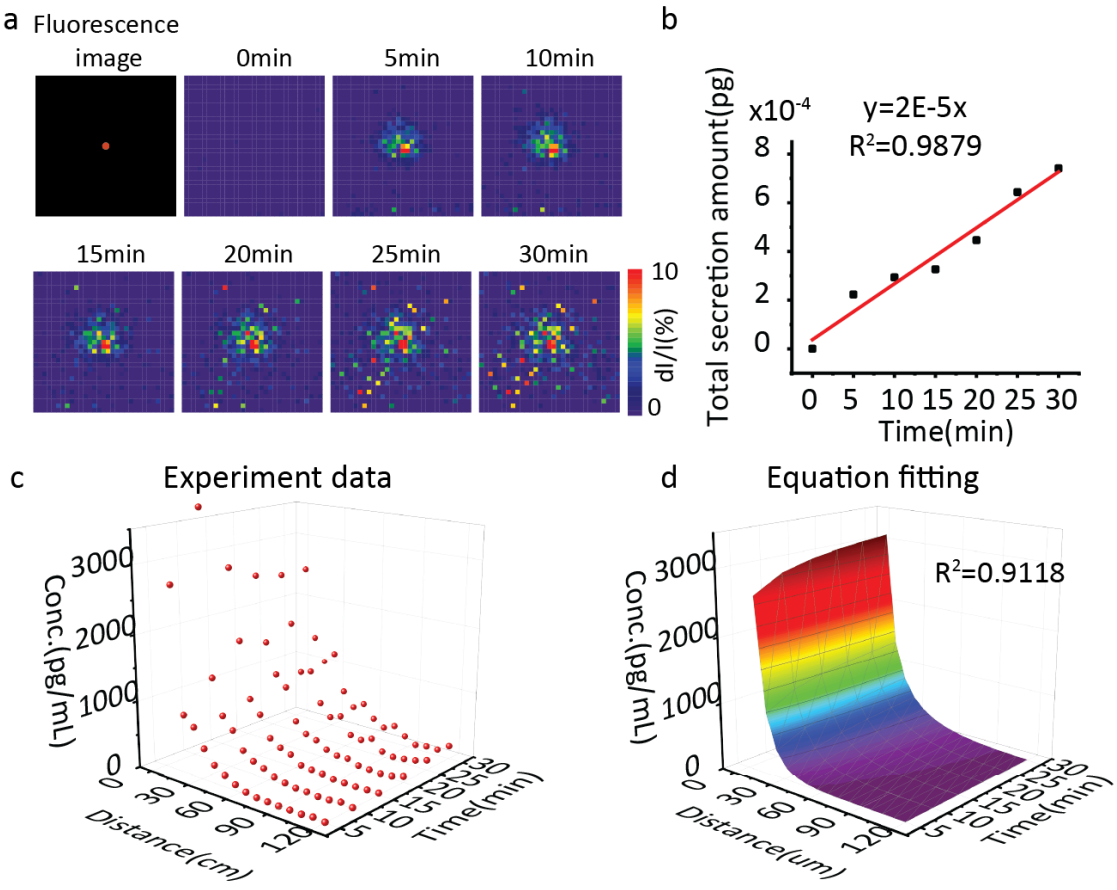

Figure 3.19 Diffusion coefficient analysis for single-cell secretion. (a) Schematic illustration of cytokine concentration gradient resulting from the secretion. (b) Real-time secretion mapping of a single-cell IL-6 secretion process. (c) Change of secretion amount in 30min. (d) Concentration distribution in specific area around the cell (150 μm x 150 μm). (e) Fitting the experiment data to the cytokine diffusion model.

We used a reported solitary cell model (**Equation 4.2**) to estimate the apparent diffusion coefficient (D) of IL-6 and IFN-γ secretion from 20 single T cells each. D was obtained through numerical approximation method performed in a MATLAB program. The secretion rate was defined as the average cytokine amount in a unit cell surface, which was calculated from the curve between the total secretion amount and time (**Figure 3.19b**). The experimental data showed a good correlation with fitting data

(R^2=0.9118) (**Figure 3.19c,d**), meaning the model was appropriate to describe the single-cell secretion process. We analyzed the heterogeneity of IL-6 and IFN-γ secretion within each 20-cell population. The average secretion rates were 11.8 molecules/s for IL-6 and 9.7 molecules/s for IFN-γ (**Figure 3.20**). The D for IFN-γ were 754.8μm^2/min which is a little bit larger than IL-6 (421.7μm^2/min). It could be due to the smaller molecular weight of IFN-γ (**Figure 3.21**). The standard derivation (SD) for each case was presented as a bar in the plots, which directly reflected the heterogeneity secretion behaviors. The mean rates of secretion for each cytokine were consistent with those evaluated from a reposted microengraving and a combination of ICS and Luminex[208].

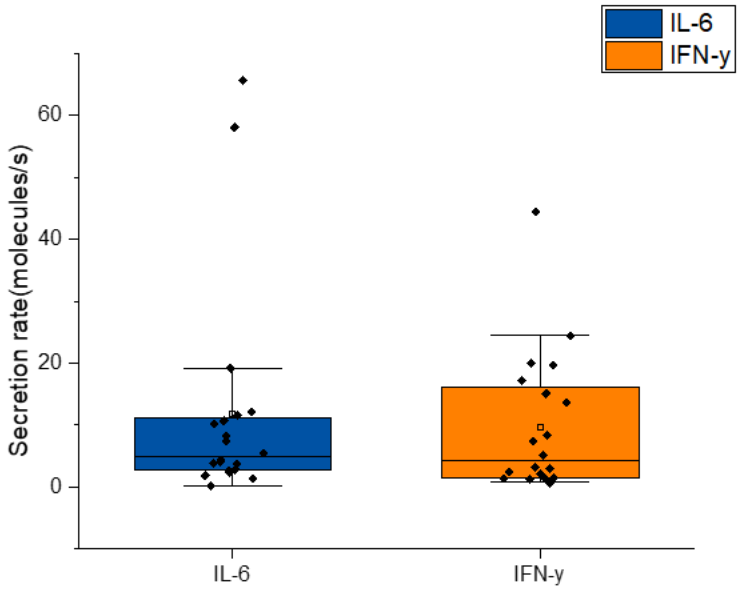

Figure 3.20 IL-6 and IFN-γ secretion rate of a 20-Jurkat T cell population.

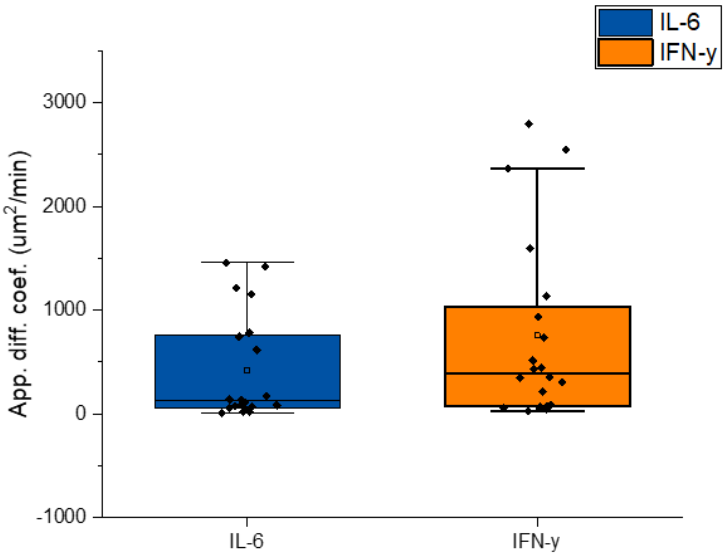

Figure 3.21 IL-6 and IFN-γ apparent diffusion coefficient of a 20-Jurkat T cell population.

3.3.5 Simultaneously mapping multiplex cells secretion profiles

Chimeric antigen receptor (CAR)-T cell immunotherapy has recently proven to be an effective treatment method for certain types of cancer such as leukemia and lymphoma[231,232]. Purified immune T cells isolated from the patient's blood were genetically modified by chimeric antigen receptors to make the T cell specific to an antigen expressed only on a certain kind of tumor. These modified T cells, usually called CAR-T cells, were cultured into several million and then reinfused into the patient leading to more effective finding and destroying of the cancer cells. However, this immune therapy is not impeccable. Side effects would come suddenly and strongly. One of the most severe side effects is called cytokine release syndrome (CRS) which may cause some life-threatening clinical manifestations such as pulmonary edema, coagulopathy, multiorgan failure, and even death[233]. It usually occurs within the first

day after CAR-T cell infusion into patients, and it is characterized by fever, hypotension, respiratory insufficiency, and dramatically increased cytokine levels, such as IL-6 and IFN-γ[234].

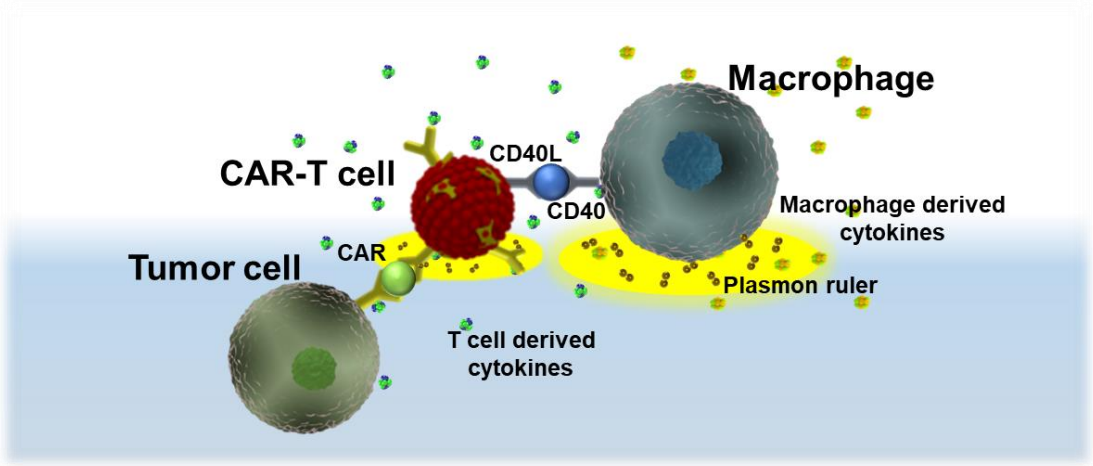

Figure 3.22 Schematics of cytokine release syndrome during CAR-T cell therapy. CD-19 CAR-T cells can directly interact with CD19-expressing tumor cells. A CD40L-CD40 interaction between CAR T cells and macrophages promotes the activation of macrophage for CRS-related cytokine secretion, which further active the CAR-T cells.

The pathophysiology of CRS has not fully understood. On-target effects caused by interaction between CAR-T cells and tumors are reported to trigger the cytokine release. In addition, many researches have revealed that macrophages are the key mediator in CAR-T related CRS(**Figure 3.22**)[235,236]. Current advances in CAR-T cell study are based mainly on animal models or clinical monitoring. Bondanza et. al demonstrated the monocyte-derived IL-1 and IL-6 are differentially required for CRS and neurotoxicity by CAR-T cells in a mouse model[237]. Sadelain et.al infused human CAR-T cell into a mouse model to prove that some cytokines such as IFN-γ and GM-CSF, were products of CAR-T cells, whereas others, such as IL-6, were produced by

endogenous mouse cells[236]. Understanding the intrinsic mechanism of CAR-T cells-induced CRS will offer better therapeutic strategy which, in turn, will leads to a safer CAR-T cell immunotherapy.

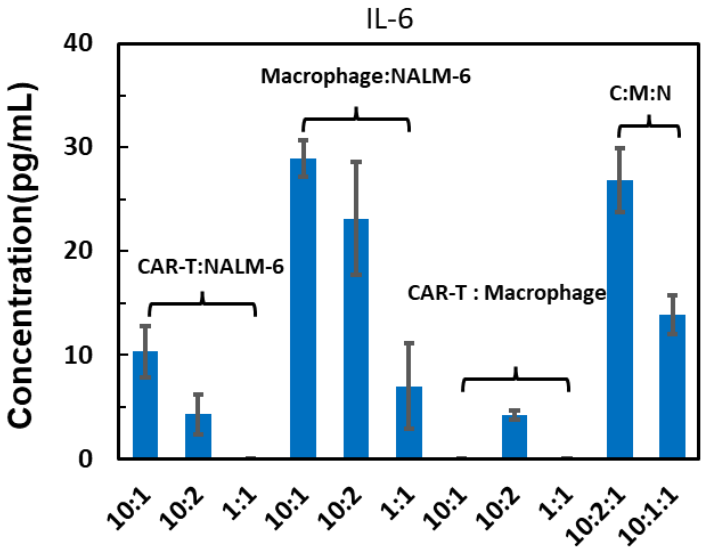

Figure 3.23 IL-6 expression after cellular co-culture quantified through ELISA method. Supernatants were collected after 10 h of co-culturing.

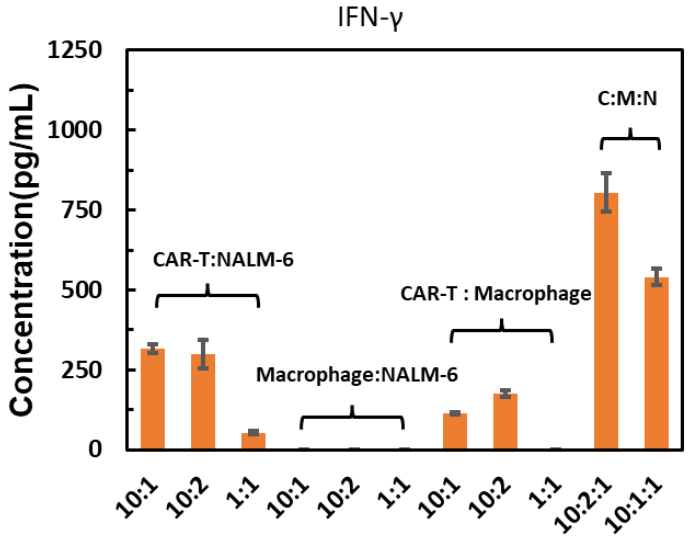

Figure 3.24 IFN-γ expression after cellular co-culture quantified through ELISA method. Supernatants were collected after 10 h of co-culturing.

To evaluate the role of different kinds of immune cell in CRS, we first evaluated the cytokine expression in CRS process in a co-colure sample by ELISA method. We investigated the cell-cell communications between CD-19 CAR-T cells, B-acute lymphoblastic leukemia cell (NALM-6), and macrophage differentiated from a monocyte lineage (THP-1). Cells were combined at different ratio (**Figure 3.23** and **Figure 3.24**). After10 h of co-culturing, much higher IFN-γ expression was observed compared with IL-6, suggesting that most IFN-γ secretion occurs at an early stage. High IL-6 levels occurred in macrophage and NALM-6 coculture sample even in the absence of CAR-T cells. However, almost no IFN-γ was detected in the absence of CAR-T cells. Cell population analysis can only provide the general information of cell behaviors. The further identification of polyfunctional response differences still requires direct visualization methods to investigate single-cell behaviors in the multiplex cells' environment.

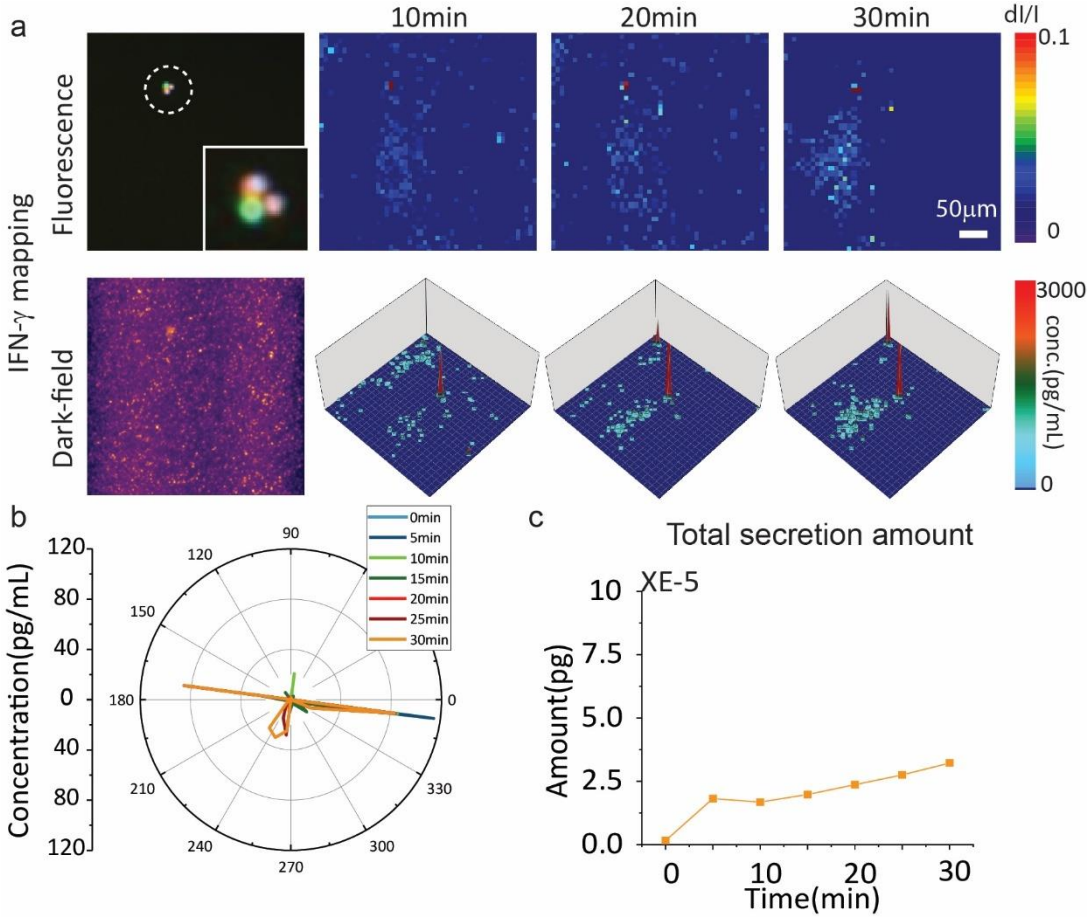

Figure 3.25 IFN-γ secretion mapping in intercellular communication among CAR-T cell, NALM-6, and macrophage. (a) IFN-γ secretion mapping. Cell locations and cell types were determined via fluorescence image. CAR-T cell is shown in red; NALM-T is shown in green; and macrophage is show in blue. Relative intensity changes and concentration profiles at 10min, 20min, and 30min are shown in color map. (b) Rose diagram of IFN-γ secretion profiles. (c) Change of secretion amount in 30min.

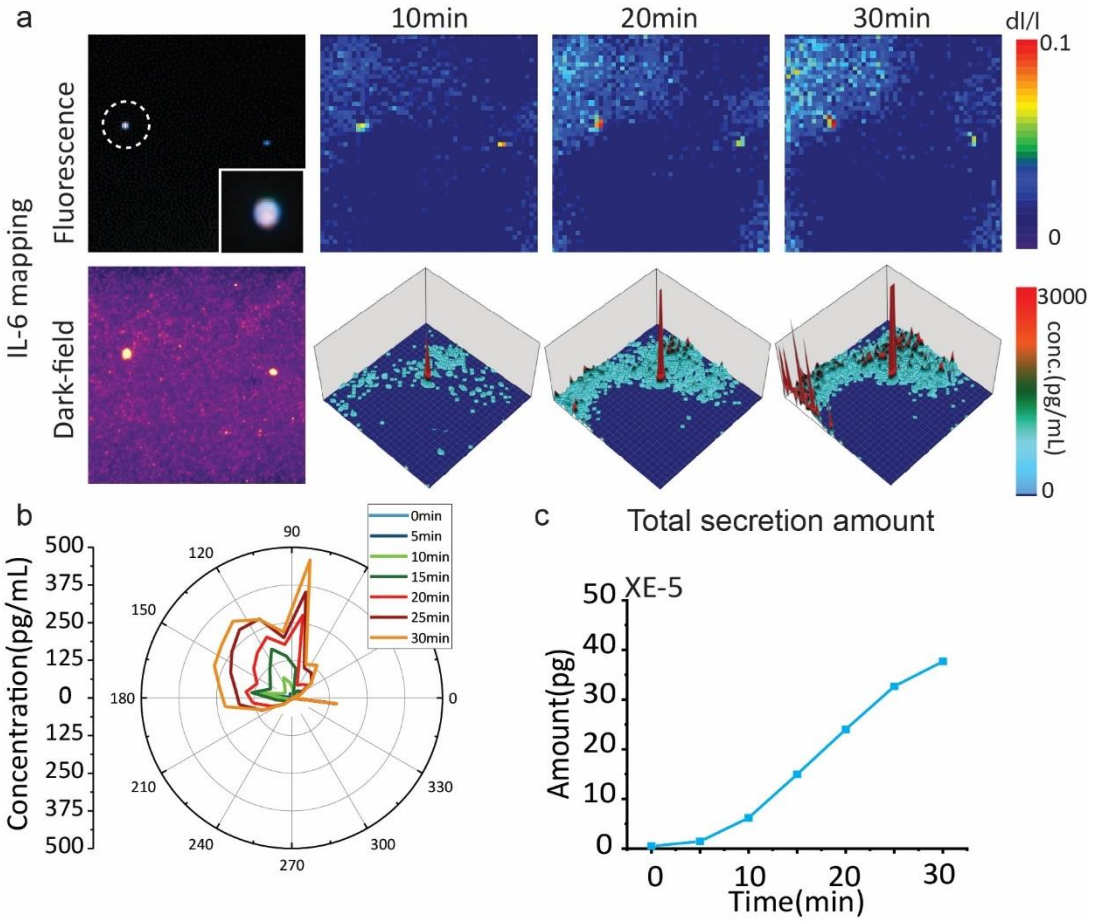

Figure 3.26 IL-6 secretion mapping in intercellular communication among CAR-T cell, NALM-6, and macrophage. (a) IL-6 secretion mapping. (b) Rose diagram of IFN-γ secretion profiles. (c) Change of secretion amount in 30min.

In our study, we used the nanoplasmon ruler biosensor patterned on glass slides to offer an on-chip way to investigate the IL-6 and IFN-γ secretion profile during the interaction between CAR-T cell, NALM-6, and macrophage. To investigate the intercellular communication, the real-time secretion profile of different types of cells were detected respectively without any agent stimulation. Purified fluorescence-labeled CAR-T cells, macrophage, and NALM-6 cells were combined at a ratio of 10:2:1 and suspended in cell culture medium. After 5h co-culture, the cell solution was loaded into the

nanoplasmon ruler chip. Cell locations and cell types were determined by fluorescence microscopy. CAR-T cells labeled with RFP showed the red fluorescence color. NALM-6 cells carrying GFP showed green color under the fluorescence microscope. Macrophages labeled by Hoechst emitted blue fluorescence color. As shown in **Figure 3.25** and **Figure 3.26**, both IL-6 and IFN-γ were expressed during the cell interaction. Three kinds of cells contacted with each other and formed a cell cluster. The real-time imaging showed the local intensity increase around the cells, indicating continuous cytokine secretion process. Most of the secretion process tended to be anisotropic.

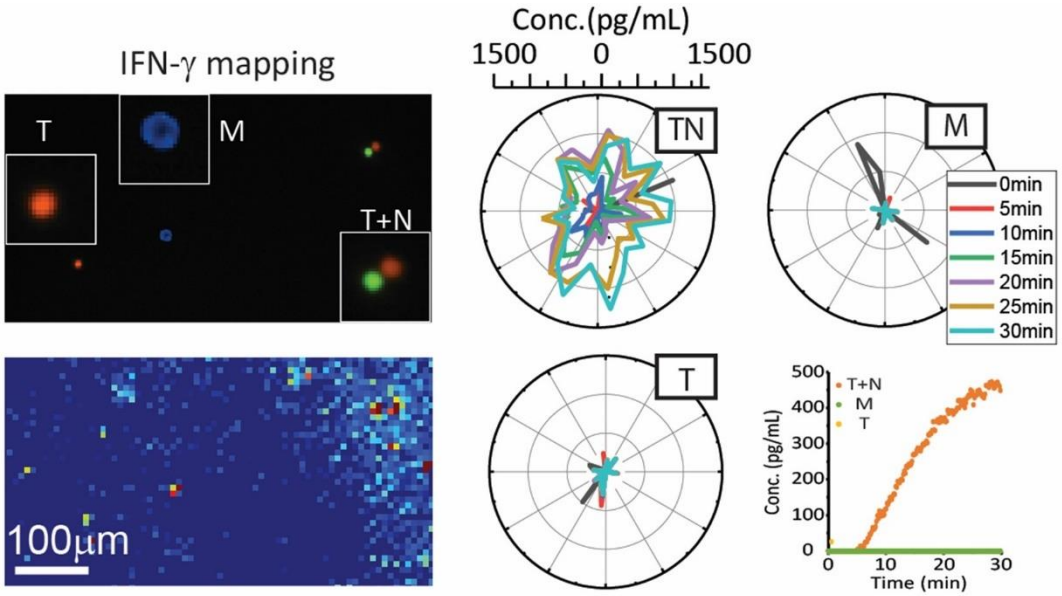

Figure 3.27 IFN-γ secretion mapping in coculture environment. The color map represents secretion mapping at 30 min. Rose diagram of secretion profiles and real-time curve are shown in right. Where T means the CAR-T cell, M means the macrophage, and N means the NALM-6.

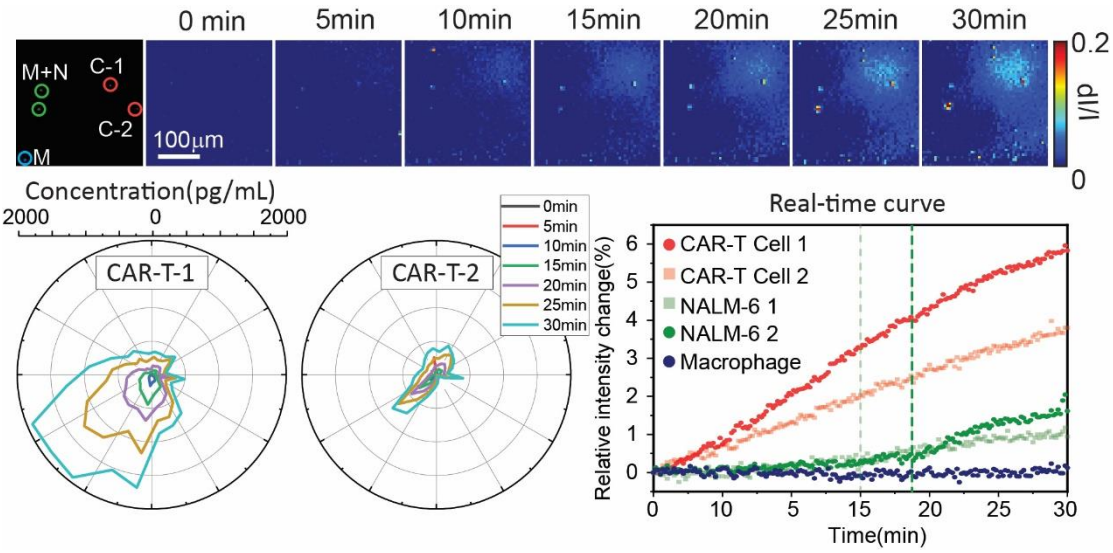

Figure 3.28 IFN-γ secretion mapping from single CAR-T cell in coculture environment.

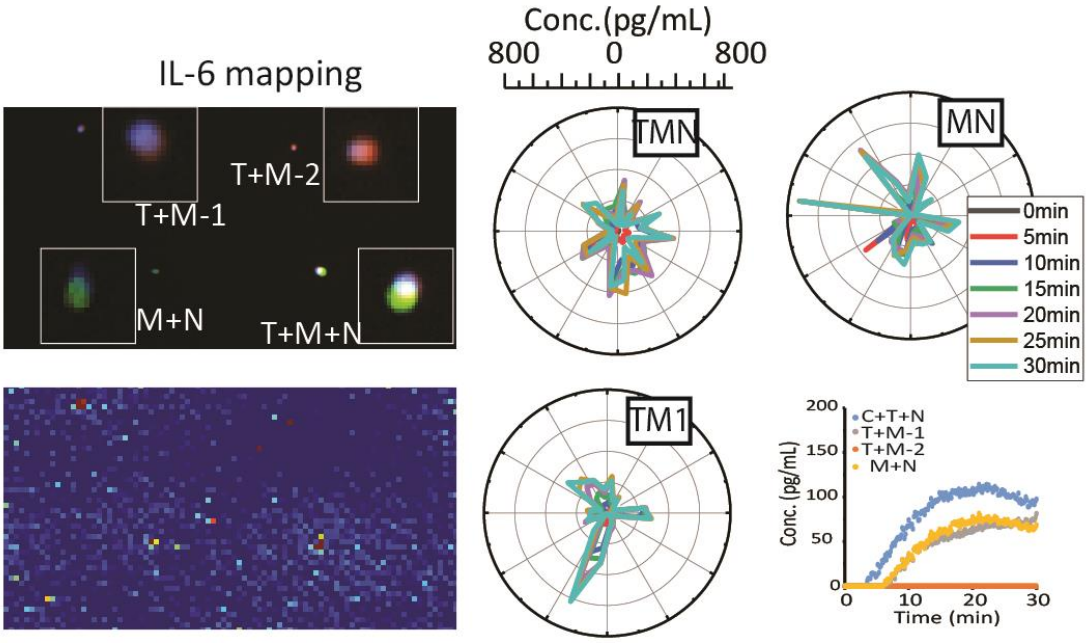

Figure 3.29 IL-6 secretion mapping in coculture environment.

There were various of cell combinations during the coculture. As shown in **Figure 3.27,** CAR-T cell and IL-6 interaction area was observed the IFN-γ secretion with a great local intensity change, while single macrophage, CAR-T cell, and NALM alone

contributed nothing to the IFN-γ express. However, we cannot conclude that the IFN-γ secretion requires the direction interaction involving in the surface ligands binding between the CAR-T cells and NALM-6. In **Figure 3.28**, IFN-γ was observed to be secreted from single T cells from single T cells, while interaction between macrophage and NALM-6 didn't show the IFN-γ expression. In **Figure 3.29**, IL-6 secretion was observed in macrophage-NALM-6, macrophage-CAR-T cells, and macrophage-NALM-6-CAR-T cells interactions. The heterogeneity of secretion during the interaction between macrophage and CAR-T cell was also observed in the figure as one combination was active in IL-6 expression while another one was not.

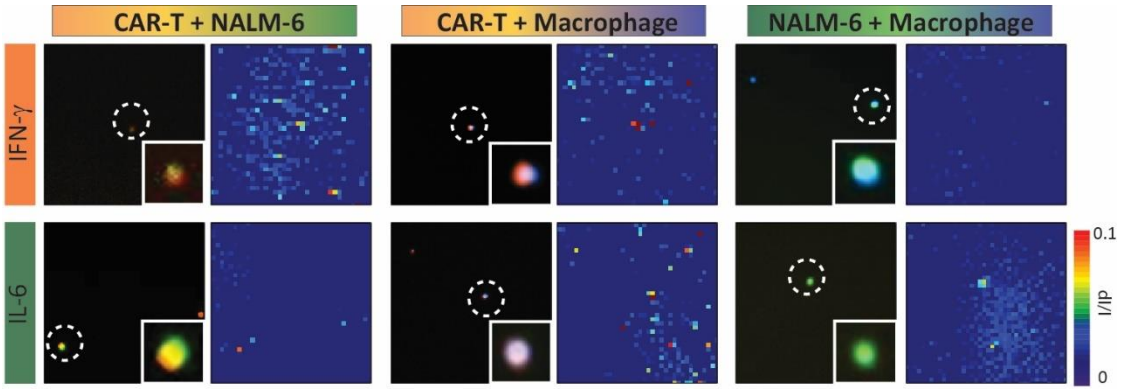

Figure 3.30 IL-6 and IFN-γ secretion mapping of two-cell interaction. All the secretion mapping were at 30 min.

We compared and analyzed the secretion profiles in two-cell interaction conditions. **Figure 3.30** showed cell secretion images after 30 mins in different groups. Tumor-CAR T cells interaction produced negligible level of IL-6 while IFN-γ secretion was observed. It means that IL-6 is not necessary for CAR-T cell activity. Besides, higher IL-6 and IFN-γ levels were observed when CAR-T cells directly interact with

macrophage. It indicated that ligand interactions could further help active cell functions, although there were still Il-6 secretions from single macrophage without ligand interactions with CAR-T cells. Direct contact may not be an essential condition for IL-6 secretion of macrophage. Besides, IL-6 secretions were also observed in macrophage-tumor cell interactions while IFN-γ secretion was not present. It demonstrated that macrophage could be a major source of IL-6 secretions during CRS process[235,237].

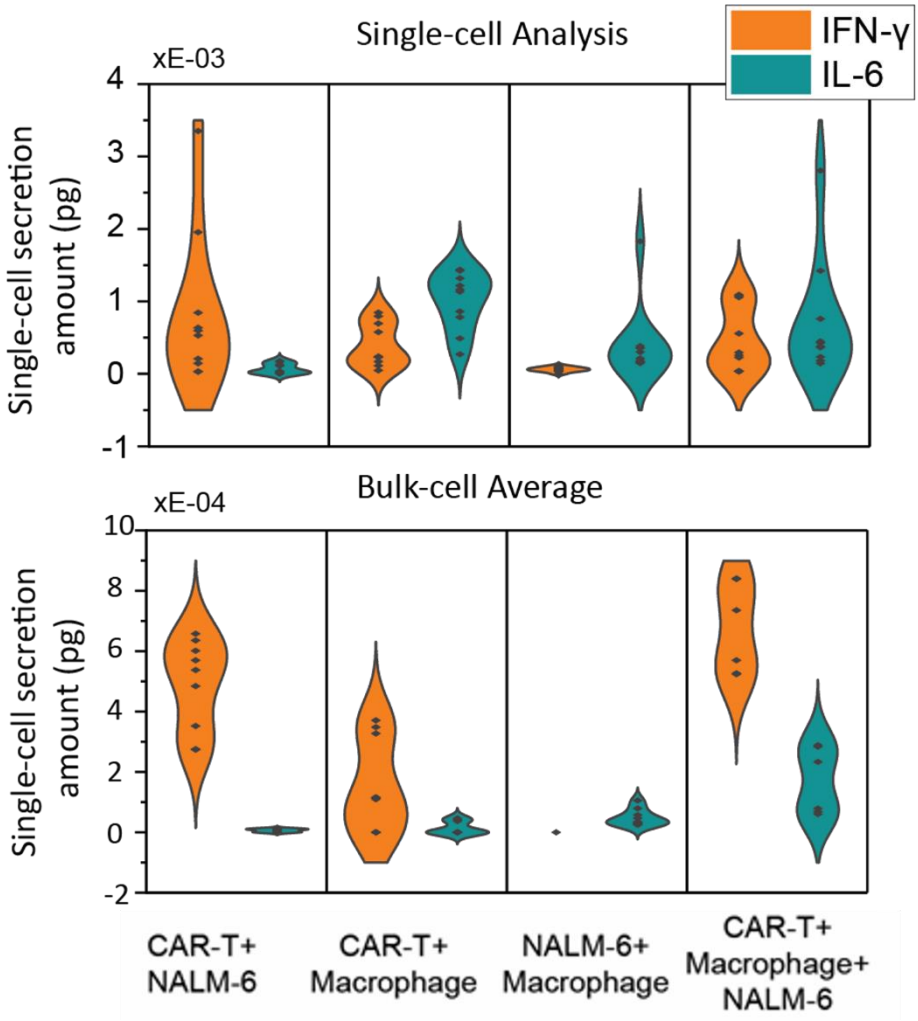

Figure 3.31 IL-6 and IFN-γ secretion amounts from single cells. The results were obtained from nanoplasmon ruler single-cell secretion imaging and ELISA assay.

We compared the IL-6 and IFN-γ secretion amounts from single cells using both the single-cell imaging method and averaged over a large population of cells in ELISA assay. The overall trends were similar. Cocultured environment activates CAR-T cells for more IFN-γ secretions. Macrophages combined with activated T cells resulted in a significant increase in IL-6 levels, suggesting that there were promotion factors for IL-6 secretion when CAR-T cells become activated. On the other side, the single-cell secretion amounts were calculated 1 to 2 orders of magnitude larger than the amounts calculated from the bulk-cell average (**Figure 3.31**). That's probably because that the cell population analysis ignores the frequency of secreting cell. Purified and activated $CD4^+$ T cells were reported to produce IFN-γ at frequencies of 1:50-300[238]. And anther microengraving based-method showed 10.7-13.6% of secreting T cells 6–7 h after stimulation with PMA and ionomycin[208].

3.4 Conclusions

Cytokine mediated intercellular communication is the main mechanism of intercellular communication in immune system[152]. Large population-based analysis may lead to misunderstandings of the results due to the phenotypic heterogeneity in cell populations, even in the cell groups with apparently identical phenotypes[227]. Direct imaging of single-cell secretion process is a powerful route to determine the variations and distinguish the unique subsets related to the quality of an immune response[239] , which is crucial to improve cell therapy. In this study, we presented a novel LSPR-based biosensor to achieve on-chip mapping of single cytokine secretion with high

spatiotemporal resolution. Nanoplasmon ruler exhibited a strong and specific plasmonic coupling signal that enables the high selectivity and sensitivity detection of single molecule binding events. Individual T cells are heterogeneous in secretion rates, secretion amounts. secretion directions were examined and quantified. In particular, the functional heterogeneity of different cells during cellular communication in CAR-T cells induced CRS was also observed. The label-free single cell secretion imaging method was shown to be a powerful tool for the investigation the real-time single cell activity. This approach will establish a new paradigm for understanding the intercellular communication and offer great help in fundamental cell biology research and clinical medicine.

Chapter 4

Nanoplasmonon Ruler for SARS-CoV-2 RBD Detection

4.1 Introduction

COVID-19 pandemic caused by novel coronavirus (SARS-CoV-2) has resulted in more than 6.25 million human deaths and nearly 520 million people have been infected. The continuous mutation of SARS-CoV-2 virus is still the ongoing threat of future pandemic. Most countries are now in the throes of new variants (omicron) which started last winner, leading to overwhelmed testing laboratories and medical institutions. Several experimental effective vaccines have approved by FDA. However, before mass vaccination and medicine to transform the fight against COVID-19, fast and accurate virus test and trace is still crucial to reopen the society safely.

Real-time reverse transcription-polymerase chain reaction (RT-PCR), as the primary method of nucleic acid detections, provides a relatively accurate test result. However, several hours' detection time and laboursome operation procedures make PCR laboratories overwhelmed in such massive daily detections[240]. Rapid viral antigens' tests mainly for virus spike (S) protein, envelope (E) protein, membrane (M) protein, nucleocapsid protein (N) are, then, likely to play a big part in COVID-19 testing strategies[4,241,242]. Among them, S protein is mainly responsible for receptor binding and viral attachment, serving as a key target for vaccines and antibodies. Previous studies have proved that the receptor-binding domain (RBD) in the SARS-CoV-2 S1subunit plays the key role in viral attachment and entry by selectively binding with the ACE2

receptor, which is expressed on host cells membrane, making RBD of the SARS-CoV-2 spike protein a key target for COVID-19 diagnosis.

Aptamers are usually short single-strangled DNA or RNA molecules that bind to a specific target molecule. Compared to antibodies, aptamers have relative smaller size and can be easily chemically synthesized and precisely modified[243]. After binding the analyte, the aptamer goes through conformational change, leading to end-to-end distance change. Nanoplasmon ruler consists of a metallic nanoparticle dimer linked by a biomolecule such as DNA or RNA. The resonating free electrons on both particle surfaces can generate a light scattering spectrum that can be tuned by the interparticle separation. These distance-dependent plasmon resonance behavior and strong scattering intensity during the strong plasmon coupling process make nanoplasmon ruler a promising sensor.

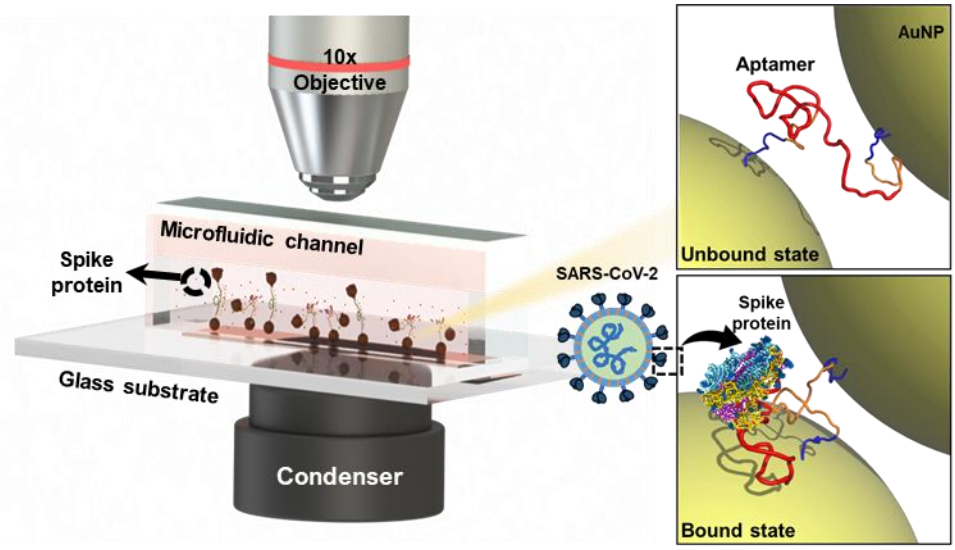

Figure 4.1 Optical setup and schematics for SARS-CoV-2 RBD detection under a dark-field microscope. The plasmon rulers were patterned on a glass substrate

mounted above an oil condenser (NA=1.45, Nikon). While light from a halogen lamp passes through the condenser can illuminate the chip. Only scattering light can be received by objective lens (10x, NA=0.6). After binding to the target antigen, the conformational change of aptamer causes AuNP dimer to approach to each other, leading to strong plasmon coupling and increase of scattering intensity which can be real-time captured by the EMCCD camera.

In this study, we developed a self-assembled nanoplasmon ruler biosensor integrated with a dark -field image system to detect SARS-CoV-2 spike protein RBD. Specifically, the optic setup based on a dark-field scattering scheme will include a dark-field condenser (NA=1.4), a 10x objective (NA=0.6), an ultra-sensitive EMCCD camera (Photometrics). The hybrid plasmonic ruler patterned on the glass substrate will be illuminated by guiding white light into the dark-field condenser from a halogen lamp. The binding of the target molecule brought the paired AuNPs into close proximate, yielding a significantly enhanced plasmonic coupling. Then, the scattering light intensity change from the arrays upon molecule binding will be captured by a EMCCD camera and analyzed using a customized MATLAB code (**Figure 4.1**). The unique optical response from plasmonic coupling is highly specific, allowing the wash-free homogeneous detection, which is the key to achieve the detection with high sensitivity and selectivity.

4.2 Experiments

Synthesis of nanoplasmon ruler

Reagents. 30 nm citrate AuNPs were purchased from nanoComposix. SARS-CoV-2

RBD, SARS-CoV-2 Spike S1 subunit, SARS-CoV-2 Spike S2 subunit, SARS-CoV-2 nucleocapsid were purchased from RayBiotech. Redesigned SARS-CoV-2 RBD aptamer were synthesized by Integrated DNA Technologies (IDT) with HPLC purification. Phosphate-buffered saline (PBS, pH=7.4, including 136.8 mM NaCl, 10.1 mM Na_2HPO_4, 2.7 mM KCl, 1.8 mM KH_2PO_4, 0.55 mM $MgCl_2$) and viral transport medium (VTM, 2% FBS,100 μg/mL Gentamicin, and 0.5 μg/mL Amphotericin in a Hanks Balanced salt solution base), were used as detection buffer.

APTES functioned glass. The glass slide was first washed by Piranha solution (H_2SO_4:H_2O_2 = 3:1 v/v) for 10 minute and dried in the oven. Then, the slide was further cleaned with plasma for 3 min under 100w power and immersed in 1% (v/v) APTES solution overnight under room temperature. After that, the glass slides were wash by ethanol and DI water.

Plasmon ruler assembling. Nanoplasmon rulers were assembled step by step on the APTES-functioned glass slide through PDMS microfluidic channels (400 μm (W) x 2.5 cm (L) x 50 μm). First, citrate AuNPs were self-assembled on the glass surface through electrostatic interactions. AuNPs stock solution (0.5 nM, 30 nm) was loaded into each sensor chamber and incubated overnight.

Aptamer functioned AuNP was achieved by forming Au-S bond during the interaction between AuNP and the thiol group on the one end of the aptamer. DNA aptamer targeting human SARS-CoV-2 RBD were first reduced by 10 mM TCEP solution to fully reduce to oxidized thiol-modified oligos for 1h. Then, the aptamer solution was

diluted to 10-100 x working concentration by Nuclease-free Duplex Buffer (30 mM Hepes, pH 7.5, 100 mM KAc) and heated to 90-95 °C for 5 min. After cooling to the room temperature, the folded aptamer was diluted to 1 nM in TE buffer. Prepared aptamer solution was loaded into microfluidic channels and incubated overnight. After that, streptavidin functioned AuNP (100nm SA solution mixture with 0.5 nm AuNPs for 1h at pH 11) was loaded into sensor chamber and incubated overnight to bind with biotin group on the other side of the aptamer to form the nanoplasmon ruler.

COMSOL simulation

Electric filed distribution and scattering cross-section simulation of AuNP dimer with different interparticle separations were simulated using COMSOL. We predict the electric field distribution near the surface of AuNP dimer upon interaction with the external electric filed. The AuNP size is 30nm. We defined far-field domain surrounding the AuNP dimer with a radium of half the wavelength of incident light and a perfectly match layer of the same thickness, in which the scattering light decays exponentially. The incident light was set parallel to the dimer axis. The hot pot between the dimer gap γshowed the strong plasmon resonance. We also investigated the scattering intensity when incident light was perpendicular to the dimer axis, the weak electric filed distributed surrounding the AuNP dimer proved the negligible contributions of the light to the scattering intensity change. We also predict the influence of gap distance on the scattering cross section change. It is shown that the significant change occurred in the small gap distance.

Coarse-grained discrete molecular dynamics (DMD) simulations

In DMD simulations, temperatures were in the reduced unit of kcal/(mol•kB) and we used eight replica simulations with following temperatures: 0.200, 0.225, 0.250, 0.270, 0.300, 0.333, 0.367, and 0.400. We employed the weighted histogram analysis method to compute the distribution of end-to-end distances at T=0.300.

Surface plasmon resonance analysis

Surface plasmon resonance (SPR) experiments were performed using a BIAcore 2000 biosensor system to measure the binding affinity of selected aptamers. The chip surface was functioned with SARS-CoV-2 RBD aptamer. 6-Mercapto -1-hexanol solution were used to block the chip surface. After stabilizing the baseline, at least five different concentrations of the SARS-COV-2 spike protein solution were injected into the flow cells. The protein surface was regenerated with 10 mM NaOH after injection of each sample and re-equilibrated with the running buffer. The SPR signal were analyzed to calculate the association rate constant ka and the dissociation rate constant kd using BIA evaluation software (Version 3.2, BIAcore).

LSPR detection

The prepared nanoplasmon ruler functioned chip was mounted on sample stage of a dark-field microscope (Nikon N-elips) which was able to perform the automated time-lapse image record. The back of the chip was attached with a dark-field microscope condenser (NA=0.6, Nikon) via lens oil. Before doing the measurement, PDMS layer

used for plasmon ruler function was removed immediately and replaced with another sample-loading PDMS microfluidic channels perpendicularly. The sample was automatically loaded into the channel with 0.1uL/min through a syringe pump during the 30-min measurement (**Figure 4.2**).

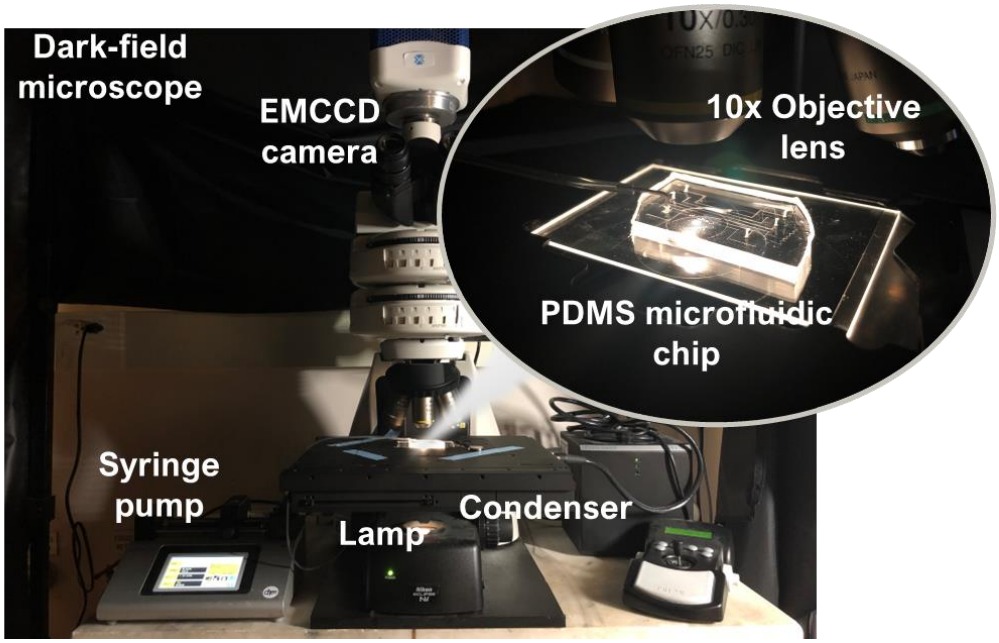

Figure 4.2 Experiment setup for LSPR detection.

Enzyme-linked immunosorbent assay (ELISA)

The ELISA kit was purchased from Elabscience (Car.No E-EL-5605). The plate has been pre-coated with an antibody specific to SARS-CoV-2 S1RBD. Standards or samples are added to the micro-ELISA plate wells and combined with the specific antibody. Then a biotinylated detection antibody specific for SARS-CoV-2 S1RBD and Avidin-Horseradish Peroxidase (HRP) conjugate are added successively to each micro plate well and incubated. Free components are washed away. The substrate solution is added to each well. Only those wells that contain SARS-CoV-2 S1RBD, biotinylated

detection antibody and Avidin-HRP conjugate will appear blue in color. The enzyme-substrate reaction is terminated by the addition of stop solution and the color turns yellow. The optical density (OD) is measured spectrophotometrically at a wavelength of 450 nm ± 2 nm.

4.3 Results and discussion

4.3.1 Design an DNA aptamer with a robust conformational switch

Effective target detection by the plasmon ruler requires a controllable and large conformation change before and after target molecule binding. Since a given DNA/RNA aptamer does not necessarily undergo end-to-end distance change upon antigen binding, we propose a ribosome switch to force the aptamer to have “off” state and “on” state by adding a competing short complementary sequence to a part of reported aptamer in either the 5’ or 3’ regions[244]. The stability of redesigned structure sequence (ΔGoff) is stronger than the stability of the "on" state of the aptamer alone (ΔGon) but weaker than that of the aptamer-target complex (ΔGon+ΔGbinding). The redesigned aptamer prefers the "off" state before binding but switches to the "on" state in the presence of the target molecule. We introduce a 14-nt sequence to the 5’ end and 13-nt sequence to the 3’ end (**Figure 4.3**). The coarse-gained discrete molecular dynamics (DMD) was performed to estimate the conformational change of designed aptamer in “on” and “off” state showing by the simplified three-bead nucleotide model, where different colors of beads corresponding to groups of linkers, designed terminal,

and original terminal (**Figure 4.4**). The "On" state had the average end-to-end distance of ~8 nm, while the "off" state had the average end-to-end distance of ~12 nm.

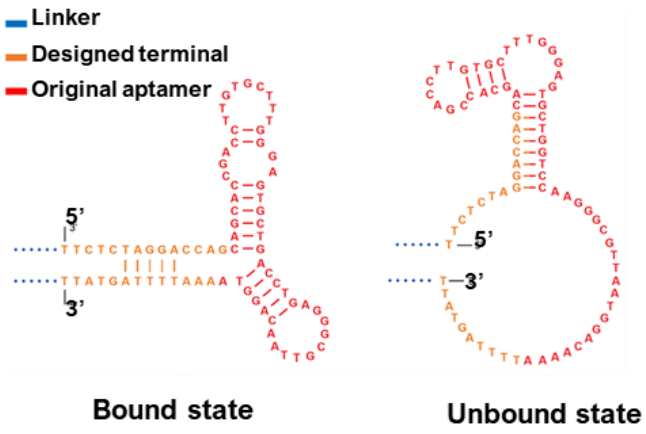

Figure 4.3 Estimated secondary structure of SARS-CoV-2 aptamer at bound and unbound state. Original aptamer bases are marked in red. 10T bases as the linkers on both 3' and 5' end is marked in blue, and designed terminals are marked in orange.

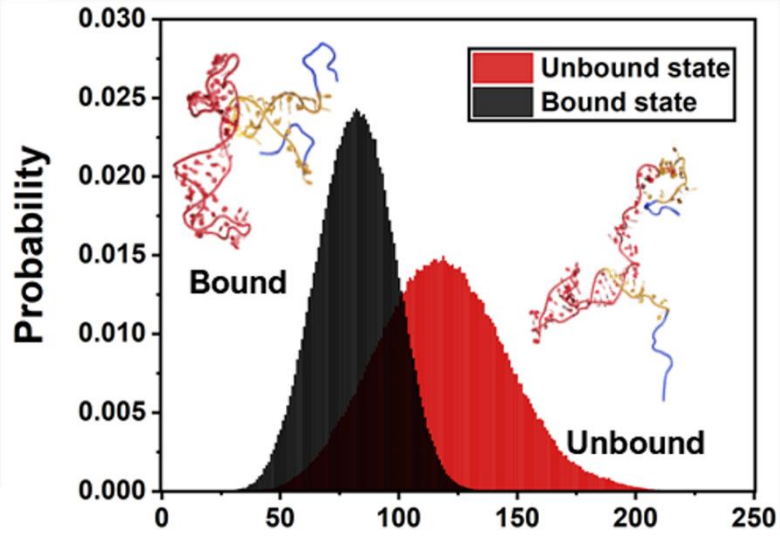

Figure 4.4 The coarse-gained discrete molecular dynamics (DMD) prediction of probability distribution of end-to-end distance. The secondary structures of aptamer at bound and unbound state are shown near the spectrums. The simulation was performed at Temperature of 0.3.

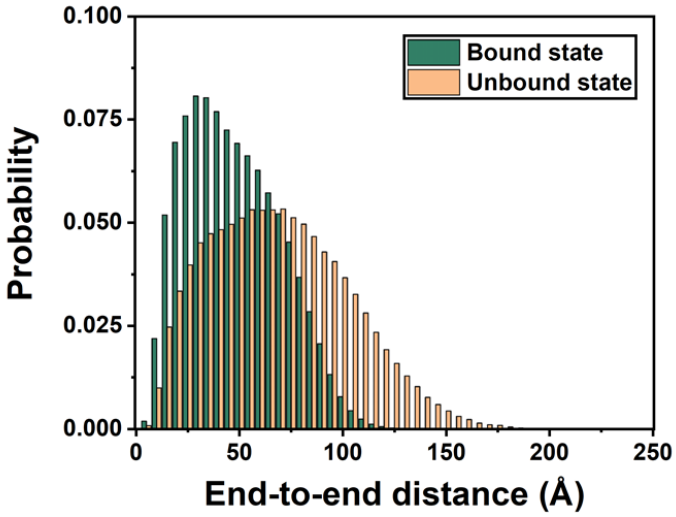

Figure 4.5 Gap distance distributions of nanoplasmon ruler before and after binding to the target.

We also predicted the gap distance distribution between AuNP dimer conjugated with designed aptamer after considering the steric hindrance during the assembling process (**Figure 4.5**). The average gap distance change upon SARS-CoV-2 RBD binding is ~ 4 nm.

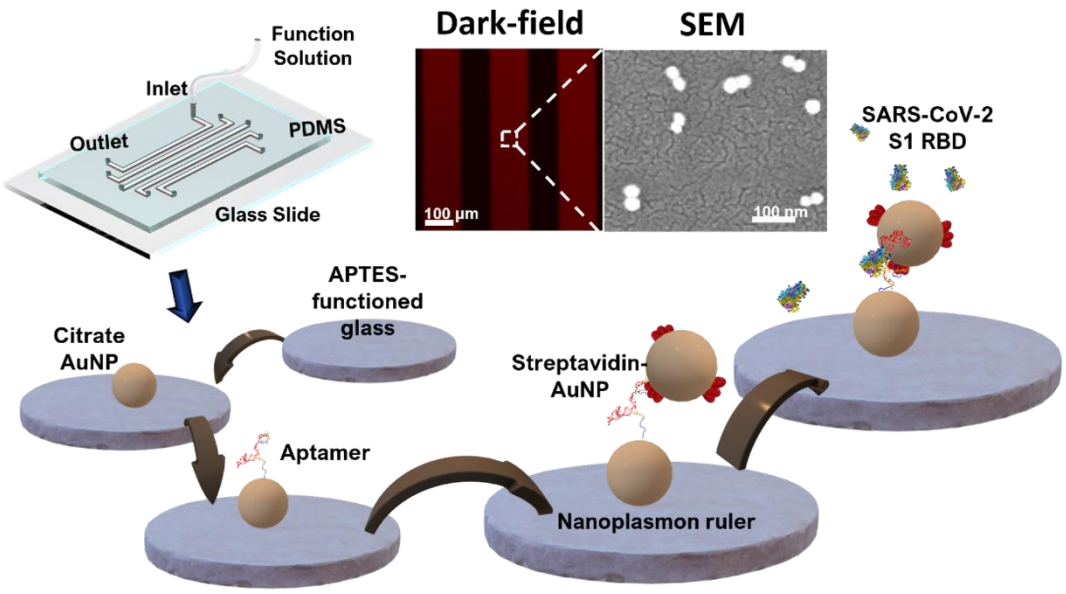

Figure 4.6 Nanoplasmon ruler biosensor chip assembling. Schematic of plasmon ruler assembling process. The aptamer was functioned a thiol group at 5' end and a biotin at 3'end. The whole structure was patterned step-by-step on an APTES-functioned glass subtract using a microfluidic device. Dark-file image and electric scanning electric microscope (SEM) of barcode chip were also showed.

In order to assemble the nanoplasmon ruler, we modified the aptamer with a thiol group on the one end and a biotin group on the other end. 10-T base was also functioned on both sides to serve as a spacer to avoid space steric hindrance. Aptamers can be directly functionalized to AuNPs through Au-S bond on the end of thiol group, while biotin group on the other end of aptamer has high binding affinity with streptavidin. Then, one aptamer can conjugate a bare AuNP and a streptavidin-functioned AuNP to form the final plasmon ruler structure. Every component was patterned step by step on glass slide by a simply designed PDMS microfluidic channel (**see method in Experiment**). A monolayer of citrate AuNPs was first patterned on the glass substrate with the assistant of electrostatic attractive interactions between negatively charged AuNP and positively

charged APTES-functioned glass substrate. Optimized aptamer-to-AuNPs ratio was required to ensure that only one aptamer conjugates with a Au dimer. High aptamer concentration promoted the formation of trimer, pentamer, and AuNPs aggregations, which would lead to a broad scattering spectrum and compromise the sensitivity of sensor, while monomer AuNP made small contributions to final signal due to the week scattering light. Dark-filed image and scanning electron microscope (SEM) image presented well-distributed plasmonic sensors and high plasmon ruler ratio.(**Figure 4.6**)

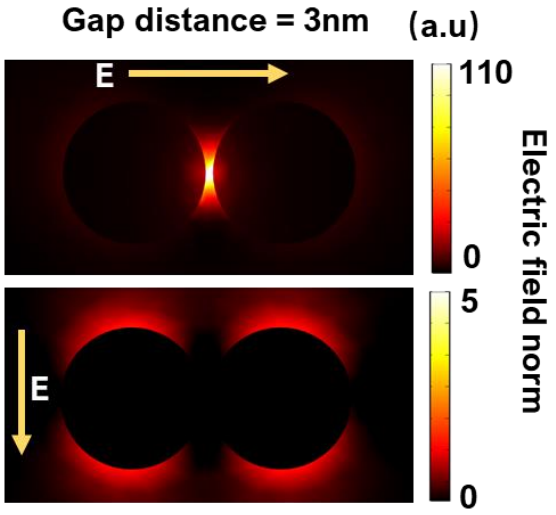

Figure 4.7 Comparation the influence of incident light polarization on the scattering response of AuNP dimer. The arrow indicates the external electric filed direction.

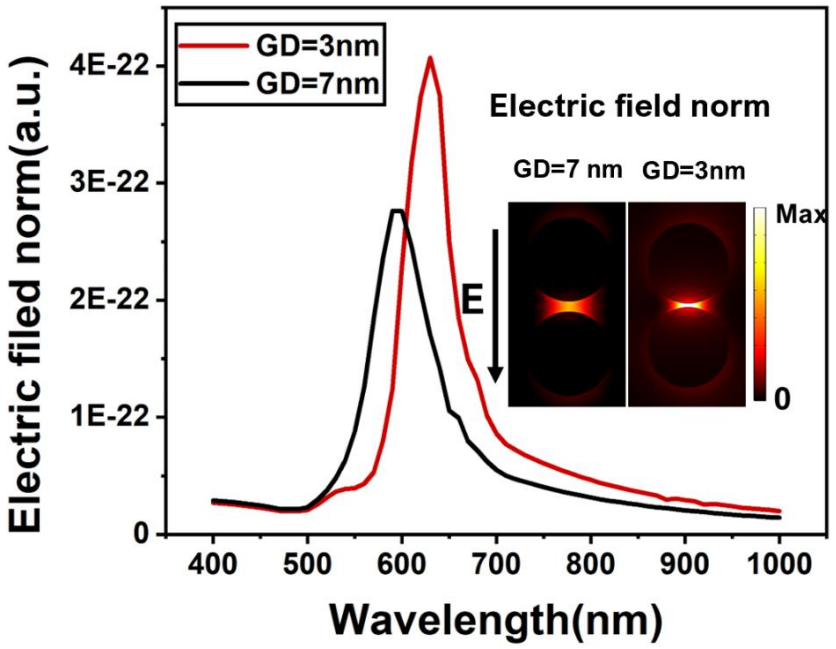

Figure 4.8 COMSOL simulation of scattering spectrum change of nanoplasmon ruler upon antigen binding under consideration of gap distributions.

The electromagnetic interactions between two coupled AuNPs was also simulated by COMSOL Multiphysics to predict how target binding would influence the local electric field intensity near the nanoplasmon ruler surface. The plasmon coupling behavior of AuNP dimer shows polarization dependence (**Figure 4.7**). As the contribution of incident light which is perpendicular to the dimer axis to scattering spectrum change is negligible, the simulation only considers the situation where the polarization direction of incident light is parallel to the dimer axis. As shown in **Figure 4.8**, significant scattering intensity change, and drastic scattering spectrum red shift occur by closing the interparticle distance due to strong plasmon coupling. The induced scattering intensity increase by a factor of 10 allows stronger optical single from the nanoplasmon ruler compared to with single AuNP when the binding occurs. This will lead to an

ultrasensitive cytokine detection with high selectivity as the noise generated by the nonspecific absorption of cytokines on to the AuNP could be negligible.

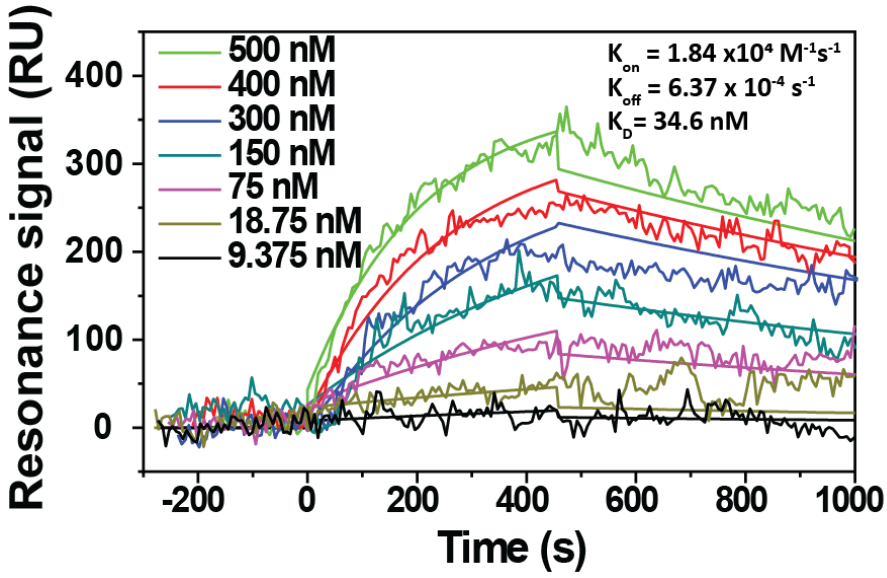

Figure 4.9 SPR detection of SARS-CoV-2 RBD at different concentrations in PBS buffer. The system was washed by PBS buffer after 400s to remove unbinding antigens.

To verify the designed aptamer, we use SPR technology first to characterize the binding kinetic between aptamer and SARS-Cov-2 RBD. The aptamer was immobilized on a Au film chip through Au-S bond. Uncovered chip surface was blocked with bovine serum albumin (BSA) and 6-Mercapto-1-hexanol. 10mM NaOH served as the regeneration buffer. SARS-CoV-2 RBD solutions ranging from 9.375 nM to 500 nM were injected into the SPR chamber for about 400s followed by SPR cell washing with PBS buffer to remove the unspecific binding antigens. The RBD specifically bound to aptamer led to a change of resonance angle. The signals, showed in **Figure 4.9**, were proportional to the analyte concentrations. The equilibrium dissociation constant K_D of the aptamers is 34.6 nm, where association rate constant (k_{on}) is $1.84x10^4 M^{-1}s^{-1}$ and

dissociation rate constant (k_{off}) is $6.37x10^{-4}s^{-1}$. It proved the redesigned aptamer has good affinity to SARS-Cov-2 RBD.

4.3.2 Real-time LSPR biosensing and calibration

The performance of nanoplasmon ruler was identified using LSPR device. To quantify the SARS-Cov-2 concentration, scattering intensity change was recorded at a sensing spot with 250 x 250 pixels (400 x 400 μm^2) under the dark-field microscope by an ultrasensitive electron multiplying CCD (EMCCD, Photometrics) with a frame acquisition rate at every 10 s. 5x5 pixels (8 x 8 μm^2) were set as a detection unit to minimize the system error due to the tiny image vibration. The real-time image of nanoplasmon rulers towards SARS-CoV-2 RBD at concentrations of 10, 100, 500, 1000, 5000 pg/mL was recorded. The relative intensity change $((I-I_0)/I)$ of every image frame during the measurement was subtracted and analysed using a customized MATLAB code. The intensity changes were showed in the form of heatmap (**Figure 4.10a**). According to the real-time plot (**Figure 4.10b**), the binding events reached an equilibrium within 30 minutes.

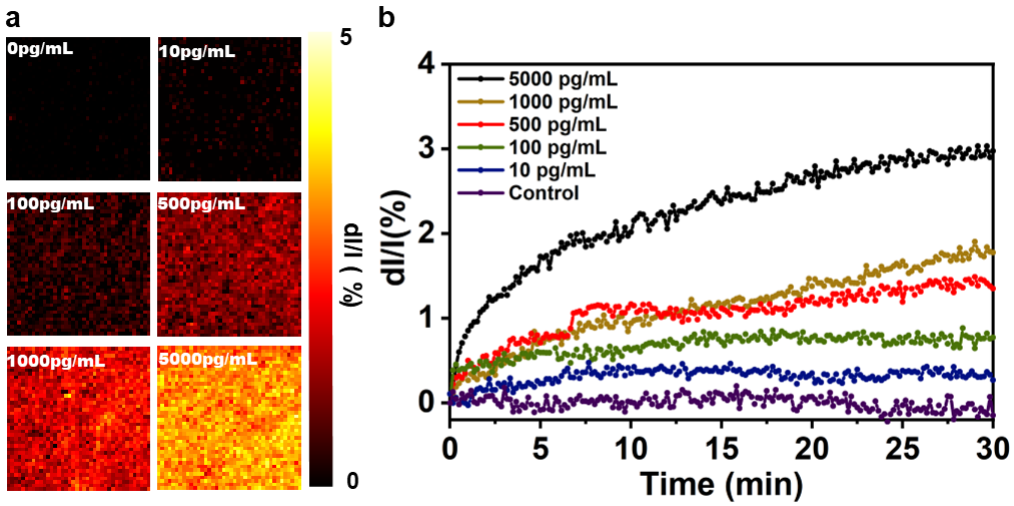

Figure 4.10 LSPR detection of SARS-CoV-2 RBD. (a) Intensity mapping of SARS-CoV-2 RBD detection of different concentrations after 30 min. The imaging area was 45x45 pixels with one pixel of 8x8 μm. (b). Real-time binding curve of SARS-CoV-2 RBD on nanoplasmon ruler in PBS buffer in 30 min.

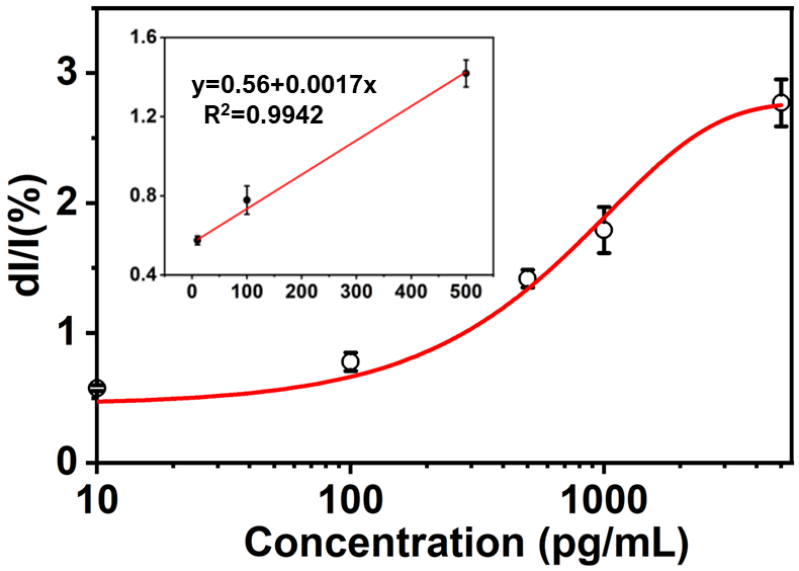

Figure 4.11 Calibration curve for SARS-CoV-2 RBD detection in PBS buffer.

We performed a control experiment to measure the background signal of nanoplasmon ruler biosensor with pure PBS buffer. The average background change is ~0.3% with standard deviation of 0.02%. The Limited of detection (LOD) of the sensor was thus

obtained from 3σ/k, where σ is standard deviation of system error and k is defined as the slope of the calibration curves using linear curve-fitting (**Figure 4.11**). The LOD is down to 35 pg/mL of SARS-CoV-2 in PBS, showing high sensitivity in antigen detection.

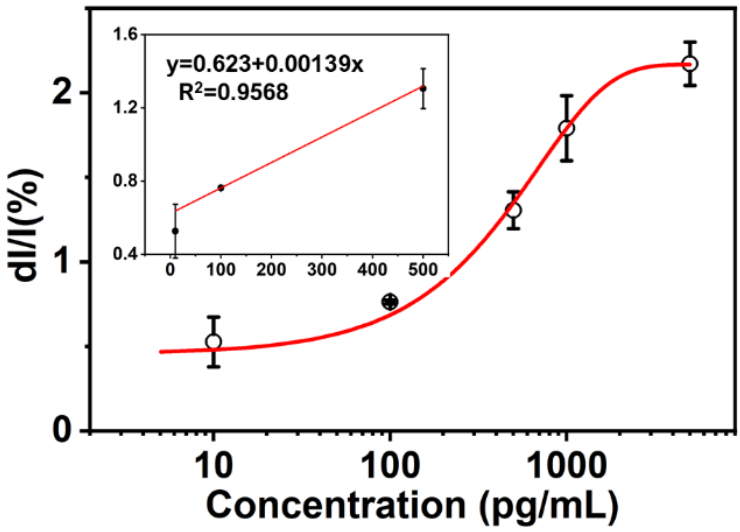

Figure 4.12 Calibration curve for SARS-CoV-2 RBD detection in virus transport medium.

Clinical diagnosis of COVID-19 is usually performed in virus transformed medium (VTM). It helps to maintain the viability and thus virulence of collected samples, while some other molecules such as fetal bovine serum (FBS), Hanks' Balanced salt, and antibiotics are also introduced at the same time. The aptamer performance may be influenced by the different medium environments. We performed the antigen detection in pure virus transport medium (VTM). The nanoplasmon ruler showed good binding affinity to the SARS-CoV-2 RBD with LOD of 100 pg/mL, revealing the great potential of nanoplasmon ruler sensor in clinical sample detection (**Figure 4.12**).

4.3.3 Validation with ELISA method.

The enzyme-linked immunosorbent assay (ELISA) is recognised as the "gold-standard" method for biochemistry detection with high sensitivity. However, laborious regent processing procedures including multiple steps of staining, washing, and blocking are time consuming and have constrained it to detect cytokines at a time snapshot and prohibited it in real-time dynamic analysis. Here, we used the ELISA platform to validate immunoassay results obtained from nanoplasmon ruler biosensor. The prepared SARS-COV-2 RBD unknown samples were measured on both two detection systems. We prepared 7 samples with different concentrations. After fitting the data into the calibration curve, we compared the results between LSPR immunoassay and ELISA measurements and observed a great linear correlation (R^2=0.9858), proving the accuracy and reliability of our system (Error! Reference source not found.**a**).

Figure 4.13 Correlation between results obtained from nanoplasmon ruler biosensor and the ELISA for the SARS-CoV-2 RBD sample.

4.3.4 Selectivity validation of nanoplasmon ruler biosensor

Nonspecific cross-reactions could influence the LSPR signal. To validate the selectivity of nanoplasmon ruler sensor, we evaluated the biding performance of nanoplamon ruler against SARS-CoV-2 antigen protein (RBD, S1, S2, nucleocapsid) and MERS-CoV RBD protein at a high concentration (5ng/mL). After 30min, the sensor showed low affinity toward S2 subunit, N protein, and MERS. While approximately 65% of binding events were maintained in several antigens' mixture environment (5ng/mL individually). Besides, the sensor also showed good binding affinity to SARS-CoV-2 S1 protein (**Figure 4.14**). These results demonstrated that the nanoplasmon ruler could recognize RBD in S1 protein and discriminated RBD in relative complex environment.

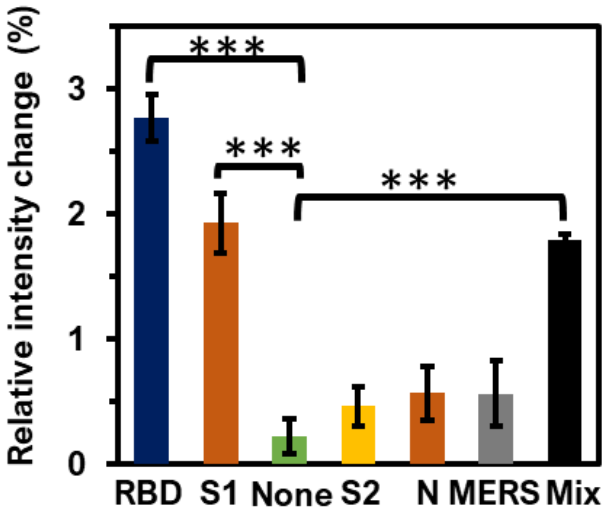

Figure 4.14 Selectivity analysis of nanoplasmon ruler biosensor. Bar graphs represents relative intensity changes after exposure of nanoplasmon ruler biosensor to 5 ng/mL virus protein (RBD, SARS-CoV-2 S1, SARS-CoV-2 S2, SARS-CoV-2 nucleocapsid, and MERS-CoV) for 30 min in PBS buffer. Error bars represent the standard deviation from three independent experiments. Statistical analysis of experimental data by two sample T-test (*:P<0.05, **P<0.01, ***P<0.001).

4.4 Conclusions

Rapid and precise detection of SARS-CoV-2 virus is crucial in controlling the COVID-19 pandemic. In this study, we developed a novel LSPR biosensor by conjugating a AuNP dimer with one strand of DNA aptamer which has high affinity to SARS-CoV-2 RBD. To construct the sensor, we redesigned the aptamer with a controllable conformational change before and after target antigen binding. The significant plasmon coupling between AuNP dimer provides a strong optical signal for SARS-CoV-2 RBD detection. The sensor was able to detect SARS-CoV-2 RBD with high sensitivity and selectivity in real-time in both PBS and VTM medium, providing a new choice for COVID-19 as well as other antigen detections.

Chapter 5

Summary and Future Work

In the whole project, we aim to develop an advanced LSPR-based biosensor system to detect biomolecules accurately and rapidly. Using this nanoplasmonic-based immunoassays, cytokines and SARS-CoV-2 spike proteins were detected in a label-free way with high sensitivity. Furthermore, a novel nanoplasmon ruler platform was fabricated to achieve direct visualization of single-cell cytokine secretion and to investigate intercellular communications. Following conclusions can be made:

1) We have developed a novel multiplexed cytokine-profiling platform based on a label-free localized surface plasmon (LSPR)-based nanoplasmonic biosensing technology with high sensitivity, short sampling-to-detection time, and low sample analysis cost. Using this platform, we investigated the influence of plasmon protein on Aβo- and Aβf-induced immune responses by evaluated and compared cytokine secretion (TNF-a and IL-6) levels from immune cells (T cells, B cells, or monocytic cells), implicating the intertwined relationship between the amyloidosis and immunogenicity of Aβ.

2) We have developed a self-assembled ‘nanoplasmon ruler’ sensor consisting of three key components: a substrate gold AuNP, a coupling AuNP, and a single short strand DNA (i.e. aptamer that binds a specific target analyte). The structure has shown great potential in detecting secreted biomolecules with superior sensitivity and specificity in real-time. Upon target analyte binding, the unique optical response

from plasmonic coupling is highly specific, allowing the wash-free homogeneous detection, which is the key to achieve the spatiotemporal mapping of cytokine secretion from individual cells. Key parameters affecting the desired nanoplasmon ruler formation, such as NP size, NP surface function, and stoichiometric particle-aptamer ratio were carefully examined to yield a uniform mono dispersed NP dimer structure on the glass substrate. 3) To improve aptamer performance, we exploited a ribosome switch design using a SOMAmers (Slow Off -rate Modified Aptamers) SL1025 selected through SELEX formed a co-crystal structure with IL-6 through two distinct domains, a G-quarter domain and a stem-loop domain that bind IL-6 in a clamp-like manner. By intentionally adding several nucleotides at the end of SMOAmer SL1025 sequence, we force the aptamer to have 'off' state and 'on' state (before and after binding) that shows significant conformation change thus large end-to-end distance before and after binding with cytokines. IFN-γ and SARS-Cov-2 aptamers were also designed with similar method. The redesigned aptamers have good affinity to target cytokines. The method could be employed to design other aptamers targeting different cytokines.

3) We demonstrated using the nanoplasmon ruler for visualizing cytokine secretion patterns from single immune cells. We first used a purified Jurkat cell line as a model system for T help cell 1 (Th1) lymphocyte, whose immune functions are critically important for intercellular communication in the immune system. We stimulated selected immune cells using phorbol 12-myristate13-acetate (PMA) and

ionomycin. Then, we can directly visualize and analyze the dynamic cytokine secretion process from each individual immune cell by capturing the dark-field images continuously. The distinct secretion patterns clearly indicate the functional heterogeneity of individual immune cells, which has rarely been observed by previous studies. Since such imaging process automated by a motorized stage can scan across (~10 sec per frame) a large area of interest, the high spatiotemporal resolution enables investigations on the secretion and diffusion dynamics of released cytokines in a single-cell level. We compared the cytokine secretion rate and diffusion coefficient of IL-6 and IFN-γ, and further revealed the heterogeneity of individual cells. .

4) We applied our nanoplasmon ruler biosensor to directly visualize the IL-6 and IFN-γ secretion profile during the interactions among CAR-T cells, B-ALL cells, and macrophages. We prepared CD 19 CAR-T cells by infecting primary splenic C57BL/6 CD8+ T cells with a retroviral construct allowing ectopic expression of a CD19-targeting CAR, as well as RFP for fluorescent cell tracing. To investigate the intercellular communication, the real-time secretion profile of different types of cells were imaged without any agent stimulation. CAR T-cells, B-ALL, and macrophage were cocultured and loaded onto the sensor surface. The cell location and cell type were determined by fluorescence microscope. IL-6 and IFN-γ secretion from paired cells were measured, respectively. The cell secretion mapping and quantification showed that CAR-T cells activated by B-ALL secreted IFN-γ,

but no obviously IL-6 secretion. The IL-6 secretion was observed in the present of macrophage. We analyzed the single cell secretion dynamics for these three kinds of cells individually in the mixture and found that more IL-6 secretion was released from macrophages than that from CAR T-cells and B-ALL. Overall, it indicates that the crosstalk among the CAR T-cell, macrophage, and B-ALL cell are critical in regulating CAR T-cell function and CRS. Such a proof-of-concept nanoplasmon ruler sensing platform could be readily extended in the proposed study to characterize the polyfunctional CAR T-cells and unveil the key signal mediators in CAR T-cell immunotherapy.

5) In the face of the ongoing COVID-19 testing pressure, we applied our nanoplasmon ruler biosensor to detect SARS-CoV-2 RBD. The nanoplasmon ruler showed good selectivity and binding affinity to the SARS-CoV-2 RBD with LOD of 100 pg/mL in both PBS and VTM medium. Besides, low cost and short detection time (30min) make it promising for COVID-19 as well as other antigen detections.

The sensor platform can be further improved in several aspects:

1) We have demonstrated the application of nanoplasmon ruler for imaging of intercellular communication between CAR-T, B-ALL, and microphage. The method can be further used to analyzed other kinds of cytokines and cell types for evaluate the cellular behaviors.

2) Simultaneously mapping multiple cytokine detection is still challenge. It is reported that an active single cell can secret several kinds of cytokines[223]. In intercellular

communications, multiplex imaging of sequential proteins secretion from individual immune cells will offers a more in-depth and comprehensive information of cellular functions and help to reveal correlates of immunological intervention.

3) Here, we demonstrated a 2D cytokine secretion model. The spatial resolution for single-cell secretion imaging can be further improved in an 3D model. That may need a well-designed microfluidic with homogeneous assembled biosensors in 3D space.

Reference

1. Shrivastav, A. M., Cvelbar, U. & Abdulhalim, I. A comprehensive review on plasmonic-based biosensors used in viral diagnostics. *Communications Biology* vol. 4 (2021).
2. Asghari, A. *et al.* Fast, accurate, point-of-care COVID-19 pandemic diagnosis enabled through advanced lab-on-chip optical biosensors: Opportunities and challenges. *Applied Physics Reviews* vol. 8 (2021).
3. Menon, S., Mathew, M. R., Sam, S., Keerthi, K. & Kumar, K. G. Recent advances and challenges in electrochemical biosensors for emerging and re-emerging infectious diseases. *Journal of Electroanalytical Chemistry* vol. 878 (2020).
4. Seo, G. *et al.* Rapid Detection of COVID-19 Causative Virus (SARS-CoV-2) in Human Nasopharyngeal Swab Specimens Using Field-Effect Transistor-Based Biosensor. *ACS Nano* **14**, 5135–5142 (2020).
5. Park, M. & Heo, Y. J. Biosensing Technologies for Chronic Diseases. *Biochip Journal* vol. 15 (2021).
6. Sharifi-Rad, M. *et al.* Lifestyle, Oxidative Stress, and Antioxidants: Back and Forth in the Pathophysiology of Chronic Diseases. *Frontiers in Physiology* vol. 11 (2020).
7. Conversano, C. Common psychological factors in chronic diseases. *Frontiers in Psychology* vol. 10 (2019).
8. Anderson, E. & Durstine, J. L. Physical activity, exercise, and chronic diseases: A brief review. *Sports Medicine and Health Science* vol. 1 3–10 (2019).
9. *Race, Ethnicity and Alzheimer's in America*. (2021).
10. Zhang, Z. *et al.* Advanced Point-of-Care Testing Technologies for Human Acute Respiratory Virus Detection. *Advanced Materials* (2021) doi:10.1002/adma.202103646.

11. Wu, J., Dong, M., Rigatto, C., Liu, Y. & Lin, F. Lab-on-chip technology for chronic disease diagnosis. *npj Digital Medicine* **1**, (2018).
12. Brücher, B. L. D. M. & Jamall, I. S. Cell-cell communication in the tumor microenvironment, carcinogenesis, and anticancer treatment. *Cellular Physiology and Biochemistry* vol. 34 213–243 (2014).
13. Labib M & Kelley SO. Single-cell analysis targeting the proteome. *Nature Reviews Chemistry* **4**, 143–158 (2020).
14. Ren, X. *et al.* Insights Gained from Single-Cell Analysis of Immune Cells in the Tumor Microenvironment. *Annu Rev Immunol* **39**, 583–609 (2021).
15. Hodzic, E. Single-cell analysis: Advances and future perspectives. *Bosnian Journal of Basic Medical Sciences* **16**, 313–314 (2016).
16. Hu, P., Zhang, W., Xin, H. & Deng, G. Single cell isolation and analysis. *Frontiers in Cell and Developmental Biology* vol. 4 (2016).
17. Patel, S., Nanda, R., Sahoo, S. & Mohapatra, E. Biosensors in health care: The milestones achieved in their development towards lab-on-chip-analysis. *Biochemistry Research International* vol. 2016 (2016).
18. Naresh, V. & Lee, N. A review on biosensors and recent development of nanostructured materials-enabled biosensors. *Sensors (Switzerland)* vol. 21 1–35 (2021).
19. Rapp, B. E., Gruhl, F. J. & Länge, K. Biosensors with label-free detection designed for diagnostic applications. *Analytical and Bioanalytical Chemistry* vol. 398 2403–2412 (2010).
20. Syahir, A., Usui, K., Tomizaki, K., Kajikawa, K. & Mihara, H. Label and Label-Free Detection Techniques for Protein Microarrays. *Microarrays* **4**, 228–244 (2015).
21. Sang, S. *et al.* Progress of new label-free techniques for biosensors: A review. *Critical Reviews in Biotechnology* **36**, 465–481 (2016).

22. Khansili, N., Rattu, G. & Krishna, P. M. Label-free optical biosensors for food and biological sensor applications. *Sensors and Actuators B: Chemical* **265**, 35–49 (2018).

23. Garzón, V., Pinacho, D. G., Bustos, R. H., Garzón, G. & Bustamante, S. Optical biosensors for therapeutic drug monitoring. *Biosensors (Basel)* **9**, (2019).

24. Chen, Y. T. *et al.* Review of Integrated Optical Biosensors for Point-Of-Care Applications. *Biosensors* vol. 10 (2020).

25. Jones, R. R., Hooper, D. C., Zhang, L., Wolverson, D. & Valev, V. K. Raman Techniques: Fundamentals and Frontiers. *Nanoscale Research Letters* vol. 14 (2019).

26. Liu, L., He, F., Yu, Y. & Wang, Y. Application of FRET Biosensors in Mechanobiology and Mechanopharmacological Screening. *Frontiers in Bioengineering and Biotechnology* **8**, (2020).

27. Chen, C. & Wang, J. Optical biosensors: An exhaustive and comprehensive review. *Analyst* vol. 145 1605–1628 (2020).

28. Damborský, P., Švitel, J. & Katrlík, J. Optical biosensors. *Essays in Biochemistry* **60**, 91–100 (2016).

29. Walt, D. R. Optical methods for single molecule detection and analysis. *Analytical Chemistry* **85**, 1258–1263 (2013).

30. Tian, Y., Zhang, L. & Wang, L. DNA-Functionalized Plasmonic Nanomaterials for Optical Biosensing. *Biotechnology Journal* vol. 15 (2020).

31. Bannas, P., Hambach, J. & Koch-Nolte, F. Nanobodies and nanobody-based human heavy chain antibodies as antitumor therapeutics. *Frontiers in Immunology* vol. 8 (2017).

32. Morales, M. A. & Halpern, J. M. Guide to Selecting a Biorecognition Element for Biosensors. *Bioconjugate Chemistry* **29**, 3231–3239 (2018).

33. Salvador, J. P., Vilaplana, L. & Marco, M. P. Nanobody: outstanding features for diagnostic and therapeutic applications. *Analytical and Bioanalytical Chemistry* vol. 411 1703–1713 (2019).

34. Wang, W., Yuan, J. & Jiang, C. Applications of nanobodies in plant science and biotechnology. *Plant Molecular Biology* vol. 105 43–53 (2021).

35. Rahbarizadeh, F., Ahmadvand, D. & Sharifzadeh, Z. Nanobody; An old concept and new vehicle for immunotargeting. *Immunological Investigations* **40**, 299–338 (2011).

36. de Meyer, T., Muyldermans, S. & Depicker, A. Nanobody-based products as research and diagnostic tools. *Trends in Biotechnology* **32**, (2014).

37. Huertas, C. S., Calvo-Lozano, O., Mitchell, A. & Lechuga, L. M. Advanced Evanescent-Wave Optical Biosensors for the Detection of Nucleic Acids: An Analytic Perspective. *Frontiers in Chemistry* vol. 7 (2019).

38. Kher, G., Trehan, S. & Misra, A. Antisense Oligonucleotides and RNA Interference. in *Challenges in Delivery of Therapeutic Genomics and Proteomics* 325–386 (Elsevier Inc., 2011). doi:10.1016/B978-0-12-384964-9.00007-4.

39. Rosch, J. C., Balikov, D. A., Gong, F. & Lippmann, E. S. A systematic evolution of ligands by exponential enrichment workflow with consolidated counterselection to efficiently isolate high-affinity aptamers. *Engineering Reports* **2**, (2020).

40. Ni, S. *et al.* Recent Progress in Aptamer Discoveries and Modifications for Therapeutic Applications. *ACS Applied Materials and Interfaces* vol. 13 9500–9519 (2021).

41. Lakhin, A. v, Tarantul, V. Z. & Gening, L. v. Aptamers: Problems, Solutions and Prospects. *34 | ActA nAturAe |* **5**, 2013 (2013).

42. Xie, S. *et al.* Functional Aptamer-Embedded Nanomaterials for Diagnostics and Therapeutics. *ACS Applied Materials and Interfaces* vol. 13 9542–9560 (2021).

43. McConnell, E. M., Nguyen, J. & Li, Y. Aptamer-Based Biosensors for Environmental Monitoring. *Frontiers in Chemistry* vol. 8 (2020).

44. Yoo, H., Jo, H. & Oh, S. S. Detection and beyond: challenges and advances in aptamer-based biosensors. *Materials Advances* **1**, 2663–2687 (2020).

45. Wang, J., Munir, A., Li, Z. & Zhou, H. S. Aptamer-Au NPs conjugates-enhanced SPR sensing for the ultrasensitive sandwich immunoassay. *Biosensors and Bioelectronics* **25**, 124–129 (2009).

46. Muhammad, M. & Huang, Q. A review of aptamer-based SERS biosensors: Design strategies and applications. *Talanta* vol. 227 (2021).

47. Zhou J & Rossi J. Aptamers as targeted therapeutics current potential and challenges. *Nature reviews Drug discovery* **16**, 181–202 (2017).

48. Zhang, Y., Lai, B. S. & Juhas, M. Recent advances in aptamer discovery and applications. *Molecules* vol. 24 (2019).

49. Chen, J. *et al.* Nanomaterials as photothermal therapeutic agents. *Progress in Materials Science* vol. 99 1–26 (2019).

50. Reineck, P. & Gibson, B. C. Near-Infrared Fluorescent Nanomaterials for Bioimaging and Sensing. *Advanced Optical Materials* vol. 5 (2017).

51. Astruc, D. Introduction: Nanoparticles in Catalysis. *Chemical Reviews* vol. 120 461–463 (2020).

52. Huang, Z., Zhang, A., Zhang, Q. & Cui, D. Nanomaterial-based SERS sensing technology for biomedical application. *Journal of Materials Chemistry B* vol. 7 3755–3774 (2019).

53. Zeng, S., Baillargeat, D., Ho, H. P. & Yong, K. T. Nanomaterials enhanced surface plasmon resonance for biological and chemical sensing applications. *Chemical Society Reviews* vol. 43 3426–3452 (2014).

54. Wang, X., Li, F. & Guo, Y. Recent Trends in Nanomaterial-Based Biosensors for Point-of-Care Testing. *Frontiers in Chemistry* **8**, (2020).

55. Chen, P. *et al.* Multiplex serum cytokine immunoassay using nanoplasmonic biosensor microarrays. *ACS Nano* **9**, 4173–4181 (2015).

56. Agharazy Dormeny, A., Abedini Sohi, P. & Kahrizi, M. Design and simulation of a refractive index sensor based on SPR and LSPR using gold nanostructures. *Results in Physics* **16**, (2020).

57. Willets, K. A. & van Duyne, R. P. Localized surface plasmon resonance spectroscopy and sensing. *Annual Review of Physical Chemistry* **58**, 267–297 (2007).

58. Chen, H., Kou, X., Yang, Z., Ni, W. & Wang, J. Shape- and size-dependent refractive index sensitivity of gold nanoparticles. *Langmuir* **24**, 5233–5237 (2008).

59. Xu, T. & Geng, Z. Strategies to improve performances of LSPR biosensing: Structure, materials, and interface modification. *Biosensors and Bioelectronics* vol. 174 (2021).

60. Sugawa, K. *et al.* Refractive index susceptibility of the plasmonic palladium nanoparticle: Potential as the third plasmonic sensing material. *ACS Nano* **9**, 1895–1904 (2015).

61. Wang, C., Cai, Y., Maclachlan, A. & Chen, P. Novel Nanoplasmonic-Structure-Based Integrated Microfluidic Biosensors for Label-Free in Situ Immune Functional Analysis: A review of recent progress. *IEEE Nanotechnology Magazine* vol. 14 46–53 (2020).

62. Choi, H. K., Lee, M. J., Lee, S. N., Kim, T. H. & Oh, B. K. Noble Metal Nanomaterial-Based Biosensors for Electrochemical and Optical Detection of Viruses Causing Respiratory Illnesses. *Frontiers in Chemistry* vol. 9 (2021).

63. Lee, J. H., Cho, H. Y., Choi, H. K., Lee, J. Y. & Choi, J. W. Application of gold nanoparticle to plasmonic biosensors. *International Journal of Molecular Sciences* vol. 19 (2018).

64. Koushkestani, M., Abbasi-Moayed, S., Ghasemi, F., Mahdavi, V. & Hormozi-Nezhad, M. R. Simultaneous detection and identification of thiometon, phosalone, and prothioconazole pesticides using a nanoplasmonic sensor array. *Food and Chemical Toxicology* **151**, (2021).

65. Harke, S. S., Patil, R. v., Dar, M. A., Pandit, S. R. & Pawar, K. D. Functionalization of biogenic silver nanoparticles with Vitamin B12 for the detection of iron in food samples. *Food Chemistry Advances* **1**, 100017 (2022).

66. Rodal-Cedeira, S. *et al.* Plasmonic Au@Pd Nanorods with Boosted Refractive Index Susceptibility and SERS Efficiency: A Multifunctional Platform for Hydrogen Sensing and Monitoring of Catalytic Reactions. *Chemistry of Materials* **28**, 9169–9180 (2016).

67. Ni, B. & Wang, X. Face the Edges: Catalytic Active Sites of Nanomaterials. *Advanced Science* vol. 2 (2015).

68. Ma, X. *et al.* Noble Metal Nanoparticle-Based Multicolor Immunoassays: An Approach toward Visual Quantification of the Analytes with the Naked Eye. *ACS Sensors* vol. 4 782–791 (2019).

69. Gao, Z. *et al.* Facile Colorimetric Detection of Silver Ions with Picomolar Sensitivity. *Analytical Chemistry* **89**, 3622–3629 (2017).

70. Liu, Y. *et al.* "click" dendrimer-Pd nanoparticle assemblies as enzyme mimics: Catalytic: o -phenylenediamine oxidation and application in colorimetric H2O2detection. *Inorganic Chemistry Frontiers* **8**, 3301–3307 (2021).

71. Yu, R. J. *et al.* Real-time sensing of o-phenylenediamine oxidation on gold nanoparticles. *Sensors (Switzerland)* **17**, (2017).

72. Chen, J. *et al.* Glucose-oxidase like catalytic mechanism of noble metal nanozymes. *Nature Communications* **12**, (2021).

73. Cao, G. J., Jiang, X., Zhang, H., Croley, T. R. & Yin, J. J. Mimicking horseradish peroxidase and oxidase using ruthenium nanomaterials. *RSC Advances* **7**, 52210–52217 (2017).

74. Xia, X. *et al.* Pd-Ir Core-Shell Nanocubes: A Type of Highly Efficient and Versatile Peroxidase Mimic. *ACS Nano* **9**, 9994–10004 (2015).

75. Venkataraman, A., Amadi, E. V., Chen, Y. & Papadopoulos, C. Carbon Nanotube Assembly and Integration for Applications. *Nanoscale Research Letters* vol. 14 (2019).

76. Hofferber, E. M., Stapleton, J. A. & Iverson, N. M. Review—Single Walled Carbon Nanotubes as Optical Sensors for Biological Applications. *Journal of The Electrochemical Society* **167**, 037530 (2020).

77. Chen, Z. *et al.* Single-walled carbon nanotubes as optical materials for biosensing. *Nanoscale* vol. 3 1949–1956 (2011).

78. Galassi, T. v., Jena, P. v., Roxbury, D. & Heller, D. A. Single nanotube spectral imaging to determine molar concentrations of isolated carbon nanotube species. *Analytical Chemistry* **89**, 1073–1077 (2017).

79. Hendler-Neumark, A. & Bisker, G. Fluorescent single-walled carbon nanotubes for protein detection. *Sensors (Switzerland)* vol. 19 (2019).

80. Ackermann, J., Metternich, J. T., Herbertz, S. & Kruss, S. Biosensing with Fluorescent Carbon Nanotubes. *Angewandte Chemie - International Edition* vol. 61 (2022).

81. Ahmad, A., Kern, K. & Balasubramaman, K. Selective enhancement of carbon nanotube photoluminescence by resonant energy transfer. *ChemPhysChem* **10**, 905–909 (2009).

82. Landry, M. P. *et al.* Single-molecule detection of protein efflux from microorganisms using fluorescent single-walled carbon nanotube sensor arrays. *Nature Nanotechnology* **12**, 368–377 (2017).

83. Ferrier, D. C. & Honeychurch, K. C. Carbon nanotube (CNT)-based biosensors. *Biosensors* vol. 11 (2021).

84. Heller, D. A., Baik, S., Eurell, T. E. & Strano, M. S. Single-walled carbon nanotube spectroscopy in live cells: Towards long-term labels and optical sensors. *Advanced Materials* **17**, 2793–2799 (2005).

85. Tîlmaciu, C. M. & Morris, M. C. Carbon nanotube biosensors. *Frontiers in Chemistry* vol. 3 (2015).

86. Rizvi, S. B., Ghaderi, S., Keshtgar, M. & Seifalian, A. M. Semiconductor quantum dots as fluorescent probes for in vitro and in vivo bio-molecular and cellular imaging . *Nano Reviews* **1**, 5161 (2010).

87. Hong, S. & Lee, C. The current status and future outlook of quantum dot-based biosensors for plant virus detection. *Plant Pathology Journal* vol. 34 85–92 (2018).

88. Wegner, K. D. & Hildebrandt, N. Quantum dots: Bright and versatile in vitro and in vivo fluorescence imaging biosensors. *Chemical Society Reviews* vol. 44 4792–4834 (2015).

89. Ding, R. *et al.* Recent advances in quantum dots-based biosensors for antibiotic detection. *Journal of Pharmaceutical Analysis* (2021) doi:10.1016/j.jpha.2021.08.002.

90. Hu, M. *et al.* Shaping the Assembly of Superparamagnetic Nanoparticles. *ACS Nano* **13**, 3015–3022 (2019).

91. Holzinger, M., Goff, A. le & Cosnier, S. Nanomaterials for biosensing applications: A review. *Frontiers in Chemistry* vol. 2 (2014).

92. Cai, Y. *et al.* Magnet Patterned Superparamagnetic Fe3O4/Au Core–Shell Nanoplasmonic Sensing Array for Label-Free High Throughput Cytokine Immunoassay. *Advanced Healthcare Materials* **8**, (2019).

93. Xia, Y., Xiong, Y., Lim, B. & Skrabalak, S. E. Shape-controlled synthesis of metal nanocrystals: Simple chemistry meets complex physics? *Angewandte Chemie - International Edition* vol. 48 60–103 (2009).

94. Baig, N., Kammakakam, I., Falath, W. & Kammakakam, I. Nanomaterials: A review of synthesis methods, properties, recent progress, and challenges. *Materials Advances* vol. 2 1821–1871 (2021).

95. Malhotra, B. D. & Ali, Md. A. Nanomaterials in Biosensors. in *Nanomaterials for Biosensors* 1–74 (Elsevier, 2018). doi:10.1016/b978-0-323-44923-6.00001-7.

96. Mahajan, G., Kaur, M. & Gupta, R. Green functionalized nanomaterials: Fundamentals and future opportunities. in *Green Functionalized Nanomaterials for Environmental Applications* 21–41 (Elsevier, 2022). doi:10.1016/b978-0-12-823137-1.00003-8.

97. Lyu, Y., Martínez, Á., D'incà, F., Mancin, F. & Scrimin, P. The biotin–avidin interaction in biotinylated gold nanoparticles and the modulation of their aggregation. *Nanomaterials* **11**, (2021).

98. Jain, A. & Cheng, K. The principles and applications of avidin-based nanoparticles in drug delivery and diagnosis. *Journal of Controlled Release* vol. 245 27–40 (2017).

99. Otten, J. *et al.* A FRET-based biosensor for the quantification of glucose in culture supernatants of mL scale microbial cultivations. *Microbial Cell Factories* **18**, (2019).

100. Soler, M., Estevez, M. C., Cardenosa-Rubio, M., Astua, A. & Lechuga, L. M. How Nanophotonic Label-Free Biosensors Can Contribute to Rapid and Massive Diagnostics of Respiratory Virus Infections: COVID-19 Case. *ACS Sensors* **5**, 2663–2678 (2020).

101. Schasfoort, R. B. M. Chapter 1. Introduction to Surface Plasmon Resonance. in *Handbook of Surface Plasmon Resonance* 1–26 (Royal Society of Chemistry, 2017). doi:10.1039/9781788010283-00001.

102. Jatschka, J., Dathe, A., Csáki, A., Fritzsche, W. & Stranik, O. Propagating and localized surface plasmon resonance sensing - A critical comparison based on measurements and theory. *Sens Biosensing Res* **7**, 62–70 (2016).

103. Li, M., Cushing, S. K. & Wu, N. Plasmon-enhanced optical sensors: A review. *Analyst* vol. 140 386–406 (2015).

104. Hill, R. T. Plasmonic biosensors. *Wiley Interdisciplinary Reviews: Nanomedicine and Nanobiotechnology* vol. 7 152–168 (2015).

105. Hong, Y., Huh, Y. M., Yoon, D. S. & Yang, J. Nanobiosensors based on localized surface plasmon resonance for biomarker detection. *Journal of Nanomaterials* vol. 2012 (2012).

106. Jeanmaire, D. L. & van Duyne, R. P. Surface raman spectroelectrochemistry: Part I. Heterocyclic, aromatic, and aliphatic amines adsorbed on the anodized silver electrode. *Journal of Electroanalytical Chemistry and Interfacial Electrochemistry* **84**, 1–20 (1977).

107. Fleischmann, M., Hendra, P. J. & McQuillan, A. J. Raman spectra of pyridine adsorbed at a silver electrode. *Chemical Physics Letters* **26**, 163–166 (1974).

108. Zong, C. *et al.* Surface-Enhanced Raman Spectroscopy for Bioanalysis: Reliability and Challenges. *Chemical Reviews* vol. 118 4946–4980 (2018).

109. Bosch, M. E., Jesús Ruiz Sánchez, A., Rojas, F. S. & Ojeda, C. B. Recent Development in Optical Fiber Biosensors. *Sensors* **7**, 797–859 (2007).

110. Zhang, G. & Yang, P. A novel cell-cell communication mechanism in the nervous system: exosomes. *Journal of Neuroscience Research* vol. 96 45–52 (2018).

111. Maia, J., Caja, S., Strano Moraes, M. C., Couto, N. & Costa-Silva, B. Exosome-based cell-cell communication in the tumor microenvironment. *Frontiers in Cell and Developmental Biology* vol. 6 (2018).

112. van Niel G *et al.* Challenges and directions in studying cell–cell communication by extracellular vesicles. *Nature Reviews Molecular Cell Biology* 1–14 (2022).

113. McWhorter, F. Y. *et al.* Macrophage secretion heterogeneity in engineered microenvironments revealed using a microwell platform. *Integrative Biology (United Kingdom)* **8**, 751–760 (2016).

114. Chen, Z. *et al.* Multiplexed, Sequential Secretion Analysis of the Same Single Cells Reveals Distinct Effector Response Dynamics Dependent on the Initial Basal State. *Advanced Science* **6**, (2019).

115. Chokkalingam, V. *et al.* Probing cellular heterogeneity in cytokine-secreting immune cells using droplet-based microfluidics. *Lab on a Chip* **13**, 4740–4744 (2013).

116. Li, X. *et al.* Plasmonic nanohole array biosensor for label-free and real-time analysis of live cell secretion. *Lab on a Chip* **17**, 2208–2217 (2017).

117. Raphael, M. P., Christodoulides, J. A., Delehanty, J. B., Long, J. P. & Byers, J. M. Quantitative imaging of protein secretions from single cells in real time. *Biophysical Journal* **105**, 602–608 (2013).

118. Liu, G. *et al.* A Nanoparticle-Based Affinity Sensor that Identifies and Selects Highly Cytokine-Secreting Cells. *iScience* **20**, 137–147 (2019).

119. Cui, X. *et al.* A fluorescent microbead-based microfluidic immunoassay chip for immune cell cytokine secretion quantification. *Lab on a Chip* **18**, 522–531 (2018).

120. Joensson, H. N. & Andersson Svahn, H. Droplet microfluidics-A tool for single-cell analysis. *Angewandte Chemie - International Edition* vol. 51 12176–12192 (2012).

121. Yamagishi, M., Ohara, O. & Shirasaki, Y. Microfluidic Immunoassays for Time-Resolved Measurement of Protein Secretion from Single Cells. (2020) doi:10.1146/annurev-anchem-091619.

122. Bange, A., Halsall, H. B. & Heineman, W. R. Microfluidic immunosensor systems. *Biosensors and Bioelectronics* vol. 20 2488–2503 (2005).

123. Darwish, I. A. *Immunoassay Methods and their Applications in Pharmaceutical Analysis: Basic Methodology and Recent Advances*. *InternatIonal journal of BIomedIcal scIence* (2006).

124. Czerkinsky, C. C., Nilsson, L. Å., Nygren, H., Ouchterlony, Ö. & Tarkowski, A. A solid-phase enzyme-linked immunospot (ELISPOT) assay for enumeration of specific antibody-secreting cells. *Journal of Immunological Methods* **65**, 109–121 (1983).

125. Cox, J. H., Ferrari, G. & Janetzki, S. Measurement of cytokine release at the single cell level using the ELISPOT assay. *Methods* **38**, 274–282 (2006).

126. Boulet, S. *et al.* A dual color ELISPOT method for the simultaneous detection of IL-2 and IFN-γ HIV-specific immune responses. *Journal of Immunological Methods* **320**, 18–29 (2007).

127. Janetzki, S., Rueger, M. & Dillenbeck, T. Stepping up ELISpot: Multi-Level Analysis in FluoroSpot Assays. *Cells* **3**, 1102–1115 (2014).

128. Bucheli, O. T. M., Sigvaldadóttir, I. & Eyer, K. Measuring single-cell protein secretion in immunology: Technologies, advances, and applications. *European Journal of Immunology* vol. 51 1334–1347 (2021).

129. Wyatt Shields Iv, C., Reyes, C. D. & López, G. P. Microfluidic cell sorting: A review of the advances in the separation of cells from debulking to rare cell isolation. *Lab on a Chip* vol. 15 1230–1249 (2015).

130. Zhu, H. *et al.* Detecting cytokine release from single T-cells. *Analytical Chemistry* **81**, 8150–8156 (2009).

131. Ogunniyi, A. O., Story, C. M., Papa, E., Guillen, E. & Love, J. C. Screening individual hybridomas by microengraving to discover monoclonal antibodies. *Nature Protocols* **4**, 767–782 (2009).

132. Story, C. M. *et al.* Profiling antibody responses by multiparametric analysis of primary B cells. *Proceedings of the National Academy of Sciences* **105**, 17902–17907 (2008).

133. Bradshaw, E. M. *et al.* Concurrent detection of secreted products from human lymphocytes by microengraving: Cytokines and antigen-reactive antibodies. *Clinical Immunology* **129**, 10–18 (2008).

134. Yamanaka, Y. J. *et al.* Cellular barcodes for efficiently profiling single-cell secretory responses by microengraving. *Analytical Chemistry* **84**, 10531–10536 (2012).

135. Lu, Y. *et al.* Highly multiplexed profiling of single-cell effector functions reveals deep functional heterogeneity in response to pathogenic ligands. *Proc Natl Acad Sci U S A* **112**, E607–E615 (2015).

136. Torres, A. J., Hill, A. S. & Love, J. C. Nanowell-based immunoassays for measuring single-cell secretion: Characterization of transport and surface binding. *Analytical Chemistry* **86**, 11562–11569 (2014).

137. Mazutis L *et al.* Single-cell analysis and sorting using droplet-based microfluidics. *Nat Protoc* **8**, 870–891 (2013).

138. Matuła, K., Rivello, F. & Huck, W. T. S. Single-Cell Analysis Using Droplet Microfluidics. *Advanced Biosystems* vol. 4 (2020).

139. Conchouso, D. *et al.* Integration of Droplet Microfluidic Tools for Single-Cell Functional Metagenomics: An Engineering Head Start. *Genomics, Proteomics and Bioinformatics* **19**, 504–518 (2021).

140. Konry, T., Dominguez-Villar, M., Baecher-Allan, C., Hafler, D. A. & Yarmush, M. L. Droplet-based microfluidic platforms for single T cell secretion analysis of IL-10 cytokine. *Biosensors and Bioelectronics* **26**, 2707–2710 (2011).

141. Milgram, S. *et al.* On chip real time monitoring of B-cells hybridoma secretion of immunoglobulin. *Biosensors and Bioelectronics* **26**, 2728–2732 (2011).

142. Stojanović, I., van der Velden, T. J. G., Mulder, H. W., Schasfoort, R. B. M. & Terstappen, L. W. M. M. Quantification of antibody production of individual hybridoma cells by surface plasmon resonance imaging. *Analytical Biochemistry* **485**, 112–118 (2015).

143. Zhu, C. *et al.* Real-time monitoring and detection of single-cell level cytokine secretion using LSPR technology. *Micromachines (Basel)* **11**, (2020).

144. McDonald, M. P. *et al.* Visualizing Single-Cell Secretion Dynamics with Single-Protein Sensitivity. *Nano Letters* **18**, 513–519 (2018).

145. Corsetti, S. & Dholakia, K. Optical manipulation: advances for biophotonics in the 21st century. *Journal of Biomedical Optics* **26**, (2021).

146. Juan-Colás, J. *et al.* Quantifying single-cell secretion in real time using resonant hyperspectral imaging. *Proceedings of the National Academy of Sciences* **115**, 13204–13209 (2018).

147. Shirasaki, Y. *et al.* Real-time single-cell imaging of protein secretion. *Scientific Reports* **4**, (2014).

148. Qiu, L. *et al.* A membrane-anchored aptamer sensor for probing IFNγ secretion by single cells. *Chemical Communications* **53**, 8066–8069 (2017).

149. Guo, Z., Ren, J., Wang, J. & Wang, E. Single-walled carbon nanotubes based quenching of free FAM-aptamer for selective determination of ochratoxin A. *Talanta* **85**, 2517–2521 (2011).

150. Ogunniyi, A. O. *et al.* Profiling human antibody responses by integrated single-cell analysis. *Vaccine* **32**, 2866–2873 (2014).

151. Altan-Bonnet, G. & Mukherjee, R. Cytokine-mediated communication: a quantitative appraisal of immune complexity. *Nature Reviews Immunology* vol. 19 205–217 (2019).

152. Turner, M. D., Nedjai, B., Hurst, T. & Pennington, D. J. Cytokines and chemokines: At the crossroads of cell signalling and inflammatory disease. *Biochimica et Biophysica Acta - Molecular Cell Research* vol. 1843 2563–2582 (2014).

153. Liu, T., Wang, S., Wornow, M. & Altman, R. B. Construction of disease-specific cytokine profiles by associating disease genes with immune responses. *PLOS Computational Biology* **18**, e1009497 (2022).

154. Kany, S., Vollrath, J. T. & Relja, B. Cytokines in inflammatory disease. *International Journal of Molecular Sciences* vol. 20 (2019).

155. Tang, X. D. *et al.* Pathogenesis and treatment of cytokine storm induced by infectious diseases. *International Journal of Molecular Sciences* vol. 22 (2021).

156. Mauriz, E. & Lechuga, L. M. Plasmonic biosensors for single-molecule biomedical analysis. *Biosensors (Basel)* **11**, (2021).

157. Špačková, B., Wrobel, P., Bocková, M. & Homola, J. Optical Biosensors Based on Plasmonic Nanostructures: A Review. *Proceedings of the IEEE* vol. 104 2380–2408 (2016).

158. Liu, J., Jalali, M., Mahshid, S. & Wachsmann-Hogiu, S. Are plasmonic optical biosensors ready for use in point-of-need applications? *Analyst* vol. 145 364–384 (2020).

159. Chen, P. *et al.* Multiplex serum cytokine immunoassay using nanoplasmonic biosensor microarrays. *ACS Nano* **9**, 4173–4181 (2015).

160. Ke, P. C. *et al.* Implications of peptide assemblies in amyloid diseases. *Chemical Society Reviews* vol. 46 6492–6531 (2017).

161. Ballard, C. *et al.* Alzheimer's disease. *Lancet* **377**, 1019–1031 (2011).

162. Tublin, J. M., Adelstein, J. M., del Monte, F., Combs, C. K. & Wold, L. E. Getting to the Heart of Alzheimer Disease. *Circulation Research* vol. 124 142–149 (2019).

163. Mackic, J. B. *et al.* Circulating amyloid-b peptide crosses the blood-brain barrier in aged monkeys and contributes to Alzheimer's disease lesions. *Vascul Pharmacol* **38**, 303–313 (2002).

164. Matsubara, E. *et al.* Soluble Aβ homeostasis in AD and DS: Impairment of anti-amyloidogenic protection by lipoproteins. *Neurobiology of Aging* **25**, 833–841 (2004).

165. Biere, A. L. *et al.* Amyloid-Peptide Is Transported on Lipoproteins and Albumin in Human Plasma. *Journal of Biological Chemistry* **271**, 32916–32922 (1996).

166. Finn, T. E., Nunez, A. C., Sunde, M. & Easterbrook-Smith, S. B. Serum albumin prevents protein aggregation and amyloid formation and retains chaperone-like activity in the presence of physiological ligands. *Journal of Biological Chemistry* **287**, 21530–21540 (2012).

167. Algamal, M., Milojevic, J., Jafari, N., Zhang, W. & Melacini, G. Mapping the Interactions between the Alzheimer's Aβ-Peptide and human serum albumin beyond domain resolution. *Biophysical Journal* **105**, 1700–1709 (2013).

168. Kakinen, A., Javed, I., Faridi, A., Davis, T. P. & Ke, P. C. Serum albumin impedes the amyloid aggregation and hemolysis of human islet amyloid polypeptide and alpha synuclein. *Biochimica et Biophysica Acta - Biomembranes* **1860**, 1803–1809 (2018).

169. Ramanathan, A., Nelson, A. R., Sagare, A. P. & Zlokovic, B. v. Impaired vascular-mediated clearance of brain amyloid beta in Alzheimer's disease: The role, regulation and restoration of LRP1. *Frontiers in Aging Neuroscience* vol. 7 (2015).

170. Marsh, S. E. *et al.* The adaptive immune system restrains Alzheimer's disease pathogenesis by modulating microglial function. *Proc Natl Acad Sci U S A* **113**, E1316–E1325 (2016).

171. Rogers, J., Strohmeyer, R., Kovelowski, C. J. & Li, R. Microglia and inflammatory mechanisms in the clearance of amyloid β peptide. *GLIA* vol. 40 260–269 (2002).

172. Wang, Z.-T. *et al.* Association of lectin-like oxidized low density lipoprotein receptor 1 (OLR1) polymorphisms with late-onset Alzheimer disease in Han Chinese. *Annals of Translational Medicine* **6**, 172–172 (2018).

173. Marx, F., Blasko, I., Pavelka, M. & Grubeck-Loebenstein, B. The possible role of the immune system in Alzheimer's disease. *Exp Gerontol* **33**, 871–881 (1998).

174. Rogers, J. *et al.* Peripheral clearance of amyloid β peptide by complement C3-dependent adherence to erythrocytes. *Neurobiology of Aging* **27**, 1733–1739 (2006).

175. Bellomo, G. *et al.* Dissecting the Interactions between Human Serum Albumin and α-Synuclein: New Insights on the Factors Influencing α-Synuclein Aggregation in Biological Fluids. *Journal of Physical Chemistry B* **123**, 4380–4386 (2019).

176. Kuo, Y. M. *et al.* Amyloid-β peptides interact with plasma proteins and erythrocytes: Implications for their quantitation in plasma. *Biochemical and Biophysical Research Communications* **268**, 750–756 (2000).

177. Pilkington, E. H. *et al.* Profiling the Serum Protein Corona of Fibrillar Human Islet Amyloid Polypeptide. *ACS Nano* **12**, 6066–6078 (2018).

178. Sudhakar, S., Kalipillai, P., Santhosh, P. B. & Mani, E. Role of surface charge of inhibitors on amyloid beta fibrillation. *Journal of Physical Chemistry C* **121**, (2017).

179. Knowles, T. P. J., Vendruscolo, M. & Dobson, C. M. The amyloid state and its association with protein misfolding diseases. *Nature Reviews Molecular Cell Biology* vol. 15 384–396 (2014).

180. Shozawa, H. *et al.* Supratherapeutic concentrations of cilostazol inhibits β-amyloid oligomerization in vitro. *Neuroscience Letters* **677**, 19–25 (2018).

181. Wiltzius, J. J. W., Sievers, S. A., Sawaya, M. R. & Eisenberg, D. Atomic structures of IAPP (amylin) fusions suggest a mechanism for fibrillation and the role of insulin in the process. *Protein Science* **18**, 1521–1530 (2009).

182. Zhang, X., St Clair, J. R., London, E. & Raleigh, D. P. Islet amyloid polypeptide membrane interactions: Effects of membrane composition. *Biochemistry* **56**, 376–390 (2017).

183. Pilkington, E. H. *et al.* Star Polymers Reduce Islet Amyloid Polypeptide Toxicity via Accelerated Amyloid Aggregation. *Biomacromolecules* **18**, 4249–4260 (2017).

184. Faridi, A. *et al.* Mitigating Human IAPP Amyloidogenesis In Vivo with Chiral Silica Nanoribbons. *Small* **14**, (2018).

185. Cao, W. & Zheng, H. Peripheral immune system in aging and Alzheimer's disease 11 Medical and Health Sciences 1109 Neurosciences. *Molecular Neurodegeneration* vol. 13 (2018).

186. Zheng, C., Zhou, X. W. & Wang, J. Z. The dual roles of cytokines in Alzheimer's disease: Update on interleukins, TNF-α, TGF-β and IFN-γ. *Translational Neurodegeneration* vol. 5 (2016).

187. Lexa, K. W., Dolghih, E. & Jacobson, M. P. A structure-based model for predicting serum albumin binding. *PLoS ONE* **9**, (2014).

188. Javed, I. *et al.* Probing the Aggregation and Immune Response of Human Islet Amyloid Polypeptides with Ligand-Stabilized Gold Nanoparticles. *ACS Applied Materials and Interfaces* **11**, 10462–10471 (2019).

189. Benilova, I., Karran, E. & de Strooper, B. The toxic Aβ oligomer and Alzheimer's disease: An emperor in need of clothes. *Nature Neuroscience* vol. 15 349–357 (2012).

190. Campioni S *et al.* A causative link between the structure of aberrant protein oligomers and their toxicity. *Nat Chem Biol* **6**, 140–147 (2010).

191. Milojevic, J., Esposito, V., Das, R. & Melacini, G. Understanding the Molecular Basis for the Inhibition of the Alzheimer's A-Peptide Oligomerization by Human

Serum Albumin Using Saturation Transfer Difference and Off-Resonance Relaxation NMR Spectroscopy. *J Am Chem Soc* **129**, 4282–4290 (2007).

192. Deng ZJ, Liang M, Monteiro M, Toth I & Minchin RF. Nanoparticle-induced unfolding of fibrinogen promotes Mac-1 receptor activation and inflammation. *Nat Nanotechnol* **6**, 39–44 (2011).
193. Hardy, J. & Selkoe, D. J. The Amyloid Hypothesis of Alzheimer's Disease: Progress and Problems on the Road to Therapeutics. *Science (1979)* **297**, 353–356 (2002).
194. Kayed R *et al.* Common Structure of Soluble Amyloid Oligomers Implies Common Mechanism of Pathogenesis. *Science (1979)* **300**, 486–489 (2003).
195. Mannini, B. *et al.* Toxicity of protein oligomers is rationalized by a function combining size and surface hydrophobicity. *ACS Chemical Biology* **9**, 2309–2317 (2014).
196. Krotee, P. *et al.* Atomic structures of fibrillar segments of hIAPP suggest tightly mated b-sheets are important for cytotoxicity. *Elife* **6**, e19273 (2017).
197. Faridi, A. *et al.* Differential Roles of Plasma Protein Corona on Immune Cell Association and Cytokine Secretion of Oligomeric and Fibrillar Beta-Amyloid. *Biomacromolecules* **20**, 4208–4217 (2019).
198. June, C. H. *et al.* Engineered T cells for cancer therapy. *Cancer Immunology, Immunotherapy* vol. 63 969–975 (2014).
199. Grupp, S. A. *et al.* Chimeric Antigen Receptor–Modified T Cells for Acute Lymphoid Leukemia. *New England Journal of Medicine* **368**, 1509–1518 (2013).
200. Lee, D. W. *et al.* T cells expressing CD19 chimeric antigen receptors for acute lymphoblastic leukaemia in children and young adults: A phase 1 dose-escalation trial. *The Lancet* **385**, 517–528 (2015).
201. Davila, M. L. *et al.* Efficacy and Toxicity Management of 19-28z CAR T Cell Therapy in B Cell Acute Lymphoblastic Leukemia. *Sci Transl Med* **6**, 224ra25 (2014).

202. Porter, D. L. *et al.* Chimeric antigen receptor T cells persist and induce sustained remissions in relapsed refractory chronic lymphocytic leukemia. *Sci Transl Med* **7**, 303ra139 (2015).

203. Fraietta, J. A. *et al.* Determinants of response and resistance to CD19 chimeric antigen receptor (CAR) T cell therapy of chronic lymphocytic leukemia. *Nature Medicine* **24**, 563–571 (2018).

204. Brudno, J. N. & Kochenderfer, J. N. Toxicities of chimeric antigen receptor T cells: Recognition and management. *Blood* vol. 127 3321–3330 (2016).

205. Brownlie, R. J. & Zamoyska, R. T cell receptor signalling networks: Branched, diversified and bounded. *Nature Reviews Immunology* vol. 13 257–269 (2013).

206. Cox, J. H., Ferrari, G. & Janetzki, S. Measurement of cytokine release at the single cell level using the ELISPOT assay. *Methods* **38**, 274–282 (2006).

207. Han, Q. *et al.* Polyfunctional responses by human T cells result from sequential release of cytokines. *Proc Natl Acad Sci U S A* **109**, 1607–1612 (2012).

208. Chattopadhyay, P. K. & Roederer, M. Good cell, bad cell: Flow cytometry reveals T-cell subsets important in HIV disease. *Cytometry Part A* vol. 77 614–622 (2010).

209. Tay, S. *et al.* Single-cell NF-B dynamics reveal digital activation and analogue information processing. *Nature* **466**, 267–271 (2010).

210. Agasti, S. S., Liong, M., Peterson, V. M., Lee, H. & Weissleder, R. Photocleavable DNA barcode-antibody conjugates allow sensitive and multiplexed protein analysis in single cells. *J Am Chem Soc* **134**, 18499–18502 (2012).

211. Elsawa, S. F. *et al.* Comprehensive analysis of tumor microenvironment cytokines in Waldenstrom macroglobulinemia identifies CCL5 as a novel modulator of IL-6 activity. *The Journal of the American Society of Hematology* **118**, 5540–5549 (2011).

212. Stewart, M. E. *et al.* Nanostructured plasmonic sensors. *Chemical Reviews* vol. 108 494–521 (2008).

213. Kumar S, Rosenberg JM, Bouzida D, Swendsen RH & Kollman PA. The Weighted Histogram Analysis Method for Free-Energy Calculations on Biomolecules. I. The Method. *J Comput Chem* **13**, 1011–1021 (1992).

214. Francis, K. & Palsson, B. O. Effective intercellular communication distances are determined by the relative time constants for cytochemokine secretion and diffusion (cell signalingbioreactor designtissue engineering). *Proceedings of the National Academy of Sciences* **94**, 12258–12262 (1997).

215. Visser, E. W. A., Horáček, M. & Zijlstra, P. Plasmon Rulers as a Probe for Real-Time Microsecond Conformational Dynamics of Single Molecules. *Nano Letters* **18**, 7927–7934 (2018).

216. Mandal M & Breaker RR. Gene regulation by riboswitches. *Nature reviews Molecular cell biology* **5**, 451–463 (2004).

217. Gelinas, A. D. *et al.* Crystal structure of interleukin-6 in complex with a modified nucleic acid ligand. *Journal of Biological Chemistry* **289**, 8720–8734 (2014).

218. Zuker, M. Mfold web server for nucleic acid folding and hybridization prediction. *Nucleic Acids Research* **31**, 3406–3415 (2003).

219. Zhang, A. Y. Q., Bugaut, A. & Balasubramanian, S. A sequence-independent analysis of the loop length dependence of intramolecular RNA G-quadruplex stability and topology. *Biochemistry* **50**, 7251–7258 (2011).

220. Ding, F. *et al.* Ab initio RNA folding by discrete molecular dynamics: From structure prediction to folding mechanisms. *RNA* **14**, 1164–1173 (2008).

221. Hirano, T. IL-6 in inflammation, autoimmunity and cancer. *International immunology* vol. 33 127–148 (2021).

222. Zhou, Y. *et al.* Evaluation of Single-Cell Cytokine Secretion and Cell-Cell Interactions with a Hierarchical Loading Microwell Chip. *Cell Reports* **31**, (2020).

223. Santarlasci, V., Cosmi, L., Maggi, L., Liotta, F. & Annunziato, F. IL-1 and T helper immune responses. *Frontiers in Immunology* **4**, 182 (2013).

224. Khalaf, H., Jass, J. & Olsson, P. E. Differential cytokine regulation by NF-κB and AP-1 in Jurkat T-cells. *BMC Immunology* **11**, (2010).

225. Liu, T., Wang, S., Wornow, M. & Altman, R. B. Construction of disease-specific cytokine profiles by associating disease genes with immune responses. *PLOS Computational Biology* **18**, e1009497 (2022).

226. Malucelli, E. *et al.* Single cell versus large population analysis: cell variability in elemental intracellular concentration and distribution. *Analytical and Bioanalytical Chemistry* **410**, 337–348 (2018).

227. Bucheli, O. T. M., Sigvaldadóttir, I. & Eyer, K. Measuring single-cell protein secretion in immunology: Technologies, advances, and applications. *European Journal of Immunology* vol. 51 1334–1347 (2021).

228. Oh, B. R. *et al.* Multiplexed Nanoplasmonic Temporal Profiling of T-Cell Response under Immunomodulatory Agent Exposure. *ACS Sensors* **1**, 941–948 (2016).

229. Jiao, M., Li, W., Yu, Y. & Yu, Y. Anisotropic presentation of ligands on cargos modulates degradative function of phagosomes. *Biophysical Reports* **2**, 100041 (2022).

230. Sterner, R. C. & Sterner, R. M. CAR-T cell therapy: current limitations and potential strategies. *Blood Cancer Journal* vol. 11 (2021).

231. Greenbaum, U., Mahadeo, K. M., Kebriaei, P., Shpall, E. J. & Saini, N. Y. Chimeric Antigen Receptor T-Cells in B-Acute Lymphoblastic Leukemia: State of the Art and Future Directions. *Frontiers in Oncology* vol. 10 (2020).

232. Shimabukuro-Vornhagen, A. *et al.* Cytokine release syndrome. *Journal for ImmunoTherapy of Cancer* vol. 6 (2018).

233. Li, X., Shao, M., Zeng, X., Qian, P. & Huang, H. Signaling pathways in the regulation of cytokine release syndrome in human diseases and intervention therapy. *Signal Transduction and Targeted Therapy* vol. 6 (2021).

234. Hao, Z., Li, R., Meng, L., Han, Z. & Hong, Z. Macrophage, the potential key mediator in CAR-T related CRS. *Experimental Hematology and Oncology* vol. 9 (2020).

235. Giavridis, T. *et al.* CAR T cell-induced cytokine release syndrome is mediated by macrophages and abated by IL-1 blockade letter. *Nature Medicine* **24**, 731–738 (2018).

236. Norelli, M. *et al.* Monocyte-derived IL-1 and IL-6 are differentially required for cytokine-release syndrome and neurotoxicity due to CAR T cells. *Nature Medicine* **24**, 739–748 (2018).

237. Brinkmann, V., Geiger, T., Alkan, S. & Heusser, C. H. Interferon alpha increases the frequency of interferon gamma-producing human CD4+ T cells. *Journal of experimental medicine* **178**, 1655–1663 (1993).

238. Han, Q., Bradshaw, E. M., Nilsson, B., Hafler, D. A. & Love, J. C. Multidimensional analysis of the frequencies and rates of cytokine secretion from single cells by quantitative microengraving. *Lab on a Chip* **10**, 1391–1400 (2010).

239. Carter, L. J. *et al.* Assay Techniques and Test Development for COVID-19 Diagnosis. *ACS Central Science* **6**, 591–605 (2020).

240. Qiu, G. *et al.* Dual-Functional Plasmonic Photothermal Biosensors for Highly Accurate Severe Acute Respiratory Syndrome Coronavirus 2 Detection. *ACS Nano* **14**, 5268–5277 (2020).

241. Yu L *et al.* Rapid Detection of COVID-19 Coronavirus Using a Reverse Transcriptional Loop-Mediated Isothermal Amplification (RT-LAMP) Diagnostic Platform. *Clin Chem* **6**, 224ra25 (2014).

242. Thiviyanathan, V. & Gorenstein, D. G. Aptamers and the next generation of diagnostic reagents. *Proteomics - Clinical Applications* vol. 6 563–573 (2012).

243. Song, Y. *et al.* Discovery of Aptamers Targeting the Receptor-Binding Domain of the SARS-CoV-2 Spike Glycoprotein. *Analytical Chemistry* **92**, 9895–9900 (2020).